ABSTRACT

Title of Document: DEVELOPMENT OF A BIO-INSPIRED MAGNETOSTRICTIVE FLOW AND TACTILE SENSOR

Michael Adam Marana, M.S., 2012

Directed By: Professor, Alison Flatau, Aerospace Engineering

A magnetostrictive sensor was designed, constructed, and evaluated for use as flow or tactile sensor. Vibrissa-like beams (whiskers) were cut from sheets of the magnetostrictive iron-gallium alloy, Galfenol. These beams were cantilevered, with the fixed end of the whisker attached to a permanent magnet to provide the whisker with a magnetic bias. The free portion of the whisker was quasi-statically loaded, causing the whisker-like sensor to bend. The bending-induced strain caused the magnetization of the whisker to change, resulting in a changing magnetic field in the area surrounding the whisker. The change in magnetic field was detected by a giant magnetoresistance (GMR) sensor placed in proximity to the whisker. Therefore, the electrical resistance change of the GMR sensor was a function of the bending in the whisker due to external forces. Prototype design was aided using a bidirectionally coupled magnetoelastic model for computer simulation. The prototype was tested and evaluated under tactile loading and low speed flow conditions.

DEVELOPMENT OF A BIO-INSPIRED MAGNETOSTRICTIVE FLOW AND TACTILE SENSOR

By

Michael Adam Marana

Thesis submitted to the Faculty of the Graduate School of the
University of Maryland, College Park, in partial fulfillment
of the requirements for the degree of
Master of Science
2012

Advisory Committee:
Professor Alison Flatau, Chair
Professor Sung Lee
Professor Norman Wereley

Acknowledgements

First and foremost, I would like to thank my advisor Dr. Alison Flatau for accepting me as a student, providing me with a research assistantship, and helping me to complete the research presented in this thesis. She has offered endless amounts of encouragement to me throughout the last two-and-a-half years, and her knowledge and wisdom have been an inspiration. I am forever grateful for her patience, understanding, and guidance.

I would also like to thank the members of Dr. Flatau's magnetostrictive research group. Dr. Jin Yoo was an invaluable resource for me, as he helped me understand the various aspects of magnetostrictive materials. Dr. Souk Min Na prepared Galfenol specimens that I tested and am presenting in this thesis. Ganesh Raghunath helped me conduct magnetomechanical characterizations on the Galfenol specimens in this thesis. I would also like to acknowledge the rest of the magnetostrictive group – Dr. Chaitanya Mudivarthi, Dr. Jung Jin Park, and Darryl Douglas – for their help throughout my thesis research.

My family and friends have been a constant source of encouragement for me in completing this thesis. I am truly inspired by my parents' and brothers' hard work and dedication to their careers; they are the reason I pursued higher education, and the reason I could push myself to finish.

I would also like to acknowledge the Multidisciplinary University Research Initiative grant that funded this project – ONR-MURI # N000140610530.

Table of Contents

List of Figures

Chapter 1: Introduction

Sensors are devices that enable the observation or measurement of physical phenomena. In modern engineering, sensors are integrated into the design and construction of many types of vehicles to allow the observation of changes in the vehicle's environment. The system controlling the vehicle can then assess and adapt to those changes if necessary.

An example of a sensor is the common use of pitot tubes in current aeronautical and naval systems used to determine speed of the vehicle as it travels through air or water. Used in combination with the static air pressure sensors, pitot-static systems found on many airplanes are utilized for air speed indicators, altimeters, and vertical speed indicators (U.S. Department of Transportation Federal Aviation Administration, 2008). Traditional sensors such as pitot tubes may not always be ideal for all situations. Some unconventional environments may call for alternative types of sensors. This thesis focuses on the development of a new type of sensor that may be used to detect fluid flow or solid objects in proximity to a vehicle or platform.

Motivation for Alternative Sensors

Autonomous Vehicles

The aerospace industry has seen a rapid rise in the research and development of uninhabited air vehicles (UAVs) (Hockmuth, 2007). UAVs can be used in military situations where manned reconnaissance aircraft cannot fly over a certain area due to risks of pilot casualties from enemy air defenses. UAVs are also not subject to human

endurance limitations. Without the need for an on-board pilot life support systems do not need to be built into the aircraft, resulting in a smaller platform, or larger payload capacity. (Haulman, 2003)

Micro air vehicles (MAVs) make up a class of UAVs that have lengths of 6 inches or less, and weights of 200 grams or less. These compact autonomous vehicles have the ability to navigate through confined spaces where larger UAVs cannot fly.

MAV researchers have noticed the efficiency and performance of flying biological organisms. In an attempt to increase the efficiency and performance of MAVs, researchers are creating designs that mimic biological flight. In particular, many MAV designs are created to mimic the flapping wing behavior of birds and insects.

MAVs operate in a sensitive Reynolds number regime where complex aerodynamic phenomena take place (Pines & Bohorquez, 2006). The system controlling an MAV requires data about the flow field around the vehicle. Data about fluid flow around MAVs may not be able to be captured with traditional pitot-static systems due to the low payload capacities of MAVs. Nontraditional sensors that are small, efficient, and lightweight are required to capture precise data about the fluid surrounding platforms such as micro air vehicles. Similar to how bio-inspired flapping-wing MAVs are being researched, engineers are studying how organisms sense their environments and are implementing those sensing mechanisms into nontraditional sensor designs.

Sensors in Nature

Many aquatic animals have sensors that supplement or substitute vision to allow them to navigate through dark or murky waters. It was found that harbor seals use their whiskers to detect disturbances in the water, allowing the seals to hunt fish in dark conditions. The whiskers of a harbor seal were found to be so sensitive that blindfolded seals were able to follow the hydrodynamic trails of a miniature submarine (Dehnhardt, Mauck, Hanke, & Bleckmann, 2001).

Fish have a series of sensors (neuromasts) running along their bodies that enables them to detect the flow of water in their surroundings. Neuromasts contain a series of hair cells (cilia) in a gelatinous cupula. As fluid flow interacts with the cupula, the cilia are deflected, stimulating the sensory nerve attached to the neuromasts. Some types of neuromasts are sensitive to flow velocity, while others are sensitive to flow acceleration. The sensitive flow sensors found on fish allow them to catch prey and evade predators (Barbier & Humphrey, 2008).

Arthropods have tactile hairs over much of their bodies. The tactile hair is exposed to external stimuli. The energy from a stimulus is transmitted along the hair to a dendrite ending, allowing the arthropod to react to the stimulus. The tactile-sensing ability of certain night-active arthropods allows them to navigate their surroundings in complete darkness (Albert, Friedrich, Dechant, & Barth, 2001).

Biological sensing elements such as the whiskers on a harbor seal or the haircells on fish lateral lines or spider legs interact with flow in a similar way. The filament part of the sensor extends into the flow field around the organism and is bent due to the drag imparted by the flow. In the case of tactile sensing, solid objects

interact with the filament causing it to bend. Nerves transduce the mechanical displacement of the filament into electrical signals that are sent through the nervous system to allow the organism to process information about its environment.

In order to match the effectiveness of biological sensors, a technological flow and tactile sensor that mimics the sensing mechanism of whiskers and haircells is investigated.

Smart Materials

Smart materials generally have properties that can change in response to an external stimulus. Smart materials enable lifelike sensing and actuating capabilities in structures. Research in smart materials has resulted in bio-inspired sensors and actuators that are unique in their durability, size, and accuracy. These smart sensors and actuators allow for more sophisticated engineering designs that result in smart structures and smart systems. Smart sensors embedded into a structure allow for advanced capabilities in stress, strain, and health monitoring. Actuators made of smart materials provide precision actuation and can enable structures to have morphing or adaptive geometry.

Common smart materials are listed below:

Smart Materials	Ability
Piezoelectrics (piezoceramics such as lead zirconate titanate (PZT))	Direct Piezoelectric Effect: Generates voltage in response to mechanical forces Converse Piezoelectric Effect: Induced mechanical strain in response to electric field
Shape-Memory Materials (e.g. Nitinol)	When mechanically deformed, returns to original shape upon heating
Magnetostrictive Materials (e.g. Terfenol-D, Galfenol)	Strain in response to an external magnetic field, or change in magnetization in response to mechanical

	forces
Electro- and Magnetorheological Fluids	Changing viscosity due to external electrical or magnetic fields
Electroactive Polymers	Change shape upon application of electric field

(Tzou, Lee, & Arnold, 2004), (Flatau & Chong, 2002)

(Spillman Jr, Sirkis, & Gardiner, 1996) define a smart structure as a non-biological physical structure that has a definite purpose, a means and imperative to achieve that purpose, and a biological pattern of functioning. It was determined that a bio-inspired sensor made of smart materials may fulfill the need for an alternative sensor that is efficient, reliable, and multifunctional.

Multifunctional Structures

Smart materials can provide the unique capability of serving as multifunction structures in engineering systems. Multifunctional structure integration into MAVs is an emerging technology (Pines & Bohorquez, 2006). By integrating structures that serve more than one purpose, the system can be lighter and more efficient. A structure that can sense different stimuli and support loads would eliminate the weight and power requirements of multiple sensors that serve different purposes.

Magnetostriction

Magnetostrictive materials demonstrate magnetostriction – a change in dimensions – upon application of a magnetic field, or change magnetization upon application of a mechanical force (Lee, 1955). Terfenol-D – an alloy of terbium, dysprosium, and iron – demonstrates very large magnetostrictive strains up to 3600 parts per million(3600×10^{-6}). Galfenol is an iron-based alloy containing gallium that

can achieve magnetostrictive strains that are on the order of 400 parts per million (400×10^{-6}).

Essentials of Magnetostriction

Magnetostrictive materials are made up of magnetic domains – regions of uniform magnetization. When the material is in an unmagnetized state, the domains are distributed in different directions to minimize the internal energy. As a magnetic field is applied to the material, the minimum internal energy happens when the domain moments are aligned with the direction of the field. Overall, this results in the material changing in length (Δl) in the direction of the magnetic field. This phenomenon, the Joule effect, is the mechanism by which magnetostrictive actuators function.

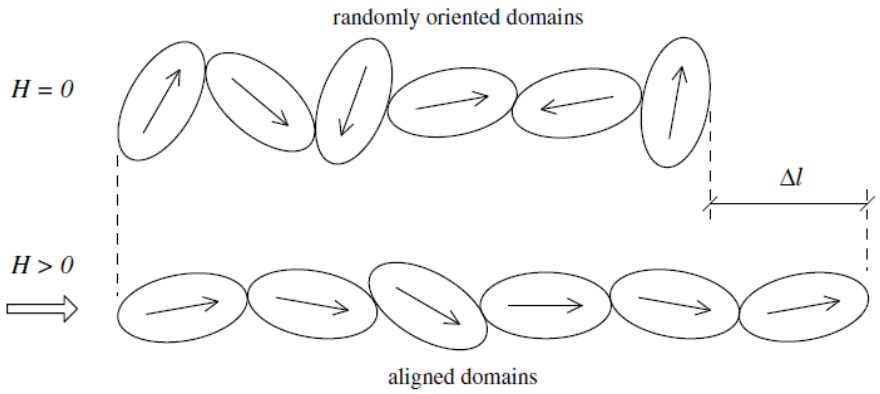

Figure 1: Schematic of Domain Alignment in Magnetostrictive Materials upon Application of a Magnetic Field (Chopra, 2009)

If the magnetic field is applied in the opposite direction, an equal length change would occur as the domains would rotate to align themselves with the direction of the field, as seen in Figure 2.

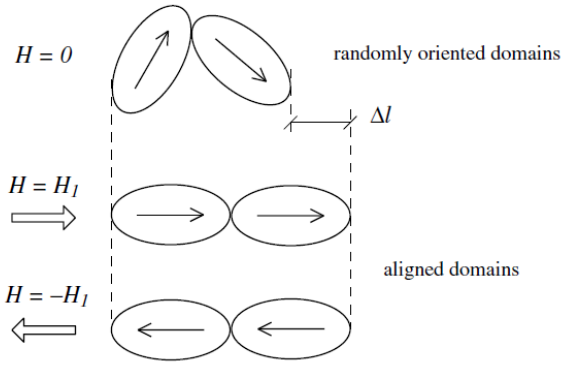

Figure 2: Schematic of Domain Rotation in Magnetostrictive Materials upon Application of Magnetic Fields in Opposite Directions (Chopra, 2009)

Saturation occurs when the magnetic domains are completely oriented in the direction of the field, preventing any further change in length in that direction. Figure 3 shows the variations in magnetostriction with an applied magnetic field for <100> oriented single crystal furnace cooled $Fe_{81}Ga_{19}$, with compressive pre-stress values of 0, 15, 30, 45, 60, and 80 MPa. One can observe saturation when the external magnetic field becomes sufficiently strong to overcome the applied compressive pre-stress and fully rotate all of the magnetic moments into alignment.

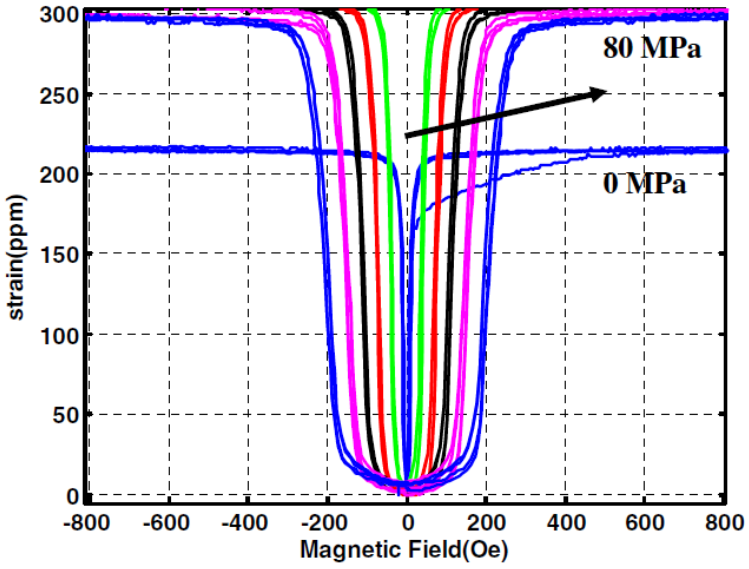

Figure 3: Strain-H Curve for furnace cooled, <100> oriented, single crystal $Fe_{81}Ga_{19}$ rods of 1 inch length and .25 inch diameter under axial compressive pre-stresses of 0, 15, 30, 45, 60, and 80 MPa (Atulasimha, 2006)

The inverse of the Joule effect is the Villari effect. If magnetic domains of the material are already aligned with the direction of the magnetic field, then a compressive force – along the same axis of the field – will cause the domains to rotate to a direction perpendicular to the field. The Villari effect allows for magnetostrictive-based sensors that can measure force and displacement.

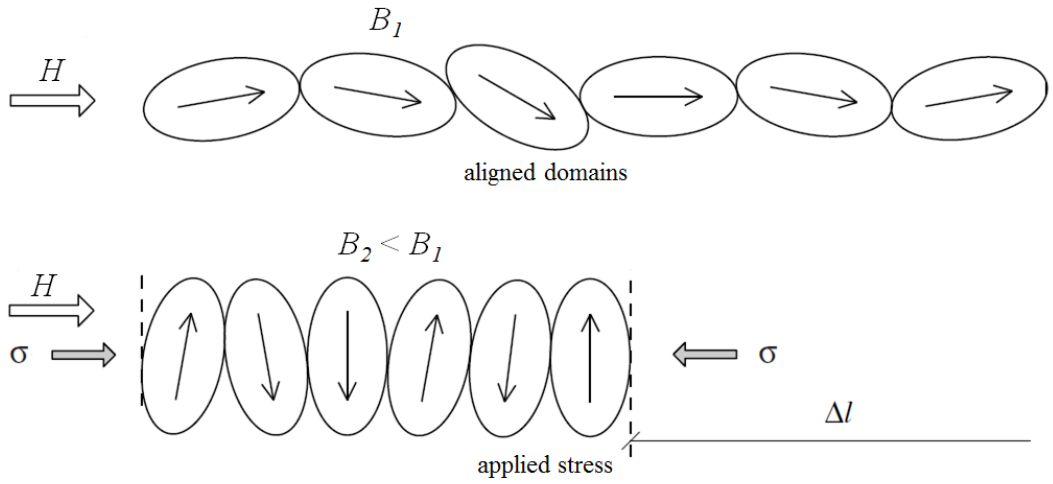

Figure 4: Domain Rotation and Magnetic Induction Change with Stress Application

Figure 5 shows the variations in magnetic induction with applied axial stress for <100> oriented 19 at. % Ga of furnace cooled, single crystal FeGa, with axially-applied magnetic fields of 0, 22.3, 44.6, 66.9, 89.1, 111, 167, 223, 446, and 891 Oe. One can observe saturation, with all moments aligned perpendicular to the applied stress, when the external stress becomes sufficiently strong to overcome the applied magnetic biasing field and fully rotate all magnetic moments.

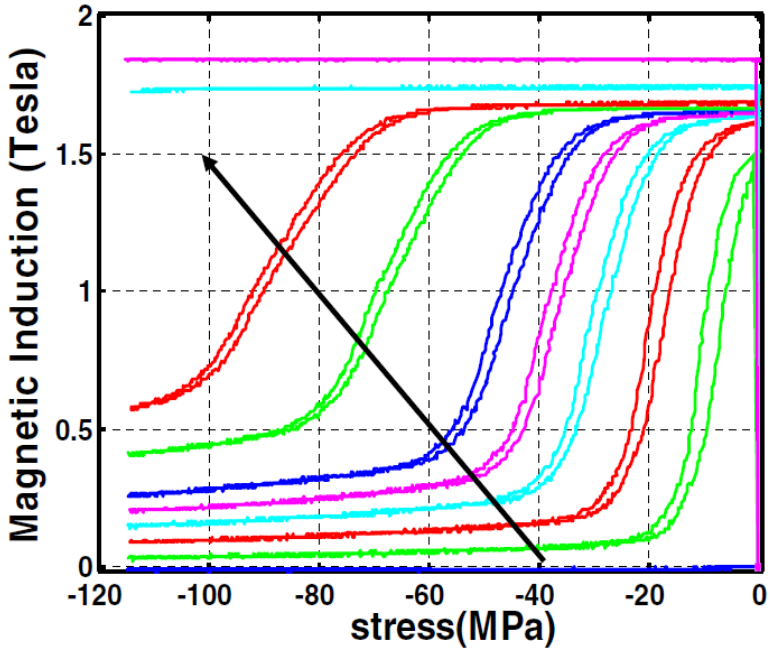

Figure 5: B-Stress Characteristics for furnace cooled, <100> oriented, single crystal $Fe_{81}Ga_{19}$ rods of 1 inch length and .25 inch diameter. Constant magnetic fields of H= 0, 22.3, 44.6, 66.9, 89.1, 111, 167, 223, 446, 891 Oe. (Atulasimha, 2006)

Magnetostrictive Models

Various constitutive models exist to describe magnetomechanical behavior of magnetostrictive materials. A set of linear constitutive equations exist to describe small perturbations of stress (σ), strain (ϵ), magnetic field (H), and magnetic induction (B):

$$\varepsilon = S^H \sigma + d_{33} H$$

$$B = d_{33}^{*}\sigma + \mu^{\sigma}H$$

$$S^{H} = {}^{1}/_{E^{H}}$$

$$d_{33}^{*} = \frac{\Delta B}{\Delta \sigma}\Big|_{H=cont}$$

Non-linear equations exist for more accurate modeling of large perturbations of stress, strain, magnetic field, and magnetic induction. Models such as the Jiles Model capture the physics of domain rotations and domain walls, but do not consider the material's dependence on the direction of magnetization, known as magnetocrystalline anisotropy. (Jiles & Atherton, 1984)

Energy-based models such as the approach presented by Armstrong, consider Zeeman, stress-induced anisotropy, and magnetocrystalline energies. Magnetic domains are likely to be oriented along directions that correspond to minimal local free energy. (Armstrong, 1997)

Galfenol vs. Terfenol-D

Galfenol is more ductile and has a tensile strength up to 20 times that of Terfenol-D. In addition to more suitable mechanical properties in certain applications, the raw material for some Galfenol compositions can be cheaper. $Fe_{81}Ga_{19}$ can cost as low as \$0.08/g. In comparison, the raw material cost of Terfenol-D ($Tb_{27}Dy_{73}Fe_{195}$) is approximately \$0.50/g using crystal growth processes (Kellogg, 2003).

Bending Behavior in Galfenol

The improved mechanical properties of Galfenol allow for bending of the material. Based on Euler-Bernoulli beam theory, the stress distribution $\sigma(x, z)$ of a cantilevered beam of length L is:

$$\sigma(x,z) = \frac{F}{I(x)}(x-L)z,$$

where F is the tip load, I is the area moment of inertia, x is a position along the length of the beam, and z is a position along the thickness of the beam. For an isotropic material, this results in an antisymmetric axial stress distribution in the beam about the neutral axis during bending, as shown in Figure 6.

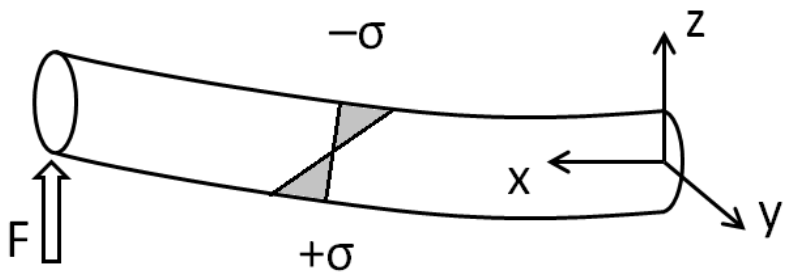

Figure 6: Beam Bending for Isotropic Materials with Antisymmetric Axial Loads about the Neutral Axis

A Galfenol bending sensor can be created by applying a biasing field along the length of a Galfenol beam, in order to align the magnetic domains along the beam length. As the beam is bent, the antisymmetric axial stress distribution shows axial compression on one surface of the beam, and an opposing axial tension on the other surface of the beam. The axial compression of the beam causes rotation of the magnetic domains, while axial tension of the beam has little effect on the domains. The result is a net magnetization in the beam. A schematic of a magnetostrictive bending sensor is shown in Figure 7.

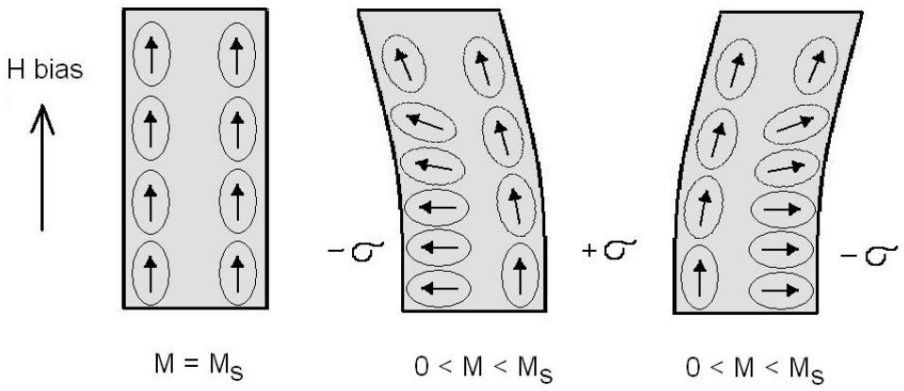

Figure 7: Schematic Showing Domain Rotation of a Magnetically Biased Galfenol Sample with Bending (Downey P. R., 2008)

Galfenol bending experiments were done by (Downey & Flatau, 2005) to demonstrate the material's use as a bending sensor. Single-crystal and poly-crystal Galfenol samples were used in the experiments, varying from 16% Galfenol to 21% Galfenol. In Figure 8, a single-crystal $Fe_{84}Ga_{16}$ cylindrical beam was biased with a 67 Oe field, and subjected to a sinusoidal-like tip force.

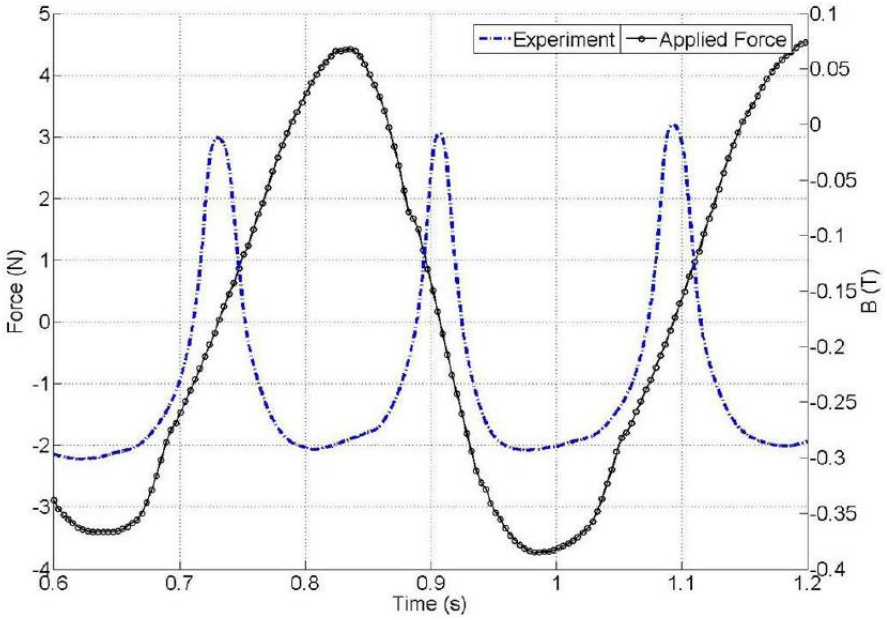

Figure 8: Experimental 0.3 T variation in magnetic induction measured with a pickup coil of the single crystal $Fe_{84}Ga_{16}$ beam with a 67 Oe bias field subjected to manual sinusoidal-like force input of 4N (Downey P. R., 2008)

The magnetic induction was measured with a pickup coil that was placed around the beam, and with a GMR sensor at the clamped end of the cantilevered beam. The result from the coil, shown in Figure 8, indicates that the magnetic induction B decreases regardless of whether the applied tip force is positive or negative. (Downey P. R., 2008)

The reorientation of Galfenol magnetic domains under bending was also optically verified. A Galfenol ($Fe_{81}Ga_{19}$ + 1.0% NbC) polycrystalline annealed sample of 7 cm length with a width and thickness of .6 mm was created with a <100> orientation along the length of the whisker. The Galfenol specimen was observed under a magneto-optic Kerr effect (MOKE) microscope. The specimen was magnetically biased along the length of the whisker. The MOKE microscope was used to observe changes in the orientation of the specimen's magnetic domains as the specimen was bent. Figure 9 shows the observed domain rotation during bending of the specimen. In Figure 9b, domains can be seen to be aligned nearly parallel to the specimen as it is magnetically biased along the length of the specimen. In Figure 9a and Figure 9b, the domains rotate out of alignment on the compression side of the specimen. The details of Galfenol bending under a MOKE microscope are further explained in Appendix A – Visualizing Magnetic Domains During Bending Using MOKE Microscope.

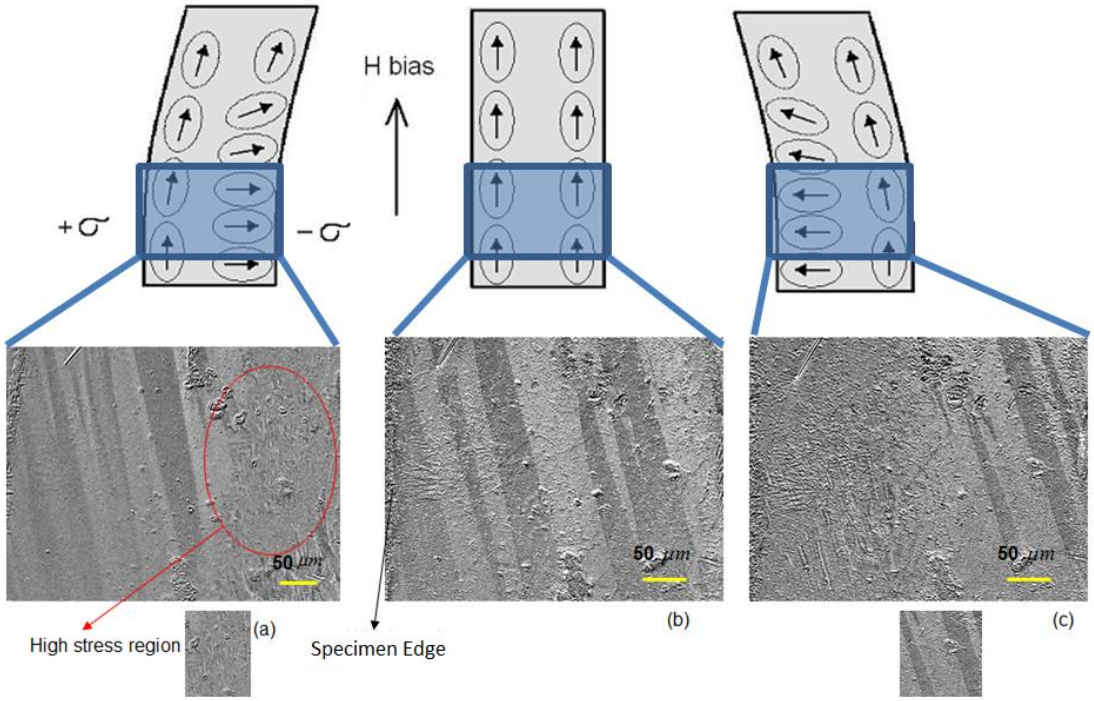

Figure 9: MOKE Microscope Images Showing Domain Rotation in Polycrystalline Annealed <100> Oriented $Fe_{81}Ga_{19}$ + 1.0% NbC under Bending

Topics to be Discussed

In this thesis, a Galfenol-based vibrissa-like sensor is designed, built, and characterized. The sensor can be used both as a tactile sensor and as a flow sensor. In chapter 2, a Galfenol whisker sensor is simulated using a bidirectionally coupled magnetoelastic model implemented in COMSOL Multiphysics software. Chapter 3 presents the development of the sensor prototype. Chapters 4 and 5 show results from tactile and flow sensing experiments. The conclusion and potential future work are found in chapter 6.

Chapter 2: Modeling & Simulation

A sensor was conceptualized based on the bending behavior of Galfenol discussed in Chapter 1. This chapter discusses the modeling and simulation that was performed to study the characteristics of Galfenol when used as a sensor. Simulations were created in COMSOL Multiphysics Software. The results, also presented in this chapter, were then used to guide the sensor design process.

Energy-Based Model

Armstrong proposed an energy-based model of magnetization that considers the total energy corresponding to a magnetization as the result of an applied stress and magnetic field. The total energy is expressed as the sum of the magnetocrystalline, magnetoelastic, and magnetic field energy terms:

$$E(\sigma, H) = E_{magnetocrystalline} + E_{magnetoelastic} + E_{magnetic}$$

The magnetocrystalline anisotropy is expressed as:

$$E_{magnetocrystalline} = K_1 * (\alpha_1^2\alpha_2^2 + \alpha_2^2\alpha_3^2 + \alpha_3^2\alpha_1^2) + K_2 * (\alpha_1^2\alpha_2^2\alpha_3^2)$$

K_1, K_2: Magnetocrystalline Anisotropy Constants

$\alpha_1, \alpha_2, \alpha_3$: Direction Cosines for Orientation of Magnetic Moment

The magnetoelastic energy is a coupling between mechanical and magnetic terms, and is expressed as:

$$E_{magnetoelastic} = -\frac{3}{2}\lambda_{100} * \sigma * (\alpha_1^2\beta_{1s}^2 + \alpha_2^2\beta_{2s}^2 + \alpha_3^2\beta_{3s}^2)$$

$$-3\lambda_{111} * \sigma * (\alpha_1\alpha_2\beta_{1s}\beta_{2s} + \alpha_2\alpha_3\beta_{2s}\beta_{3s} + \alpha_3\alpha_1\beta_{3s}\beta_{1s})$$

$\lambda_{100}, \lambda_{111}$: Magnetostriction Constants in <100> and <111> Directions

σ: Applied Stress Magnitude

$\beta_{1s}, \beta_{2s}, \beta_{3s}$: Applied Stress Direction Cosines

$\alpha_1, \alpha_2, \alpha_3$: Magnetic Moment Direction Cosines

The magnetic energy is expressed as:

$$E_{magnetic} = -\mu_0 * \mathbf{M_s} * \mathbf{H} * (\alpha_1\beta_{1F} + \alpha_2\beta_{2F} + \alpha_3\beta_{3F})$$

μ_0: Magnetic Permeability of Free Space

$\mathbf{M_s}$: Saturation Magnetization

H: Magnetic Field

$\beta_{1F}, \beta_{2F}, \beta_{3F}$: Applied Field Direction Cosines

$\alpha_1, \alpha_2, \alpha_3$: Magnetic Moment Direction Cosines

The magnetoelastic energy can be scaled by a dimensionless factor of γ_σ so that the variation in magnetic behavior with stress matches more closely to experimental results, such that:

$$E(\sigma, H) = E_{magnetocrystalline} + \gamma_\sigma * E_{magnetoelastic} + E_{magnetic}$$

Using the total energy, an ensemble average of all possible orientations of the magnetization vector is calculated to evaluate magnetization and magnetostriction. For example, the magnetization along the [100] crystallographic direction is expressed as:

$$M_x = \frac{\sum_{\theta,\phi}(M_s \sin\theta \cos\phi)(d\theta d\phi|\sin\theta|)e^{-E(\theta,\phi)/\Omega}}{\sum_{\theta,\phi}(d\theta d\phi|\sin\theta|)e^{-E(\theta,\phi)/\Omega}}$$

The magnetization along the [010] and [001] directions (M_y and M_z) can similarly be calculated. A smoothing parameter, Ω, was used to achieve desired smoothness in B-H and λ-H curves in order to match experimental results.

The magnetization along any direction could then be calculated, as well as the magnetic flux density:

$$M(\sigma, H) = M_x\beta_{1R} + M_y\beta_{2R} + M_z\beta_{3R}$$

$$B(\sigma, H) = \mu_0(M(\sigma, H) + H)$$

(Atulasimha, 2006)

Figure 10 and Figure 11 respectively show the comparison of the energy-based model predictions with experimental results, for $Fe_{84}Ga_{16}$, as an actuator and sensor under axial compression loads.

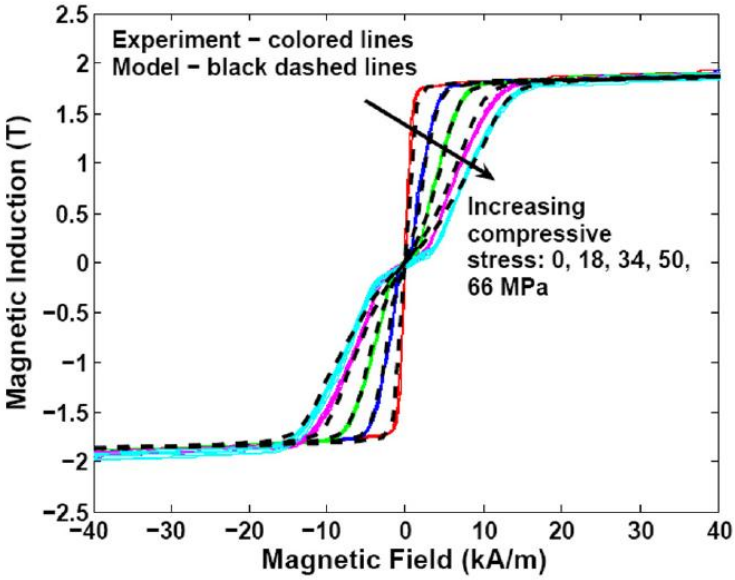

Figure 10: B-H Comparison between energy-based model (dashed lines) and experimental data (solid lines) for furnace cooled, <100> oriented, single crystal $Fe_{81}Ga_{16}$ rods of 1 inch length and .25 inch diameter under axial compressive pre-stresses (Datta, 2009)

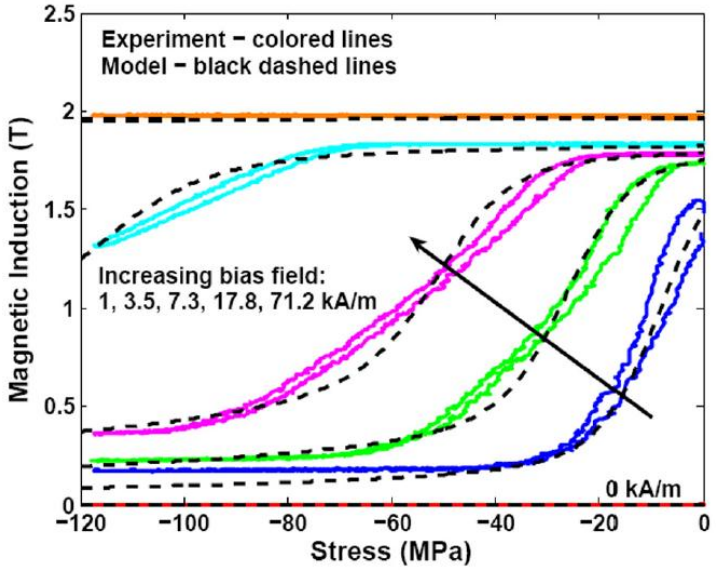

Figure 11: B-Stress Comparison between energy-based model (dashed lines) and experimental data (solid lines) for furnace cooled, <100> oriented, single crystal $Fe_{81}Ga_{16}$ rods of 1 inch length and .25 inch diameter under different DC bias magnetic fields (Datta, 2009)

Bidirectionally-Coupled Magnetoelastic Model (BCMEM)

Mudivarthi et al. presented a 3D nonlinear finite element-based model to predict the behavior of magnetostrictive materials in complex structures. The BCMEM integrates both magnetic and elastic boundary value problems.

The elastic boundary value problem (BVP) is formulated and solved using the finite element method:

$$\int_{\Omega} \delta\tilde{\varepsilon}^T \tilde{\sigma} dV - \int_{\Omega} \delta\tilde{u}^T \tilde{F}_b dV - \int_{\Omega} \delta\tilde{u}^T \tilde{F}_s dS = 0$$

$$\tilde{\varepsilon} = \{\varepsilon_{11} \quad \varepsilon_{22} \quad \varepsilon_{33} \quad \gamma_{12} \quad \gamma_{23} \quad \gamma_{31}\}^T$$

$$\tilde{\sigma} = \tilde{\mathbf{C}}(\tilde{\varepsilon} - \tilde{\lambda}(\tilde{\sigma}, \tilde{H}))$$

The magnetic boundary value problem is expressed as:

$$\int_{\Omega} \delta\tilde{H}^T \tilde{B} dV = 0$$

$$\tilde{B} = \tilde{\mu}(\tilde{\sigma}, \tilde{H})\tilde{H} + \tilde{B}_r$$

$$\tilde{\mu}(\tilde{\sigma}, \tilde{H} \neq 0) = \frac{\mu_0(\tilde{M}(\tilde{\sigma}, \tilde{H}) + \tilde{H})}{\tilde{H}}$$

The elastic and magnetic boundary value problems were solved iteratively, with the elastic BVP first solved under an assumption of a zero applied magnetic field, $\tilde{H} = \tilde{0}$. With the resulting stress distribution, the magnetization, $\tilde{M}(\tilde{\sigma}, \tilde{H})$, is calculated using the energy-based model. The magnetic boundary value problem can then be solved to obtain the magnetostriction, $\tilde{\lambda}(\tilde{\sigma}, \tilde{H})$, which is fed back into the elastic boundary value problem. The iterations continue until a convergence criterion is achieved, such as $\Delta B < 0.5\%$ and $\Delta\sigma < 0.5\%$.

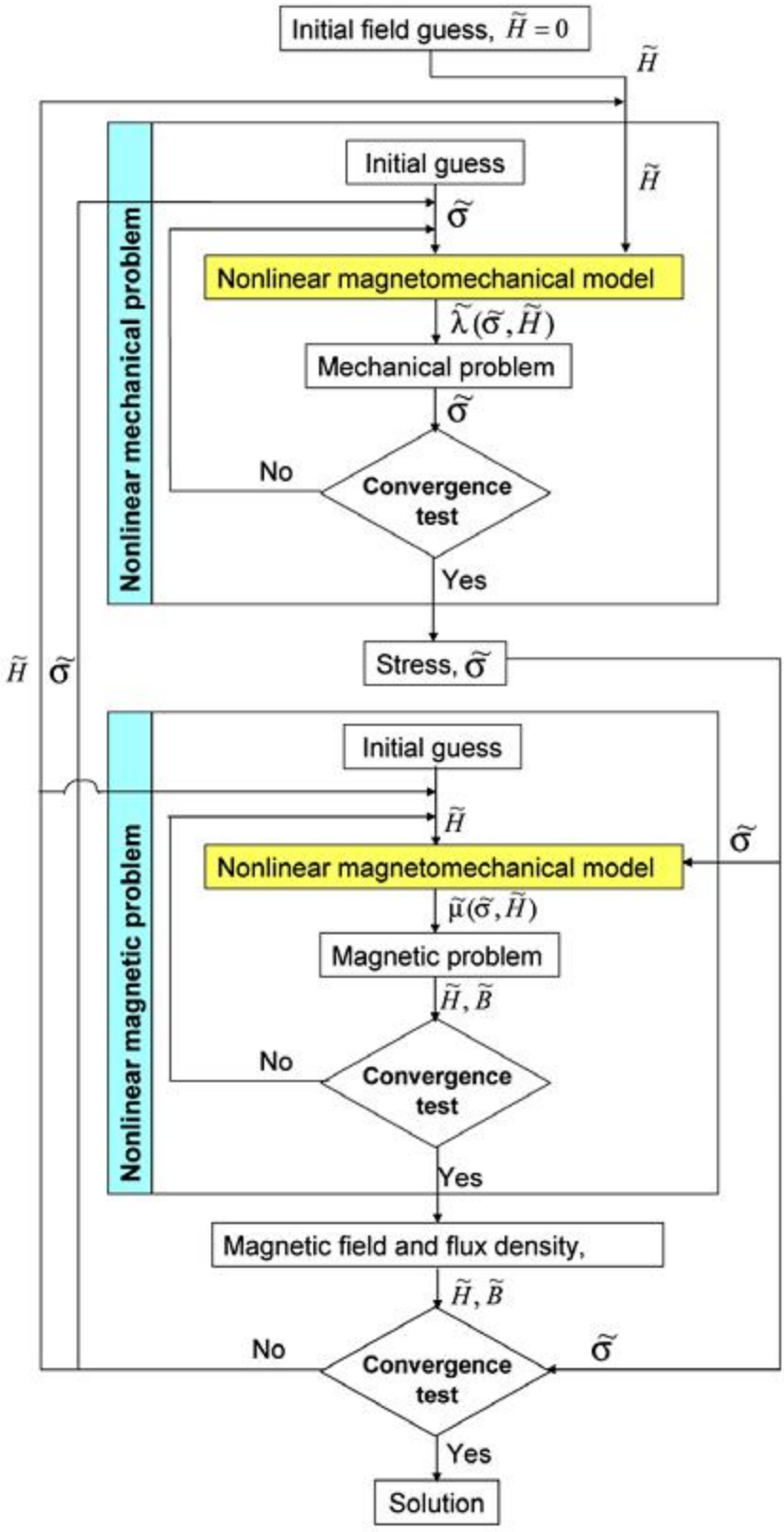

Figure 12: BCMEM Flow Chart, showing two minor iterative loops embedded in a major iterative loop (Mudivarthi, Datta, Atulasimha, & Flatau, 2008)

For the current research, the Armstrong equations of the energy-based model of magnetostriction were implemented into a MATLAB function, `armstrong_optimized.m`, which received an input of a local magnetic field ($H_{3\times1}$) and stress ($\sigma_{6\times1}$), and produced an output of local magnetic induction ($B_{3\times1}$) and magnetostriction ($\lambda_{6\times1}$). The armstrong_optimized. m MATLAB code is included in Appendix E – armstrong_optimized.m.

$$\begin{Bmatrix} H_x \\ H_y \\ H_z \end{Bmatrix}, \begin{Bmatrix} \sigma_x \\ \sigma_y \\ \sigma_z \\ \sigma_{xy} \\ \sigma_{yz} \\ \sigma_{xz} \end{Bmatrix} \rightarrow \texttt{armstrong\_optimized.m} \rightarrow \begin{Bmatrix} B_x \\ B_y \\ B_z \end{Bmatrix}, \begin{Bmatrix} \lambda_x \\ \lambda_y \\ \lambda_z \\ \lambda_{xy} \\ \lambda_{yz} \\ \lambda_{xz} \end{Bmatrix}$$

Due to the nature of cantilever beam bending, the stress in the beam is dominated by σ_x. In addition, the biasing magnet causes magnetic flux lines to run along the length of the whisker, causing the local magnetic field in the high-stress region to be dominated by H_x. Using these approximations, a database was created with a range of expected σ_x and H_x values. For each combination of every σ_x and H_x, values were calculated for λ_x and B_x. This database of stress, magnetic field, magnetostriction, and magnetic induction values was called during execution of the BCMEM in COMSOL Multiphysics software.

COMSOL 3.5a features the ability to run MATLAB alongside COMSOL. The bidirectionally-coupled magneto-elastic model was coded using the COMSOL Multiphysics programming language in a MATLAB script. The geometry for the

mechanical boundary value problem featured the whisker and surrounding epoxy layer. The geometry for the magnetic boundary value problem featured the whisker, air domain, and permanent magnet.

Approximations & Assumptions

The BCMEM used in this thesis models magneto-mechanical coupling in the x-axis only. This was considered to be a valid assumption for modeling magnetostrictives in bending. When one considers a beam in bending, the stresses are dominated by stresses that are parallel to the beam's neutral axis. For the modeling discussed in this thesis, the Galfenol specimens are modeled to be biased in the direction parallel to the neutral axis as well.

BCMEM Validations

The BCMEM was experimentally validated by Mudvarthi et al., using a unimorph structure consisting of a single-crystal $Fe_{84}Ga_{16}$ patch bonded to an aluminum cantilever beam. The Galfenol patch was biased using a .79 T permanent magnet. A strain gage was attached to the aluminum beam, and a linear Hall-effect sensor was placed adjacent to the Galfenol patch. A range of loads were applied to the free end of the cantilever. The setup was modeled using COMSOL 3.3a using the BCMEM.

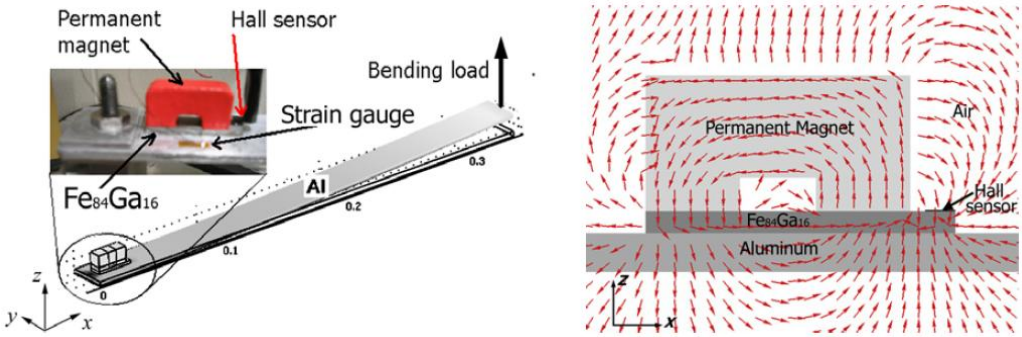

Figure 13: Schematic of BCMEM $Fe_{84}Ga_{16}$ Unimorph Validation Experiment (Mudivarthi, Datta, Atulasimha, & Flatau, 2008)

The error of the BCMEM predictions for bending strain and magnetic flux density was less than 7%. For modeling $Fe_{84}Ga_{16}$, the following parameters were used:

Cubic Magnetocrystalline Anisotropy Constants

$K_1 = 13$ kJ m^{-3}

$K_2 = -90$ kJ m^{-3}

Experimentally Determined Magnetostrictive Constants

$\lambda_{100} = 165 \times 10^{-6}$

$\lambda_{111} = -13 \times 10^{-6}$

Saturation Magnetization

$M_s = 1456$ kA m^{-1}

Armstrong Smoothing Factor

$\Omega = 600$

Dimensionless Linear Correction Constant

$\gamma_\sigma = 0.875$

(Mudivarthi, Datta, Atulasimha, & Flatau, 2008).

Modeling a Galfenol Bending Sensor using the BCMEM

According to the research discussed in (Downey P. R., 2008), a magnetically biased Galfenol beam has a change in magnetization due to a change in bending stresses in the beam. The change in magnetization can be detected by measuring the changing magnetic field in air close to the high-stress region of the bending Galfenol beam.

For the current project, a prototype Galfenol-based sensor was modeled as follows: a flexible Galfenol whisker-like specimen was cantilevered at one end and exposed to tactile and drag forces at the free end. The design called for the Galfenol whisker to be biased by a permanent magnet, rather than an electromagnet in order to reduce the power requirements and complexity of the sensor. A sensor to detect the magnetic field variations was designed to be as close as possible to the high-stress regions of a bending Galfenol whisker in order to be as sensitive as possible to magnetization changes in the whisker. This resulted in a sensor layout, shown in Figure 14, where a portion of the Galfenol whisker is cantilevered with a GMR sensor and a permanent magnet, with the free portion of the whisker available to be exposed to external forces.

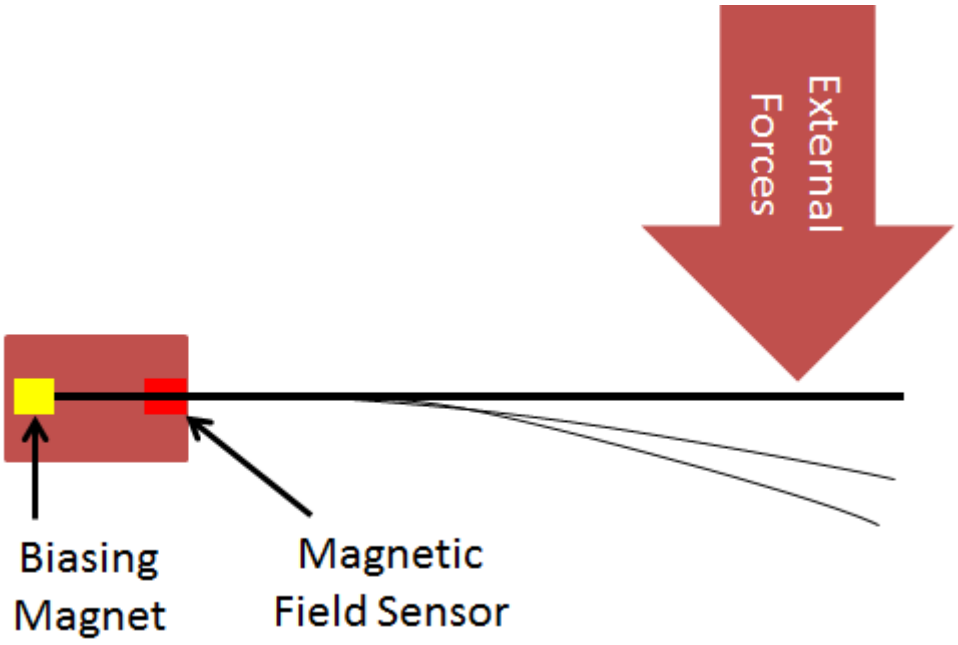

Figure 14: Whisker Prototype Sensor Layout Depicting Biasing Magnet and Field Sensor Locations

Modeling the conceptualized sensor design would show the simultaneous tensile and compressive axial strains in the modeled Galfenol sample during bending, and its overall effect on magnetization.

The BCMEM was applied to a structure consisting of a cantilevered $Fe_{84}Ga_{16}$ beam to model Galfenol-based bending sensors. The prototype Galfenol sensor used whiskers cut from a heat-treated Galfenol rolled sheet; however, the BCMEM validations were for single-crystal $Fe_{84}Ga_{16}$, so the composition for the discussed modeling was the same single-crystal Galfenol composition.

The rolled sheet Galfenol composition could not be modeled because of the lack of sufficient magnetic and mechanical characterizations to determine necessary coefficients for the energy model previously discussed. The prototype Galfenol whisker used a polycrystal Galfenol ingot to manufacture the rolled sheet rather than a single-crystal specimen to keep the cost low. Although direct comparisons between

the Galfenol sensor modeling and testing could not be made, it was assumed that the lessons learned from modeling & simulation would carry over to whiskers of different compositions.

Model Geometry

The beam's width and thickness of .6 mm came from the final thickness of the rolled sheet after the annealing process when manufacturing the actual Galfenol whiskers. Although the prototype Galfenol whisker had a beam length of 19 cm, the modeled beam was 4 cm long to cut down on computation time, since the high-stress region would be located close to the part of the beam that transitions from free to fixed boundary conditions. Half of the beam was fixed, and half of the beam was free. A range of positive and negative loads were applied to the free tip of the beam.

Biasing Magnet

The beam was magnetically biased by modeling a .6 mm x .6 mm x .6 mm cube-shaped permanent magnet. The magnet was placed at the end of the whisker, in line with the whisker's neutral axis. The permanent magnet was modeled to have remnant magnetizations of .75 T and 1.25 T.

Meshing

Although a structured mesh may have provided faster and more accurate results in areas of interest, the BCMEM was created to accommodate potentially complex geometries, where structured meshes would not be ideal. Future refinement of a bio-inspired sensor is expected to have much more complex geometries; thus, meshing of the prototype whisker sensor was done using the unstructured mesh

algorithms in COMSOL 3.5a. The meshing parameters are shown in Appendix C – Creating the COMSOL Geometries.

Whisker Axes

The x-axis is defined as the neutral axis of the straight whisker, starting from the end of the fixed portion of the whisker, pointing in the direction of the free end of the whisker.

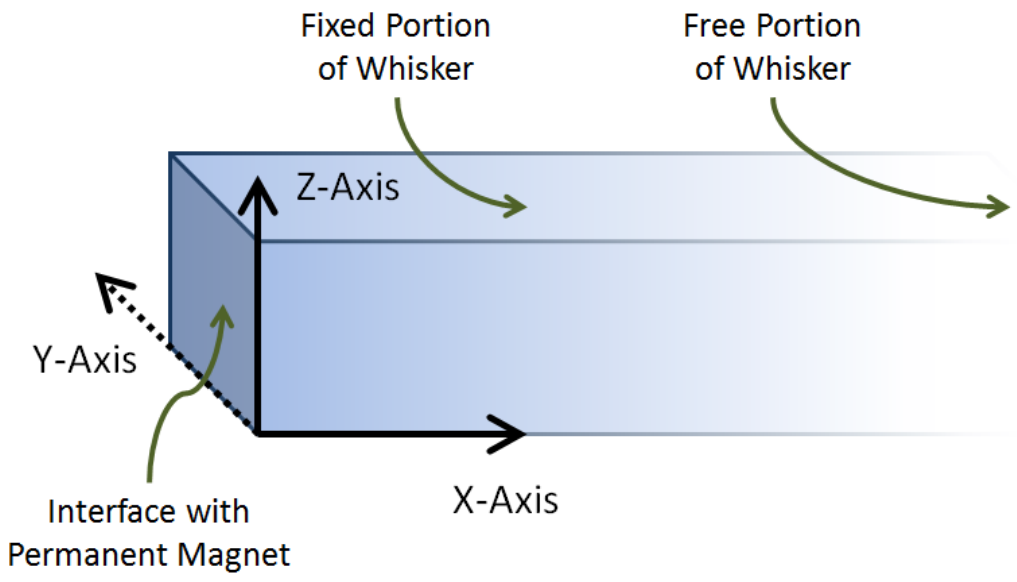

Figure 15: Whisker Axes in COMSOL

Modeling the Geometry in COMSOL

The BCMEM calls for modeling the mechanical and magnetic geometries separately. The mechanical geometry features the whisker, the fixed boundary conditions, the free boundary conditions, and a tip force of various magnitudes and directions, as shown in Appendix C – Creating the COMSOL Geometries.

The magnetic geometry features the whisker, biasing magnet, the surrounding air, and corresponding magnetic boundary conditions, as shown in Appendix C – Creating the COMSOL Geometries.

Results

As expected, the highest stresses and strains occurred near the fixed section of the whisker. The bending caused stresses that changed from compressive to tensile through the thickness of the whisker, as seen in Figure 16 and Figure 17.

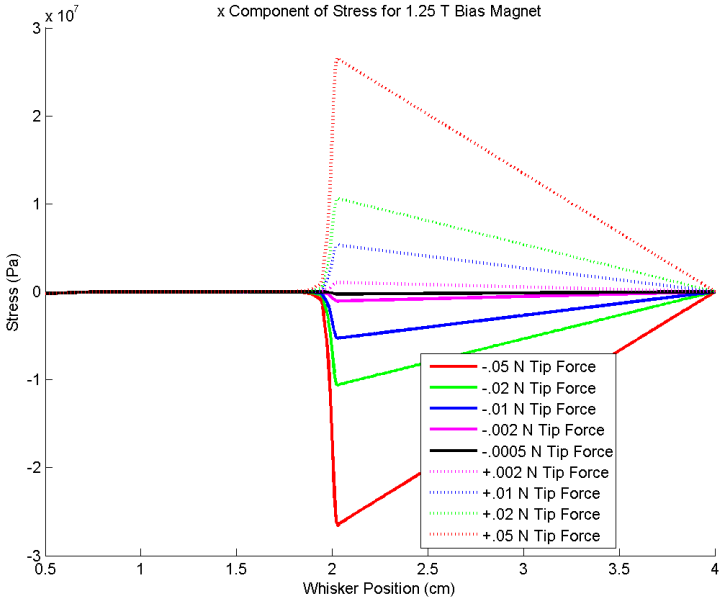

Figure 16: x-Component of Stress at Bottom of Whisker

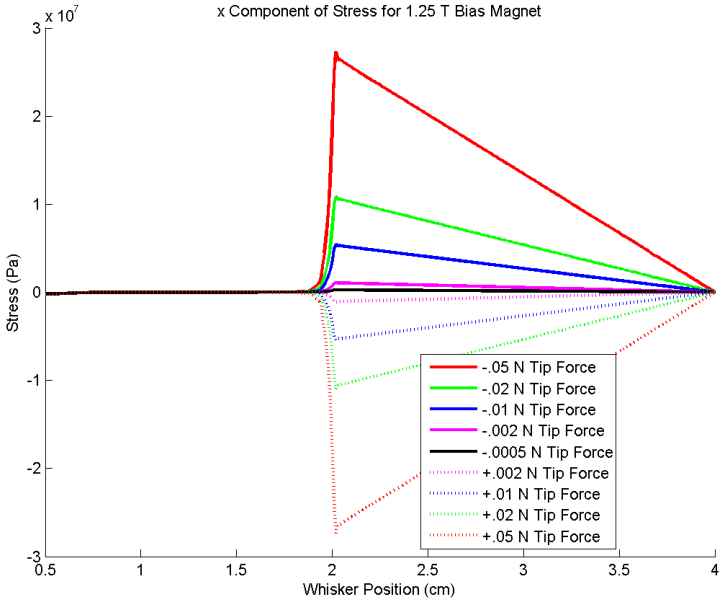

Figure 17: x-Component of Stress at Top of Whisker

The BCMEM predicted changes in relative permeability and magnetization that were greatest in the high-stress region of the cantilevered Galfenol beam. This change permeability resulted in changes of the magnetic field that were greatest close to the high-stress region. Figure 18 shows the x-component of the B field along the bottom surface of the whisker. The tip forces in the direction of the negative z-axis cause compressive stresses at the bottom of the whisker. The domains rotate, and a low flux density results. For tip forces in the direction of the positive z-axis, a higher flux density is shown. It is assumed that the modeled permanent magnet did not sufficiently bias the whisker; therefore, the domains were not fully aligned, and a magnetic field change is shown for the bottom of the whisker, as tensile stresses further align the domains. The reverse is shown for the top of the whisker, as shown in Figure 19.

Results for a biasing magnet strength of .75 T is shown in Appendix F – COMSOL Results of .75 T Bias Magnet.

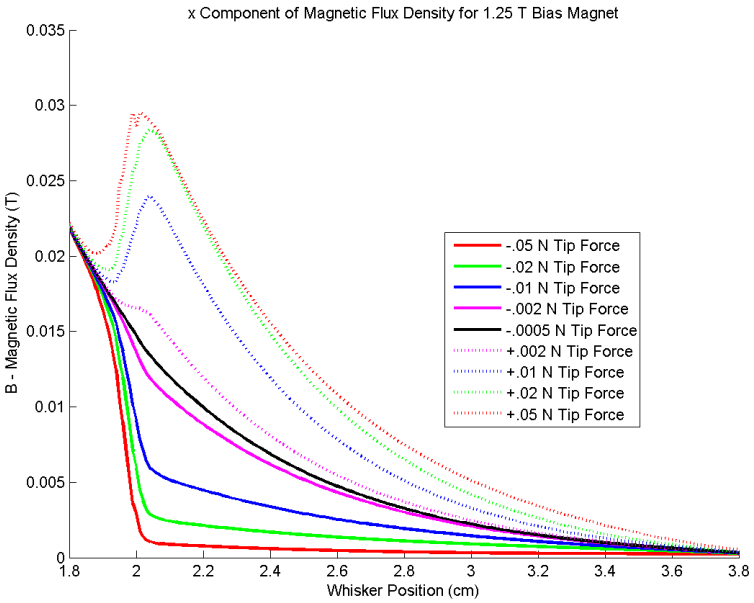

Figure 18: x-Component of B Field for 1.25 T Bias Magnet - Bottom of Whisker

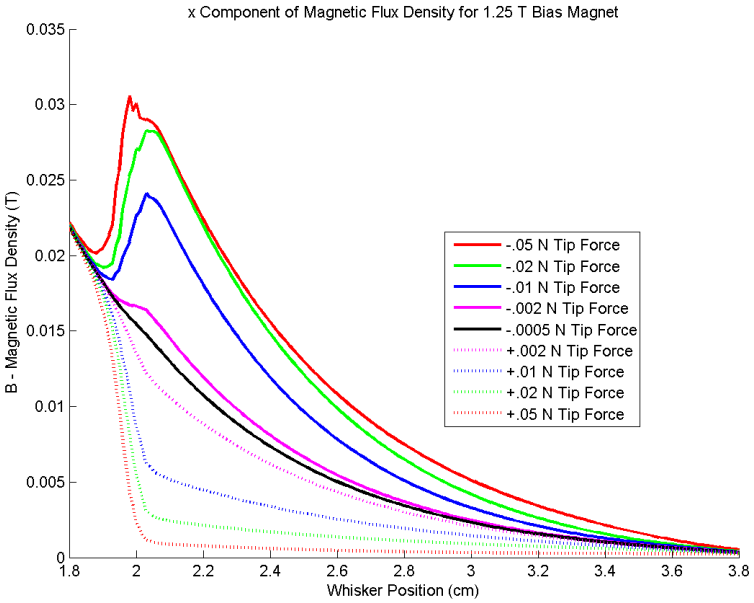

Figure 19: x-Component of B Field for 1.25 T Bias Magnet - Top of Whisker

Modeling of a Galfenol-based bending sensor aided in the process of designing the sensor prototype. Since the highest changes in magnetization would occur near the high stress regions in a bent whisker, a magnetic field sensor would need to be placed as close as possible to the high stress region in order to detect the changes in magnetization.

It was also observed that the strength and location of the biasing magnet is important to the sensing ability of the sensor. A permanent magnet that is weak or far away from the whisker's high stress region would weakly align the domains, and the magnetization change would saturate at low bending stresses due to small bending displacements. On the other hand, a permanent magnet that is strong or close to the high stress region would cause the whisker to require large bending displacements for a magnetization change to be detected.

Results from the simulations provided two important insights that guided design iterations:

- The largest changes in magnetization occurred in the high-stress region near the interface between the fixed portion of the beam and the free portion of the beam. Thus, the magnetic field sensor should be placed as close as possible to this location.
- The placement and strength of the biasing magnet plays a critical role in the effectiveness of the sensor – the magnetic field cannot be too strong or too weak

Chapter 3: Prototype Development

A whisker-like prototype sensor was developed. A Galfenol 'whisker' was cantilevered in an aluminum base with a permanent magnet to align the domains along the length of the whisker. A giant magnetoresistance (GMR) sensor was also fixed to the aluminum base to detect magnetic field changes resulting from whisker bending. The whisker could be bent by various external stimuli such as tactile forces or fluid flow drag forces.

Whisker Preparation

Galfenol Composition

While single-crystal Galfenol specimens exhibit greater magnetostrictive properties, a polycrystalline whisker was desired for mechanical properties that would be optimal for bending. A polycrystalline Galfenol specimen was hot rolled into a rolled sheet. Niobium Carbide was used as an alloying addition in order to suppress cracking along grain boundaries during rolling. (Na, Yoo, & Flatau, 2009)

A polycrystalline Galfenol ($Fe_{81}Ga_{19}$ + 1.0% NbC) ingot was produced by ETREMA Products, Inc.

Annealing & Rolling Process

The manufacturing of the prototype Galfenol whisker started with a Galfenol ($Fe_{81}Ga_{19}$ + 1.0% NbC) ingot produced by ETREMA Products, Inc. The ingot was hot rolled at 900º C, changing the thickness from 15 mm to 7.57 mm, for a reduction rate of 49.5%. The specimen was hot rolled again at 700º C, reducing the thickness

86.3% to 1.04 mm. A final warm rolling at 400º C resulted in a reduction rate of 42.3%. The resulting rolled sheet of thickness 0.60 mm.

Prior to the rolling process, the Galfenol ingot had random grain orientations. The rolled sheet had mainly fiber textures of lower energy states, which was undesirable for magnetostrictive performance. In order to create grain orientations that would maximize magnetostrictive performance, the rolled sheet was then annealed in flowing Argon gas at 1200º C for 2 hours. Annealing caused Goss texture {110}<001> in the rolled sheet, aligning the <100> magnetic easy axis parallel to the rolling direction. The result was an increase in magnetostriction.

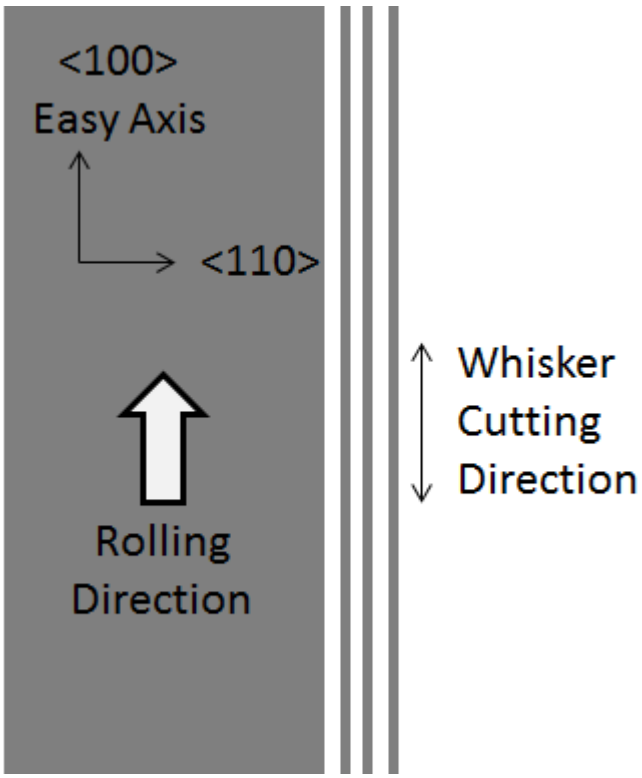

Figure 20: Schematic of Whisker Rolling, Cutting, and Orientation Directions

After the rolling and annealing processes, the Galfenol rolled sheet cut into whiskers using wire electrical discharge machining. Each whisker had a .6 mm x .6 mm square cross-section, and a 19 cm length.

Characterization of Mechanical Properties

Tensile testing of single-crystal Galfenol dogbone-shaped specimens was conducted by Holly Schurter. The dogbone specimens had the dimensions depicted in Figure 21. A gripper was fabricated from 1018 steel, and attached to an MTS Model 810 Material Test System. The dogbone samples were installed in the gripper, and axial loads were applied through the MTS system. Axial and transverse strain gages were attached to opposite faces of the dogbones in order to calculate the elastic properties of each sample. (Schurter, 2009)

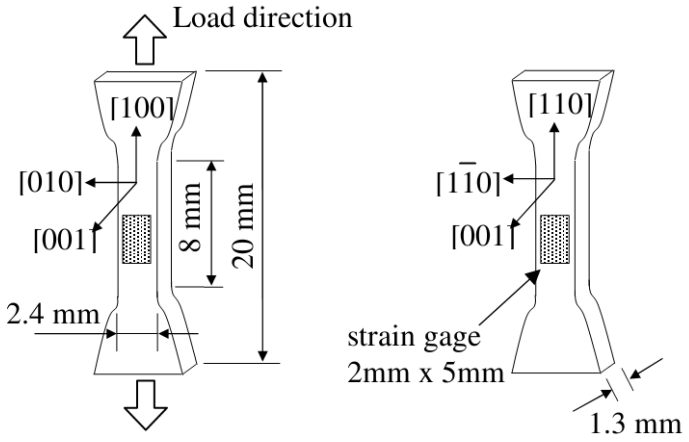

Figure 21: Schematic of the [100] and [110] Fe-Ga dogbone tensile samples tested by Schurter (Schurter, 2009)

Characterization of mechanical properties of the Galfenol whisker was done on a specimen that was cut from the same heat-treated rolled sheet as the whisker. The specimen was cut in a dogbone shape, as shown in Figure 22. The dogbones had

similar dimensions to those depicted in Figure 21, but the samples had a thickness of .6 mm.

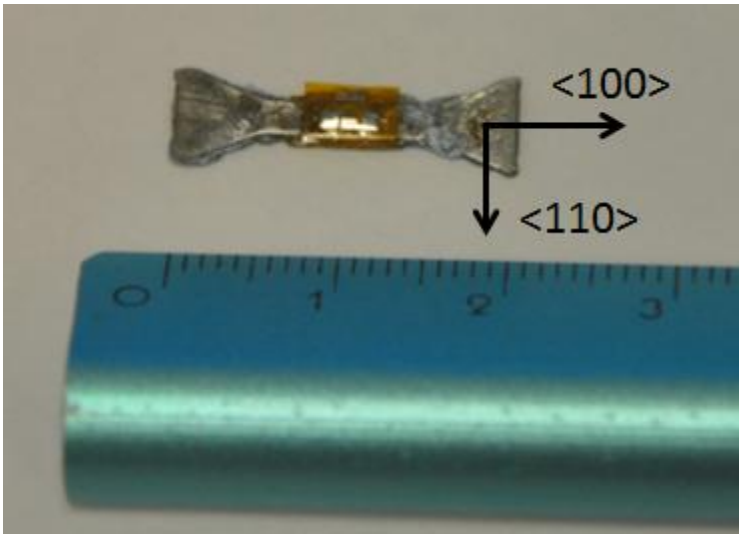

Figure 22: Dogbone Cut from Rolled Sheet of Polycrystalline $Fe_{81}Ga_{19}$ + 1.0% NbC

Axial and transverse strain gages were mounted on opposite sides of the dogbone face. Axial forces were applied along the length of the dogbone using the MTS Model 810 Material Test System to determine the Young's modulus, Poisson's ratio, and yield strength. From the mechanical characterization tests done on the sample, there was no observable plastic deformation. The dogbone sample fractured at a stress of 422.1 MPa, and an axial strain of 7919 $\mu\varepsilon$. The Young's modulus was calculated from the inverse of the slope of the linear fit in Figure 23.

$$E = \frac{tensile\ stress}{tensile\ strain} = \frac{\sigma}{\varepsilon} = 54.4 \times 10^9 \text{ Pa}$$

Poisson's ratio was calculated:

$$\nu = \frac{-transverse\ strain}{axial\ strain} = .58$$

A Poisson's ratio greater than .5 was unexpected. Further investigation is warranted, especially given the auxetic behavior of Galfenol in certain orientations, as observed by Schurter. (Schurter, 2009)

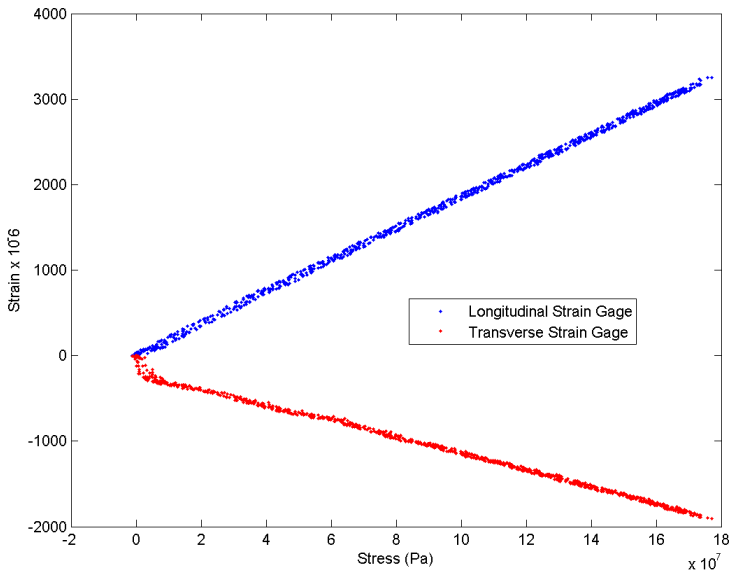

Figure 23: Longitudinal & Transverse Strains of Dogbone Cut from Rolled Sheet of Polycrystalline $Fe_{81}Ga_{19}$ + 1.0% NbC

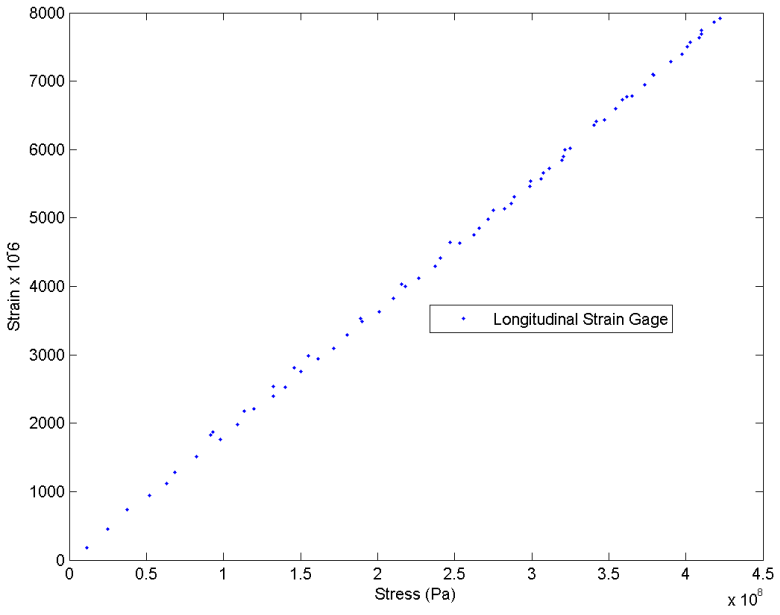

Figure 24: Ultimate Tensile Strength of Dogbone Cut from Rolled Sheet of Polycrystalline $Fe_{81}Ga_{19}$ + 1.0% NbC

The validity of the ultimate tensile strength is in question. The dogbone fractured at the edge of the constant stress range, as shown in Figure 25. An ANSYS model created by Schurter depicts concentrated tensile stresses in the region at the edge of the constant stress range (Schurter, 2009). It is thought that the dogbones were cut such that concentrated tensile loads depicted by Schurter's ANSYS model caused premature fracturing, resulting in the data not depicting the true ultimate tensile strength of the whisker material. Further characterization of the mechanical properties of the whisker material is needed in the future.

Figure 25: Fractured Sample of Dogbone Cut from Rolled Sheet of Polycrystalline $Fe_{81}Ga_{19}$ + 1.0% NbC

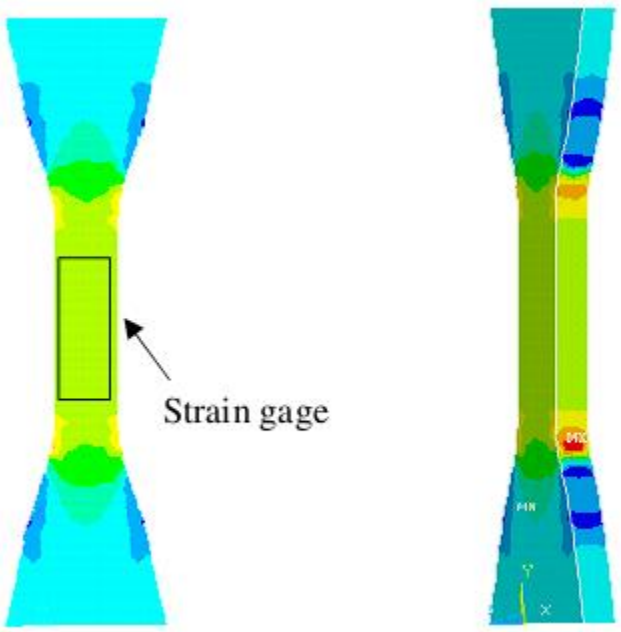

Figure 26: ANSYS Model of Tensile Stress in Dogbone (Schurter, 2009)

Characterization of Magnetostrictive Properties

Characterization of magnetostrictive properties was done on a dogbone specimen cut from the same heat-treated rolled sheet. The dogbone specimen had axial and transverse strain gages mounted on opposite sides of the dogbone face. The dogbone was mounted inside an electromagnet. The length of the dogbone was oriented parallel to the magnetic field lines. The magnetic field was varied between negative 1000 Gauss to 1000 Gauss.

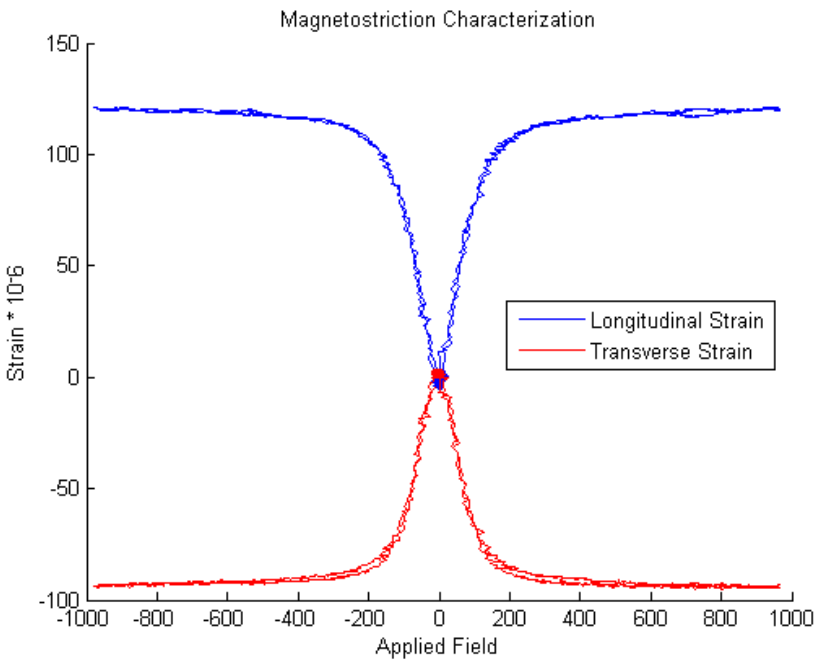

Figure 27: Longitudinal & Transverse Magnetostriction of Dogbone Cut from Rolled Sheet of Polycrystalline $Fe_{81}Ga_{19}$ + 1.0% NbC

Sensor Component Layout

GMR Sensor

Modeling of a Galfenol-based bending sensor illustrated the necessity to place a magnetic field sensor as close as possible to the high-stress region of the Galfenol beam to indicate the most magnetization change.

A commercial off-the-shelf giant magnetoresistance (GMR) sensor was used as the magnetic field sensor. The GMR sensor needed to be sensitive enough to detect variations in magnetic field due to magnetization changes in the Galfenol whisker, while having a high-enough field range of operation to not be saturated by the biasing magnet. Low-hysteresis characteristics were desirable as well. The selected GMR sensor was the NVE AAL002-02.

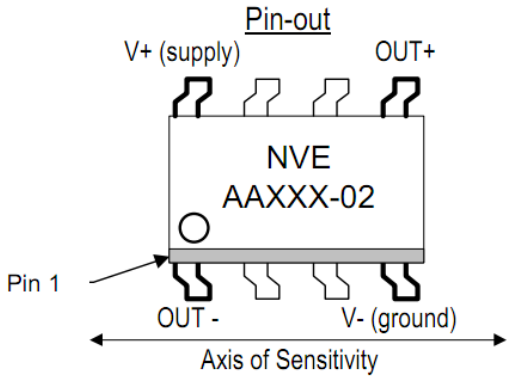

Figure 28: Schematic of NVE GMR Sensor used in Whisker Sensor (NVE Corporation)

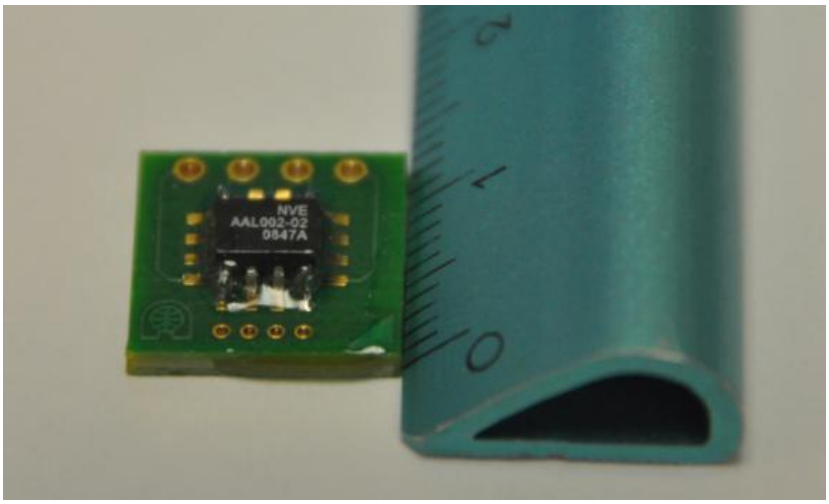

Figure 29: NVE AAL002-02 GMR Sensor on Circuit Board

The GMR sensor was soldered to a printed circuit board (13 mm length x 13 mm width x 2 mm height), as shown in Figure 29. The GMR sensor circuit included a Burr Brown INA118 instrumentation amplifier. The circuit that was implemented was similar to the one described in (NVE Corporation).

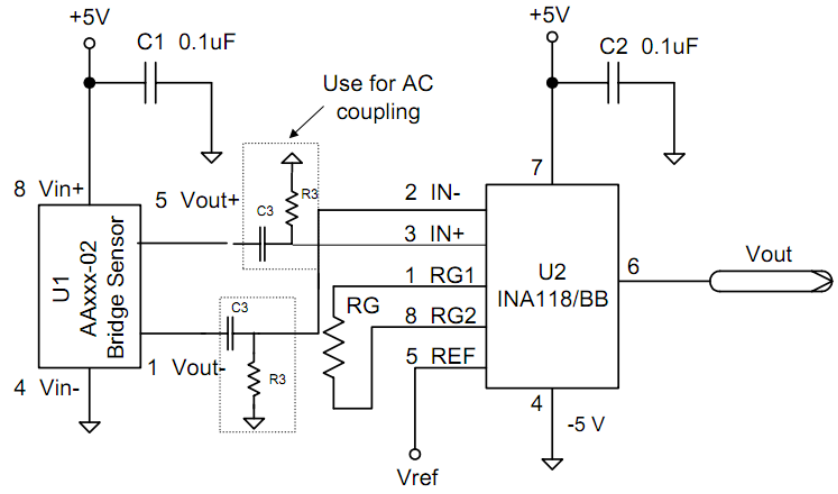

Figure 30: GMR Sensor Circuit (NVE Corporation)

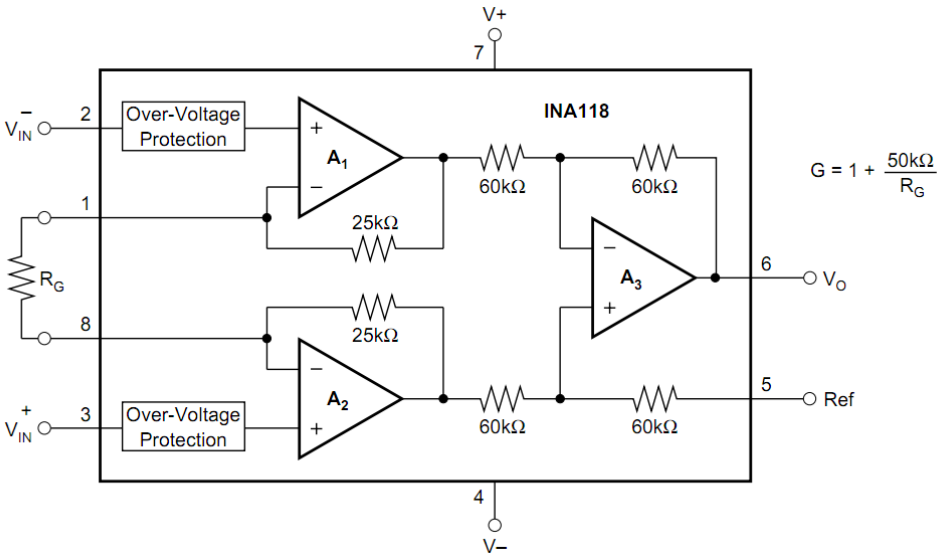

Figure 31: INA118P Instrumentation Amplifier Circuit Schematic (Burr-Brown Corporation, 1994)

The GMR sensor was calibrated by attaching the GMR sensor to a F.W. Bell Model 5080 Gauss/Teslameter probe.

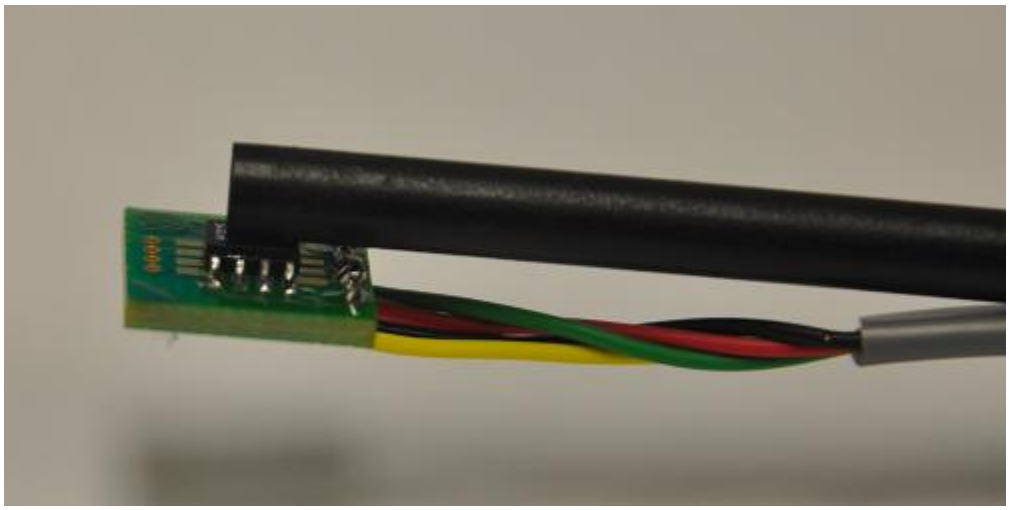

Figure 32: Calibrating NVE AAL002-02 GMR Sensor with Gaussmeter Probe

The GMR sensor and gaussmeter were inserted into a magnetic coil. Current was varied to obtain a range of magnetic field strengths. The magnetic field strength was measured with the fluxmeter probe, and a corresponding GMR voltage was the output of the GMR sensor circuit. The GMR sensor began to saturate around 2.5 mT.

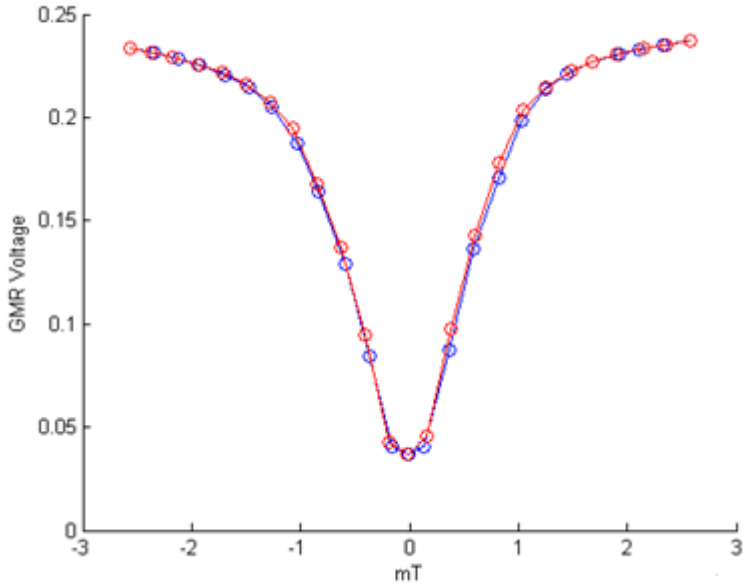

Figure 33: GMR Calibration Showing Voltage Output of GMR Sensor Circuit vs. Applied External Field Along the GMR Axis of Sensitivity

Cantilevering the Whisker

Epoxy was used to secure the GMR sensor to the whisker. The GMR axis of sensitivity was oriented in the same axis pointing along the length of the whisker.

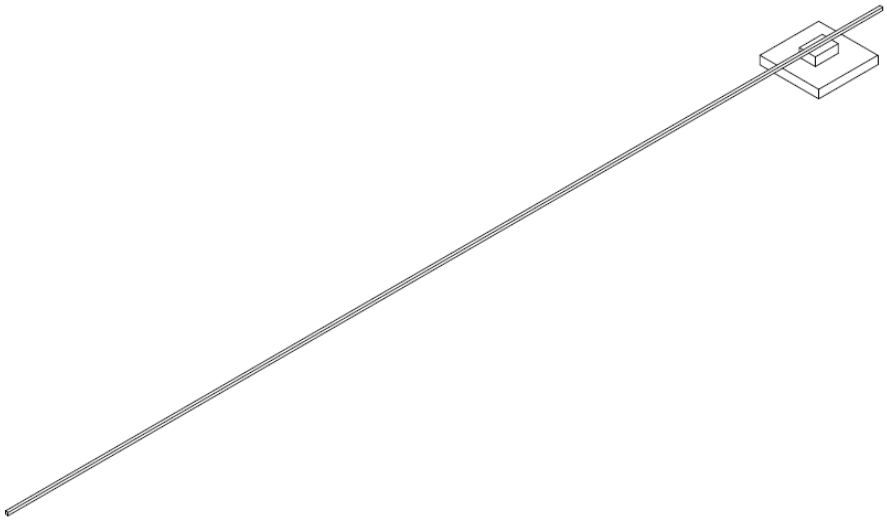

Figure 34: Mounting Whisker on GMR Chip

Upon curing, another application of epoxy secured the GMR-whisker-assembly to an aluminum base of 20 mm length x 25 mm width x 12.3 mm height. Approximately 25 mm of the whisker was fixed to the aluminum base, while the remainder of the whisker was free to be exposed to external forces.

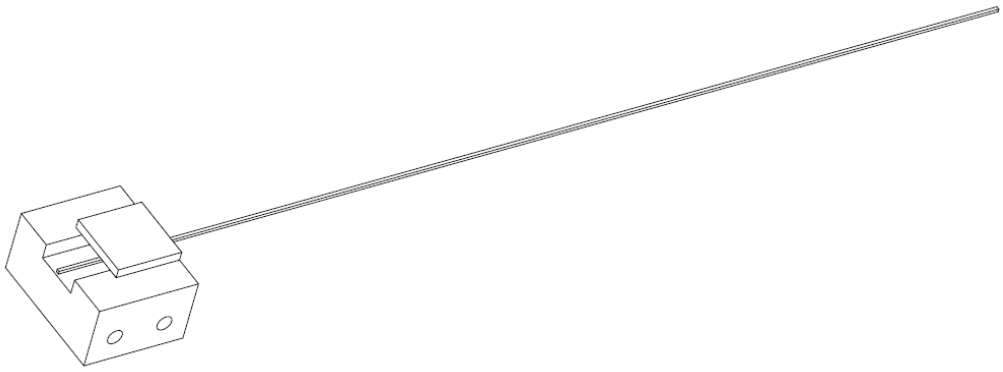

Figure 35: Mounting Whisker-GMR Assembly on Aluminum Base

The epoxy used was Loctite Heavy Duty Epoxy. The hardness of the epoxy after a 24 hour cure is Shore D 76$\pm$1 (Loctite, 2011). The equivalent Young's modulus in units of Pa $\times 10^6$ is calculated with the linear relation:

$\log_{10} E = 0.0235S - 0.6403$, where $S = S_D + 50$.

For $S_D = 76$, the equivalent Young's modulus of the epoxy is approximately $E = 210$ MPa.

Placement of the Biasing Magnet

A permanent magnet was used to bias the magnetic domains along the length of the whisker. The magnet needed to be close enough to align the domains of the whisker; however, the magnet could not be too close to the high-stress region in order to allow for domain rotation at small bending compressions. The magnet also had to

be far enough away from the GMR sensor so as not to saturate the GMR sensor's field range of operation. The optimal strength and placement of the magnet was determined using experiments described in chapter 4.

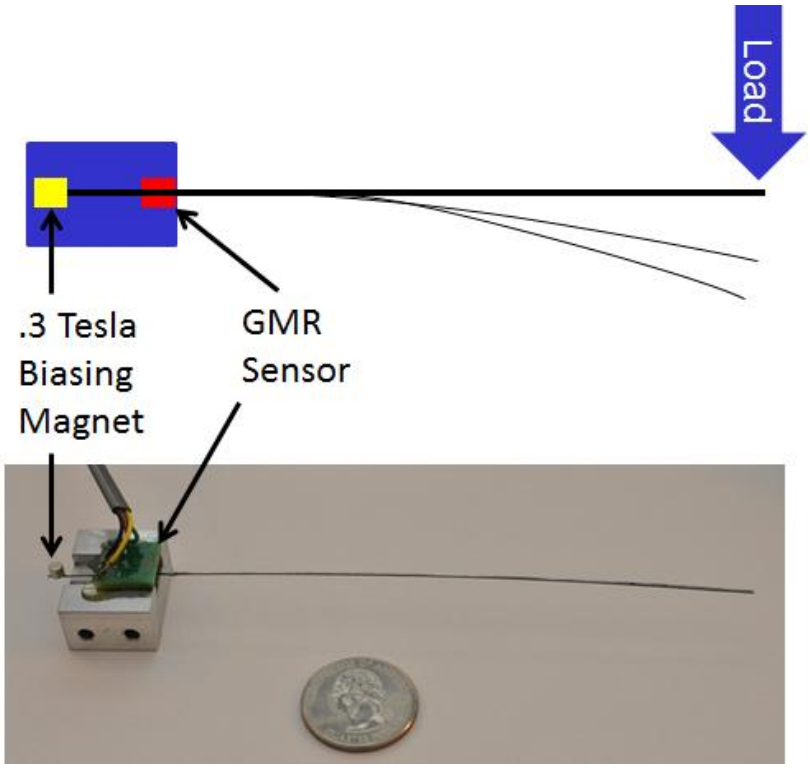

Figure 36: Prototype Whisker Sensor Schematic

Early Prototypes

The prototype that was discussed in this chapter was the one used in the experiments in Chapter 4 and Chapter 5. Several earlier prototypes were built; however, they had several issues that called for a redesign. All of the prototypes had the permanent magnet and GMR sensor placed with the fixed portion of the whisker.

With the first prototype, the GMR sensor, permanent magnet, and part of the whisker were immersed in a polydimethylsiloxane (PDMS) solution. The prototype's GMR sensor detected a varying magnetic field with whisker deflections. However,

the permanent magnet was fixed inside the PDMS, so studies could not easily be performed to observe the effect of the permanent magnet placement.

The second prototype featured the GMR sensor, permanent magnet, and part of the whisker being fixed between two rubber sheets, each backed by rigid plastic. The plastic and rubber sheets were bolted together, squeezing the whisker between the rubber sheets, as shown in Figure 69 and Figure 70 of Appendix G – Previous Whisker Sensor Prototypes. The permanent magnet could be placed in different positions along the whisker; however, it was found during static bending tests that the whisker would slowly slip between the two rubber sheets (Figure 71), despite how much the bolts were tightened.

The third prototype, shown in Figure 72, fixed the whisker with the GMR sensor using the same epoxy that was used in the final prototype design. The permanent magnet could be moved with respect to the whisker, once the epoxy dried; however, the epoxy coated the entire whisker, decreasing the amount of magnetic biasing that the magnet could provide, because the magnet could not make direct contact with the whisker.

With the lessons learned from the first three prototypes, the final prototype design was manufactured and tested.

Chapter 4: Tactile Bending Experiments

Bending experiments were conducted on the whisker sensor. The sensor was fixed to a surface, while the whisker tip was displaced. The tip displacement caused bending in the whisker, resulting in a net magnetization change, especially in the high-stress region of the whisker. The GMR sensor attached to the fixed portion of the whisker detected the resulting magnetic field change around the whisker. The GMR sensing circuit produced a voltage change that was recorded in a LabVIEW data acquisition system.

Experimental Setup

Resistive Position Transducer

A novotechnik T 100 position transducer was used to apply measured displacements to the tip of the whisker. The sensor measures a displacement range of 100 mm and has a nominal resistance of 5 kΩ (novotechnik, 2007). The resistive displacement sensor was built into a voltage divider circuit. The circuit had an input voltage of 3 V. A +5 V excitation was provided to the voltage divider circuit.

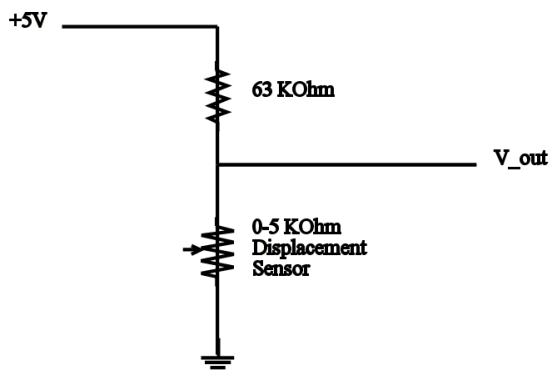

Figure 37: Position Transducer Circuit

Data Acquisition System

LabVIEW 8.5 was used in conjunction with a National Instruments USB-6212 BNC data acquisition module. The LabVIEW-based DAQ system provided a +5 V excitation for both the GMR circuit and the displacement sensor circuit, and recorded the voltage outputs of both circuits as well.

Results

Displacement Sweeps

A number of experiments were performed to characterize the tactile bending behavior and response of the whisker sensor. The whisker holder was fixed to a surface. The position transducer was placed perpendicular to the straight whisker, near the tip of the whisker. The whisker tip was displaced approximately 68 mm in the perpendicular direction to the neutral position of the whisker. Data was recorded for both the displacement sensor and the GMR voltage return.

To assess the importance of the strength and location of the permanent magnet in the fixed portion of the whisker, tests were conducted with two permanent magnets of different strengths of .3 T and .67 T. For each magnet, nine locations were tested. The farthest magnet placement is shown in Figure 38, with the edge of each magnet being 16 mm away from the GMR circuit board. The closest magnet placement is shown in Figure 39, with it being adjacent to the GMR circuit board.

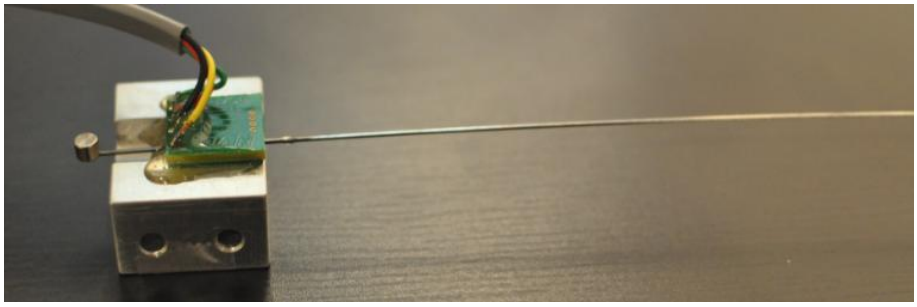

Figure 38: Prototype Whisker Sensor with Far Placement of Bias Magnet

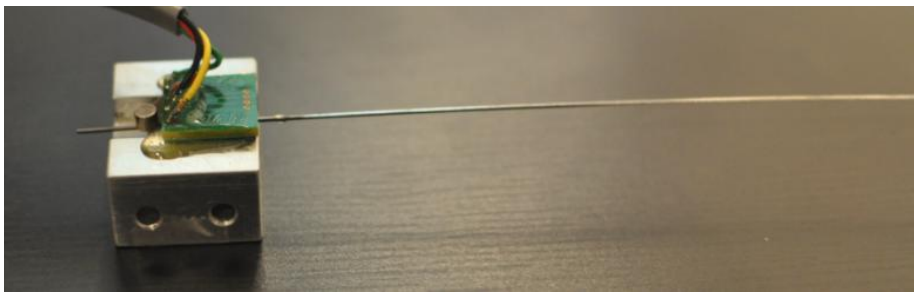

Figure 39: Prototype Whisker Sensor with Close Placement of Bias Magnet

The permanent magnet started out 16 mm from the back of the GMR sensor circuit board. Data was recorded as the displacement arm applied bending to the whisker (upsweep), and as the whisker was returned to the neutral position (downsweep). The magnet was then moved 2 mm closer to the GMR sensor circuit board. The resulting 18 plots (9 positions for each of the two magnets) are shown in Appendix H – Effect of Permanent Magnet Placement (.3 Tesla) and Appendix I – Effect of Permanent Magnet Placement (.67 Tesla).

As either of the magnets is moved closer, the GMR sensor picks up a magnetic field, resulting in an increase in the GMR output voltage. When the .3 T magnet was placed far from the GMR sensor, very low variations in magnetic field were observed. As the .3 T magnet was brought closer to the high-stress region of the whisker, larger variations of magnetic field could be observed. With stronger biasing fields (e.g. where the .3 T magnet was touching the GMR sensor circuit board, or when the .67 T magnet was used), there was a noticeable increase in noise in the GMR voltage signal. Eventually, when the .67 T magnet was brought close to the GMR sensor circuit board, the GMR sensor became saturated, and could no longer pick up variations in magnetic field as the whisker was deflected. Figure 40 shows the effect of increasing the bias field as the whisker is deflected.

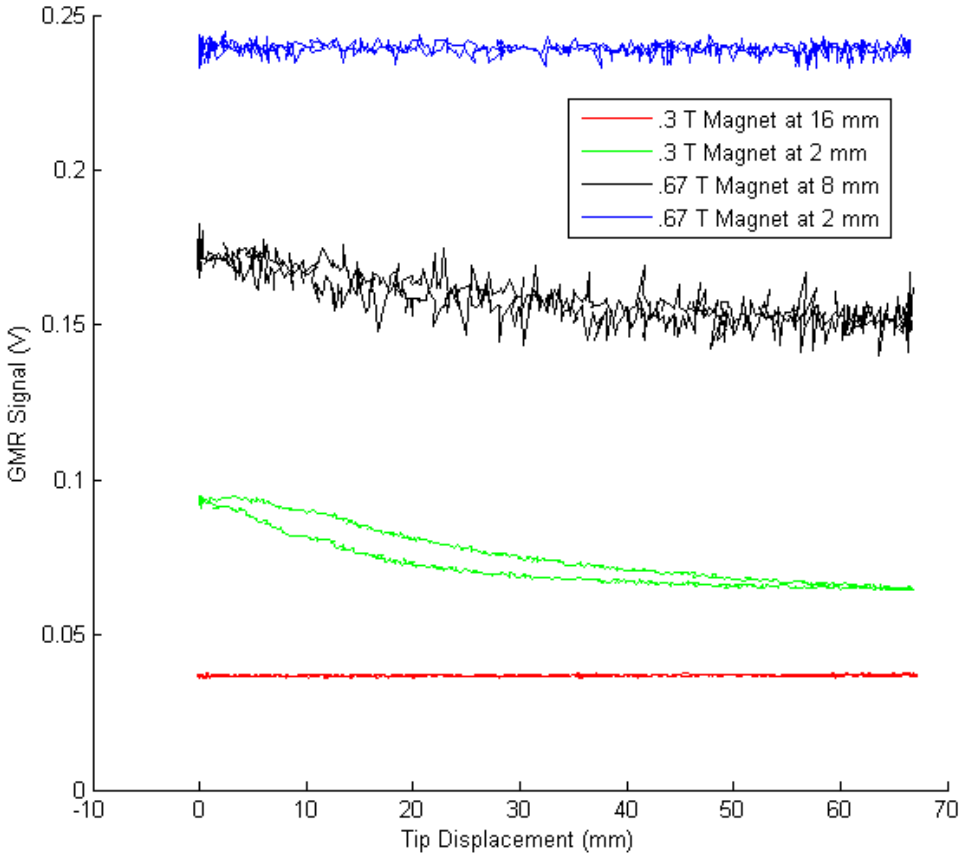

Figure 40: Effect of Increasing Bias Field using Different Magnet Strengths and Different Magnet Locations

It was found that the maximum GMR signal change occurred when the .3 T permanent magnet was 2 mm behind the back of the GMR sensor circuit board, for a tip displacement of 0 to 68 centimeters. This corresponded to a GMR sensor signal of .09 volts when the whisker was in the neutral position. The .3 T permanent magnet was then fixed to that position for future tests for optimal sensor sensitivity.

Multi-Directional Displacement

The ‘sweep’ tests were conducted in four different directions, as the whisker tip was displaced in the positive and negative y and z axes. Based on the 'optimal' permanent magnet strength of .3 T and placement of 2 mm from the back of the GMR

sensor circuit board, an estimated sensitivity was determined from the tip displacement sweep tests. Due to hysteresis, the sensor has a tip displacement uncertainty of up to +/- 5 mm. For example, at a GMR voltage change of -.03 V, assuming bending in the +z direction, the displacement could be between 35 mm or 45 mm, depending on whether the tip movement was on the upsweep or downsweep. Thus, one could conclude that at a GMR voltage change of -.03 V, the displacement is 40 +/- 5 mm. The uncertainty decreases at low tip displacements around 0 to 20 mm.

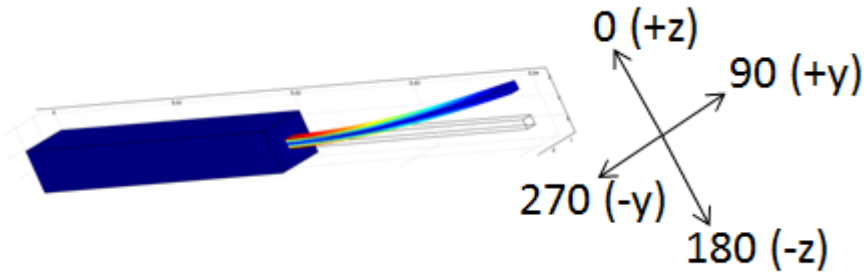

Figure 41: Labeling of Multi-Directional Bending

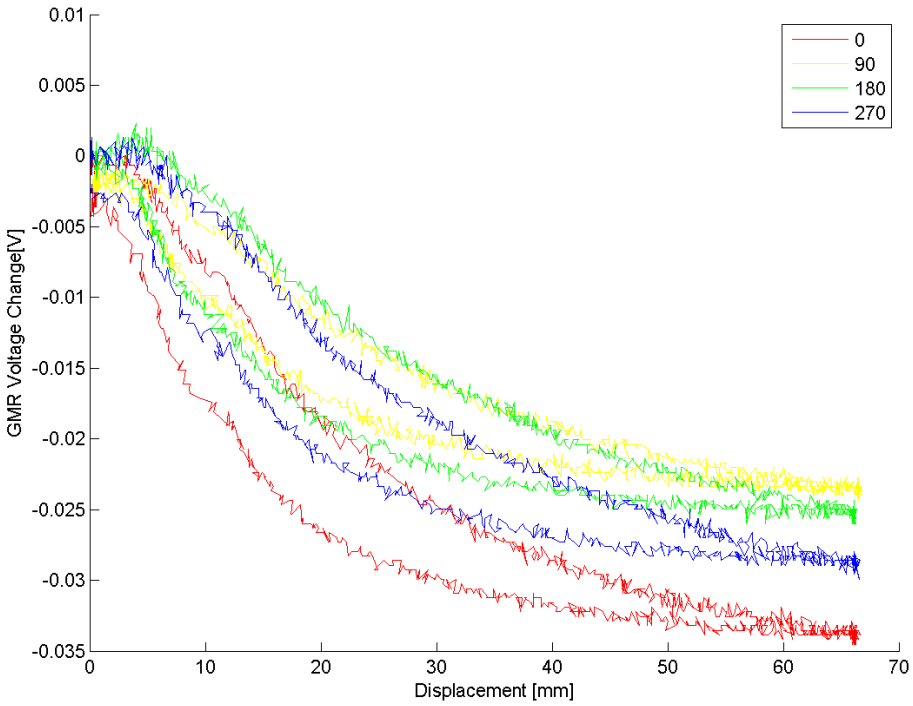

Figure 42: Displacing the whisker tip by equal magnitudes in four perpendicular directions

Static Displacement Behavior

Static displacement tests were conducted on the whisker. The whisker tip was displaced by 10 mm, 30 mm, and 65 mm. The tip was held for approximately 30 seconds before being returned to the neutral position. The GMR voltage change was proportional to the tip displacement. As the whisker tip was returned to the neutral position, the GMR sensor signal returned to the original voltage as well.

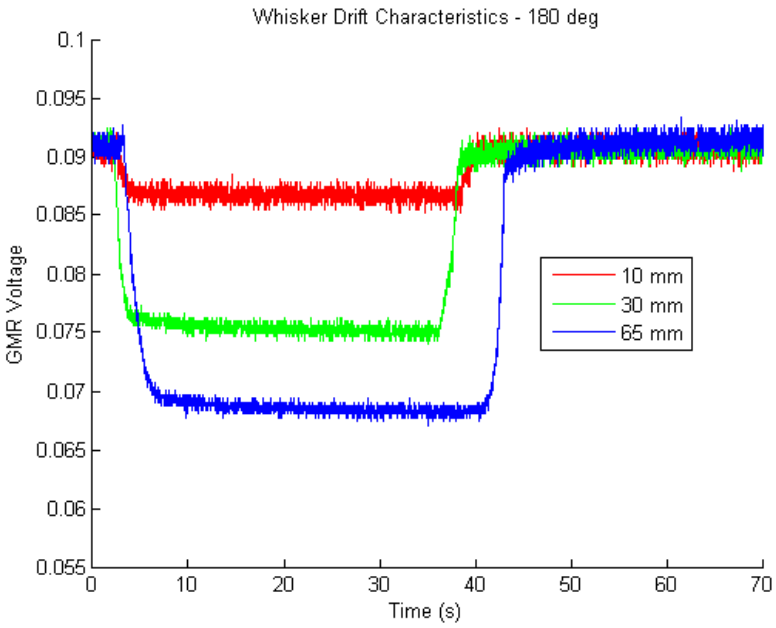

Figure 43: 30-Second Static Displacement - 180 Degrees

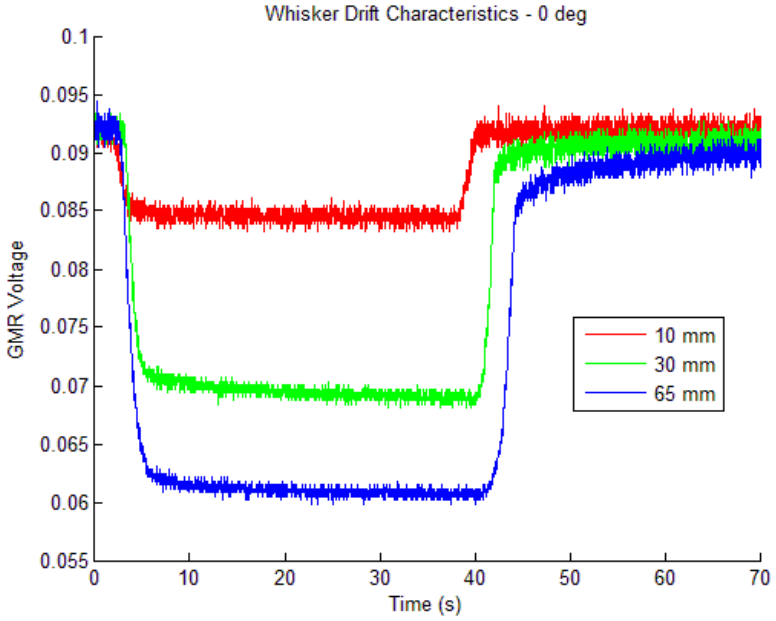

Figure 44: 30-Second Static Displacement - 0 Degrees

Issues that Need to be Addressed

GMR Sensor Saturation

The GMR sensor saturated when the .67 T permanent magnet was moved close to the GMR sensor circuit board. It remains to be seen if greater sensitivity can be achieved with a GMR sensor that saturates at a higher magnetic field.

The NVE AAL002-02 GMR sensor was selected due to its low-hysteresis characteristics. Other GMR sensors should be tried with a broader magnetic field range.

Magnetic Field Interference

While positioning the whisker sensor in preparation for tactile testing, it was observed that rotating the entire whisker sensor prototype caused a change in the GMR circuit's voltage output. While no proper quantitative measurements were taken to study this phenomenon closer, it is assumed that the GMR sensing circuit is sensitive to variations in Earth's magnetic field. Moving permanent magnets within a few inches of the GMR sensor or the whisker also caused fluctuations in the sensor output.

Symmetry

The whisker sensor did not have a symmetrical response to equal displacements in opposite directions. While care was taken in placing the GMR sensor over the whisker before applying epoxy, there was no precise method in doing so. As a result, a small misalignment of the GMR's axis of sensitivity with respect to the whisker may cause some of the asymmetrical behavior in the GMR sensor output.

Other possible causes may include imperfections in the epoxy layer holding the whisker, and imperfections in the Galfenol sample.

Hysteresis

Hysteresis is observed in the GMR sensor signal. A noticeable difference is seen in the upsweep and downsweep. For a given tip displacement, the GMR signal has a lower voltage during the upsweep relative to the GMR signal voltage during the downsweep. The difference between the upsweep voltage and the downsweep voltage is most noticeable for displacements in the 10-30 mm range; this difference can be as high as 10 mV, or 20-30% of the maximum displacement voltage reading.

Drift

During the static displacement tests, a small but noticeable drift is observed at tip displacements of 30 mm and 65 mm, visible in Figure 43 and Figure 44. The drift for these static displacements is on the order of 1-2 mV over 30 seconds.

Uncertainty

There is a large increase in GMR signal noise as the permanent magnet was placed close to the GMR sensor. The source of the noise is unknown. This is apparent in the figures in Appendix H – Effect of Permanent Magnet Placement (.3 Tesla) and Appendix I – Effect of Permanent Magnet Placement (.67 Tesla).

Chapter 5: Testing in Low-Speed Flow

The whisker was tested and evaluated in its performance as a low-speed flow sensor. The whisker was inserted into a water tunnel test section. The fluid flow imparted a drag force on the whisker, causing the whisker to bend. The same LabVIEW data acquisition system mentioned in chapter 4 was used to detect the GMR sensor voltage.

Experimental Setup

Water Tunnel

Water tunnel testing was done at the University of Maryland's Edwin W. Inglis '43 Thermal Fluids Instructional Laboratory. The water tunnel used in flow experiments was designed and manufactured by Engineering Laboratory Design, Inc. The 501/502 model had a 6" x 6" x 18" test section, with flow rates up to 1.0 fps.

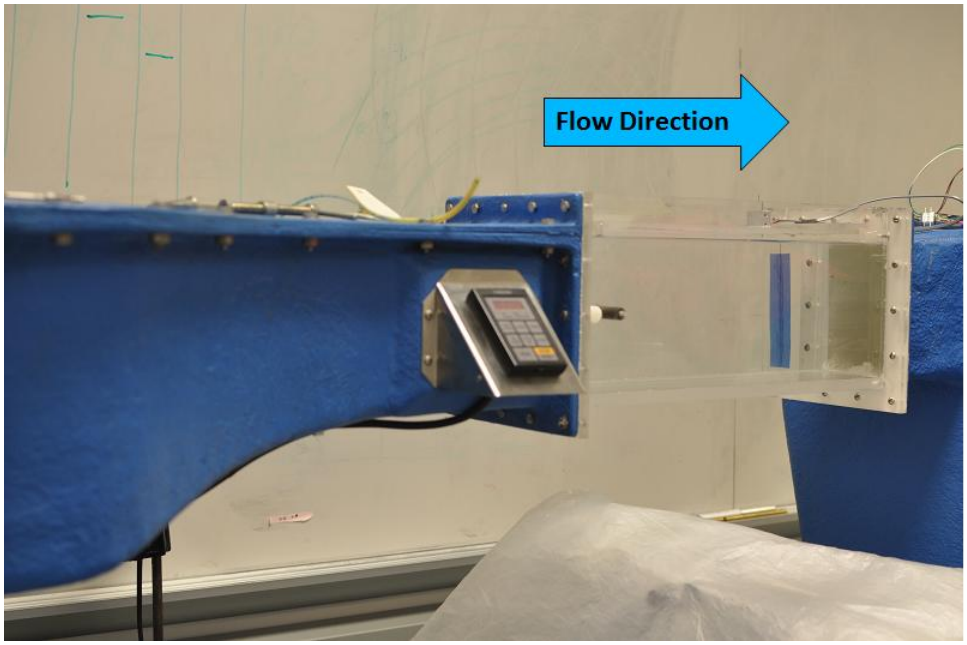

Figure 45: Water Tunnel Flow Direction

Whisker Placement

The whisker sensor was oriented such that the aluminum whisker holder (composed of the epoxy layer, GMR sensor, and permanent magnet) were above the surface of the water, while most of the free end of the whisker was submerged in the water. The neutral position of the whisker was perpendicular to the direction of the water flow.

Drag Element

Initial testing of the whisker was conducted in water flow velocities up to 17 centimeters per second. It was found that for any of the tested flow velocities, there was an insufficient drag force on the whisker to cause it to bend; therefore, there was no magnetization change in the whisker, and no voltage change in the GMR sensor output.

In order to increase the whisker's sensitivity to low speed flows, a 5 cm wide x 13 cm long x .5mm thick plastic element was attached to the whisker to increase the amount of pressure drag that would be imparted by the water flow.

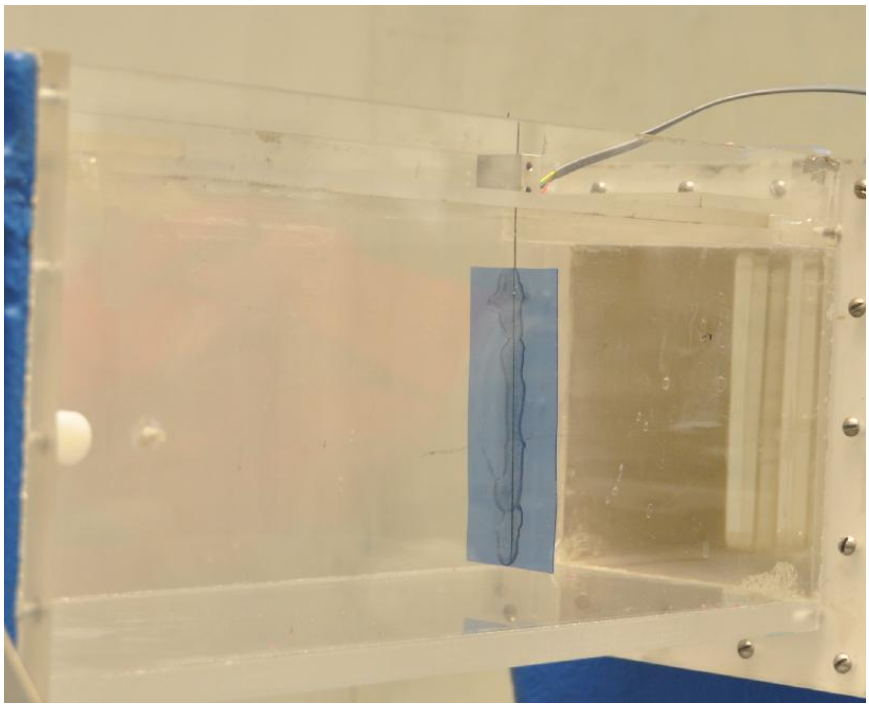

Figure 46: Plastic Drag Element

Results

Flow Velocity Sweeps

The whisker sensor prototype was tested with the pressure drag element attached. The permanent magnet placement was the same as with the tactile tip loading tests. Data was recorded for flow speeds between 0 and 17 cm/s. For each tested flow velocity, data was recorded for 30 seconds. The 'upsweep' consisted of increasing flow velocities, and the 'downsweep' consisted of decreasing flow

velocities. The error bars shown in Figure 47 represent the standard deviation of the sensor noise for 30 seconds of data taken at each flow speed.

Results show a correlation between flow speed and sensor output. Similar to the tactile tip loading tests, hysteresis is observable between the upsweep and downsweep. Due to hysteresis, the sensor has a flow velocity uncertainty of up to 2.5 cm/s. For example, of the GMR average signal reads .062 V, the flow speed could be between 10 cm/s and 15 cm/s, depending on whether the flow speed was on the upsweep or downsweep. Thus, one could conclude that at a voltage of .062 V, the flow speed is 12.5 +/- 2.5 cm/s. The uncertainty decreases at moderate flow speeds around 4 cm/s to 10 cm/s.

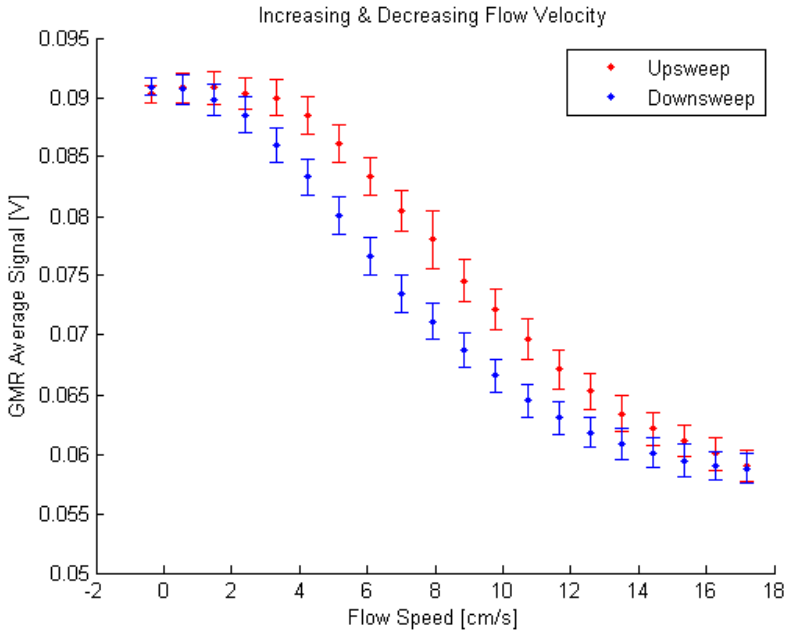

Figure 47: Increasing & Decreasing Flow Velocity

Randomized Flow Velocities

Randomized sampling was done at flow speeds between 0 and 17 cm/s. Three tests were conducted – for each test the flow speeds were randomly ordered. 30 seconds of data were recorded for each flow speed.

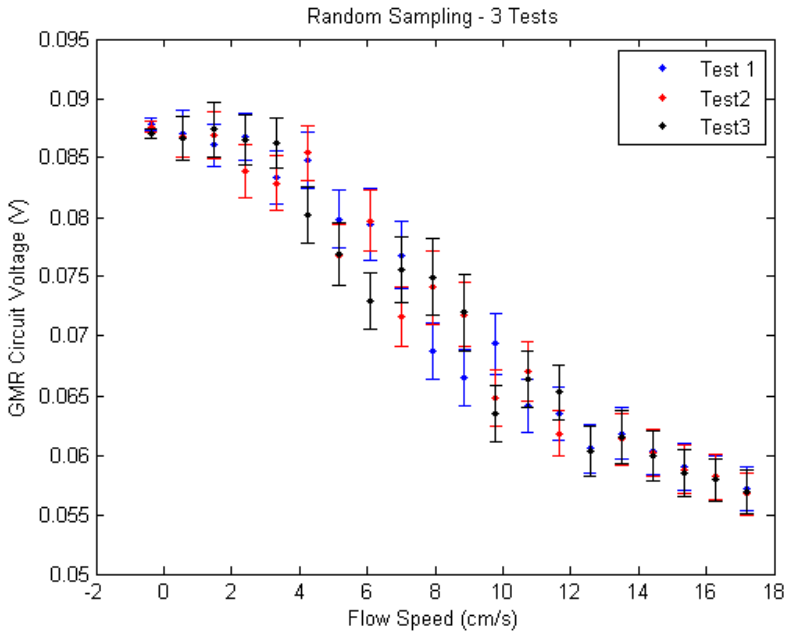

Figure 48: Water Tunnel Random Sampling

Issues that Need to be Addressed

Numerous issues were encountered during flow sensing experiments. The whisker was too stiff for the flow speeds tested. As a result, the fluid flow could not impart enough drag on the whisker for it to bend. The drag flag was used to impart more drag on the whisker. While a trend was realized between the flow speed and the GMR circuit voltage, there was a large amount of uncertainty from unknown causes. Further investigation is warranted. Like with the tactile bending tests, hysteresis was observed, further adding to the uncertainty of the sensor.

Chapter 6: Conclusion

Summary

The prototype presented in this thesis was a proof of concept sensor, showing that it would be possible to create a multipurpose bending sensor based on the magnetostrictive properties of Galfenol. The bidirectionally-coupled magnetoelastic model was used with COMSOL 3.5a. The results predicted that the strength of the biasing magnet and placement of the GMR sensor have an effect on the sensing ability of the whisker. Quasi-static tactile bending tests and low-speed flow tests were done on the whisker. Results show that a magnetic field change is detected as a result of the changing magnetization in a bending Galfenol whisker. However, there are problems such as hysteresis and asymmetry in the sensitivity of bending in different directions. Further refinement of the whisker prototype is required before practical application of the sensor. Based on the results of the prototype sensor tactile bending and flow sensing tests, the following whisker characteristics were observed:

Tactile Bending with .3 Tesla Permanent Magnet @ 2 mm Behind GMR Sensor	Range: 0 to 65 mm tip displacement Uncertainty: +/- 5 mm tip displacement Sensitivity: .51 mV/mm (0° bending direction)
Flow Sensing with .3 Tesla Permanent Magnet @ 2 mm Behind GMR Sensor	Range: 0 to 18 cm/s flow speed Uncertainty: +/- 2.5 cm/s flow speed Sensitivity: 1.74 mV/[cm/s]

Future Work

Sensors function best when they are tailored to a certain application. Future work includes optimizing the whisker sensor to best suit certain applications that

require such a sensor. For example, the biasing magnet can be placed farther away to better suit applications where there are low bending displacements. The whisker itself can be machined to form various geometries that are more responsive to water flow.

Future work should be done to investigate the causes and effects of the hysteresis observed in the sensor. Further investigation should also be done on the fatigue properties of a Galfenol whisker that is bent repeatedly, and the effect of the rusting of Galfenol on its mechanical properties.

More tests should be done to determine the complete mechanical and magnetic characteristics of the Galfenol ($Fe_{81}Ga_{19}$ + 1.0% NbC) rolled sheet with developed Goss texture. Failure modes need to be determined on the whisker.

This thesis research presented an evaluation of the quasi-static bending of the whisker prototype. Dynamic behavior of the whisker should be tested and evaluated. Such research may find new applications for the whisker sensor. The whisker prototype could potentially act as an accelerometer or a vibration sensor.

Appendix A – Visualizing Magnetic Domains During Bending Using MOKE Microscope

Figure 49: MOKE Microscope

Figure 49 shows the magneto-optic Kerr effect (MOKE) microscope used to observe the domain rotations of the whisker.

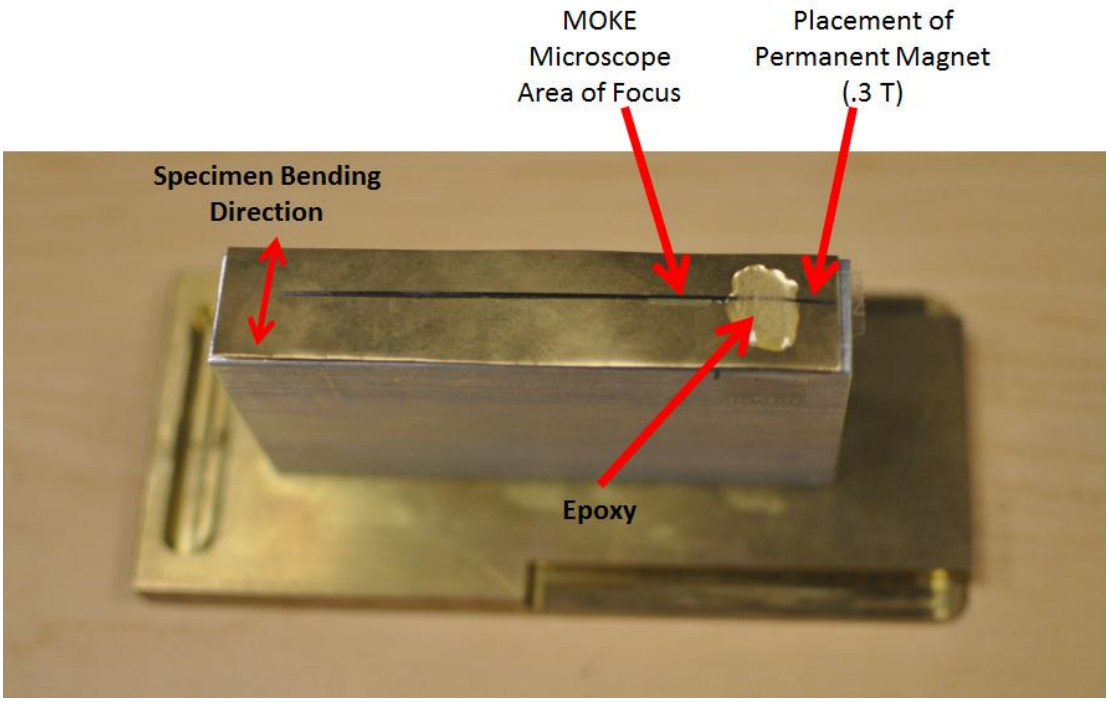

Figure 50: Polished Galfenol Specimen for MOKE Microscope

Figure 50 shows the Galfenol specimen that was observed while bending under the MOKE microscope. The specimen was 7 cm long, with a width and thickness of .6 mm. The specimen was polished using silica gel, resulting in a final thickness of .45 mm.

The Galfenol specimen was secured to an aluminum and brass stage using epoxy. A .3 T permanent magnet was attached to the right of the epoxy. The MOKE microscope lens was focused just to the left of the epoxy during bending. The whisker tip was displaced 2 centimeters both directions from the neutral axis when the images in Figure 9a and Figure 9c were captured.

Appendix B – Characterization of Mechanical Properties

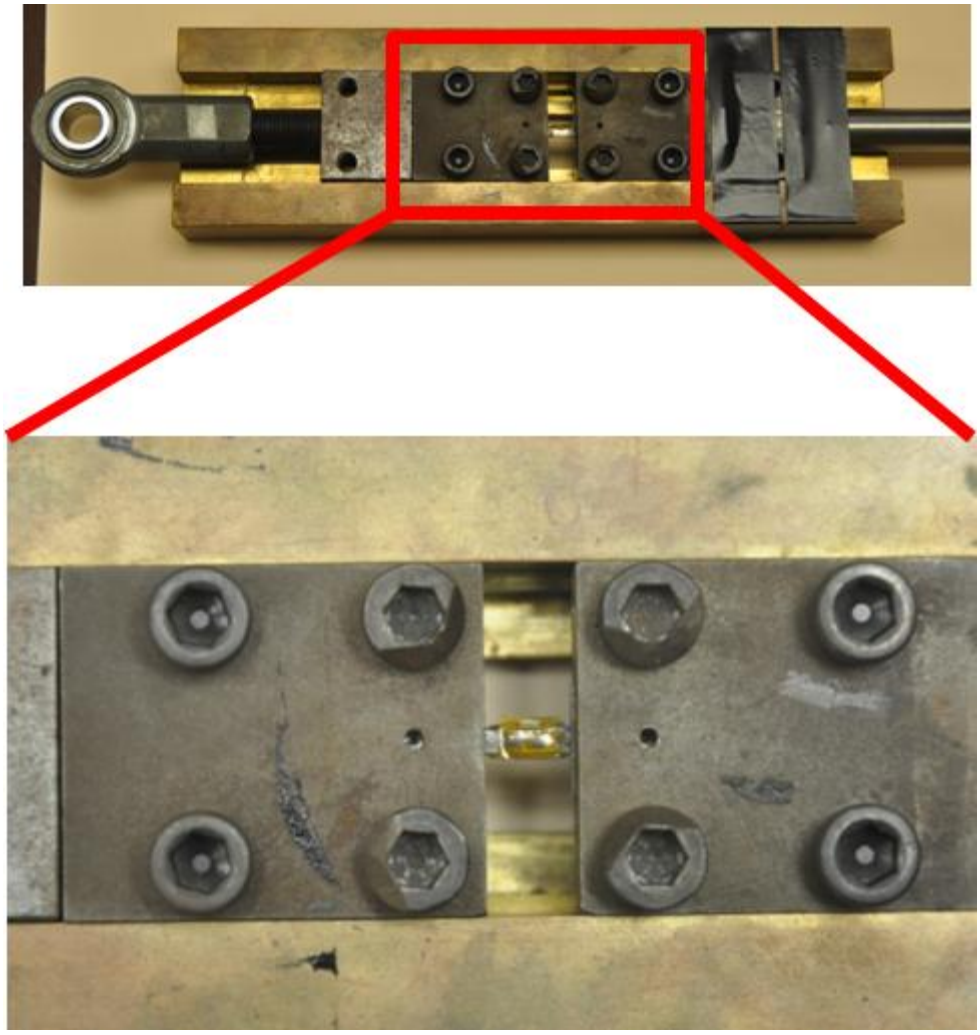

Figure 51: Clamped Galfenol Sample for Tensile Tests

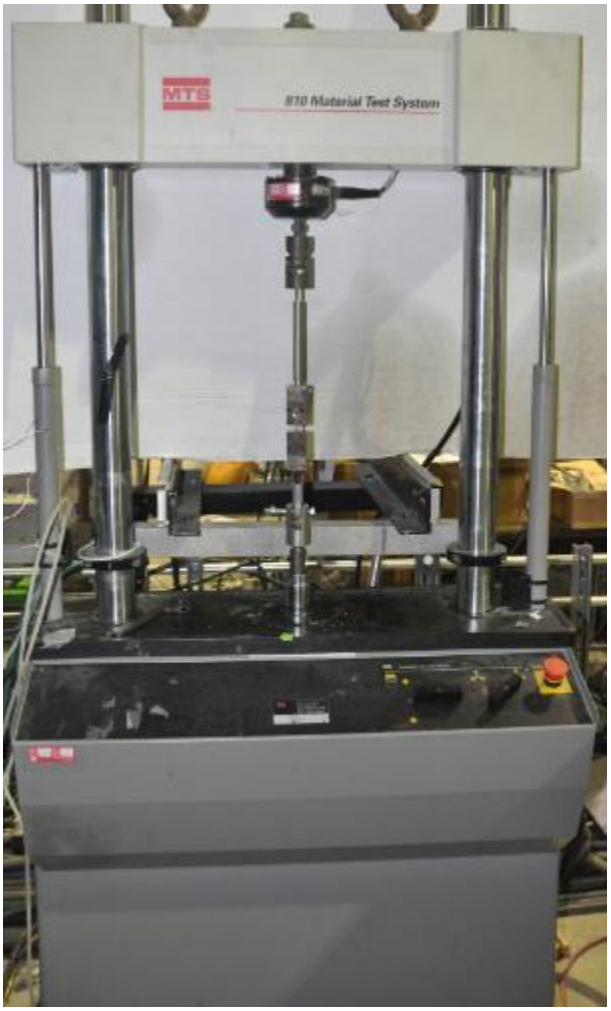

Figure 52: Material Test System for Tensile Tests of Galfenol Dogbone

Appendix C – Creating the COMSOL Geometries

Geometries and boundary conditions for both the mechanical and magnetic problems were first sketched in COMSOL. The geometries and boundary conditions were then exported as MATLAB .m files. The generated code was pasted into the BCMEM code shown in Appendix D – BCMEM Sample Code.

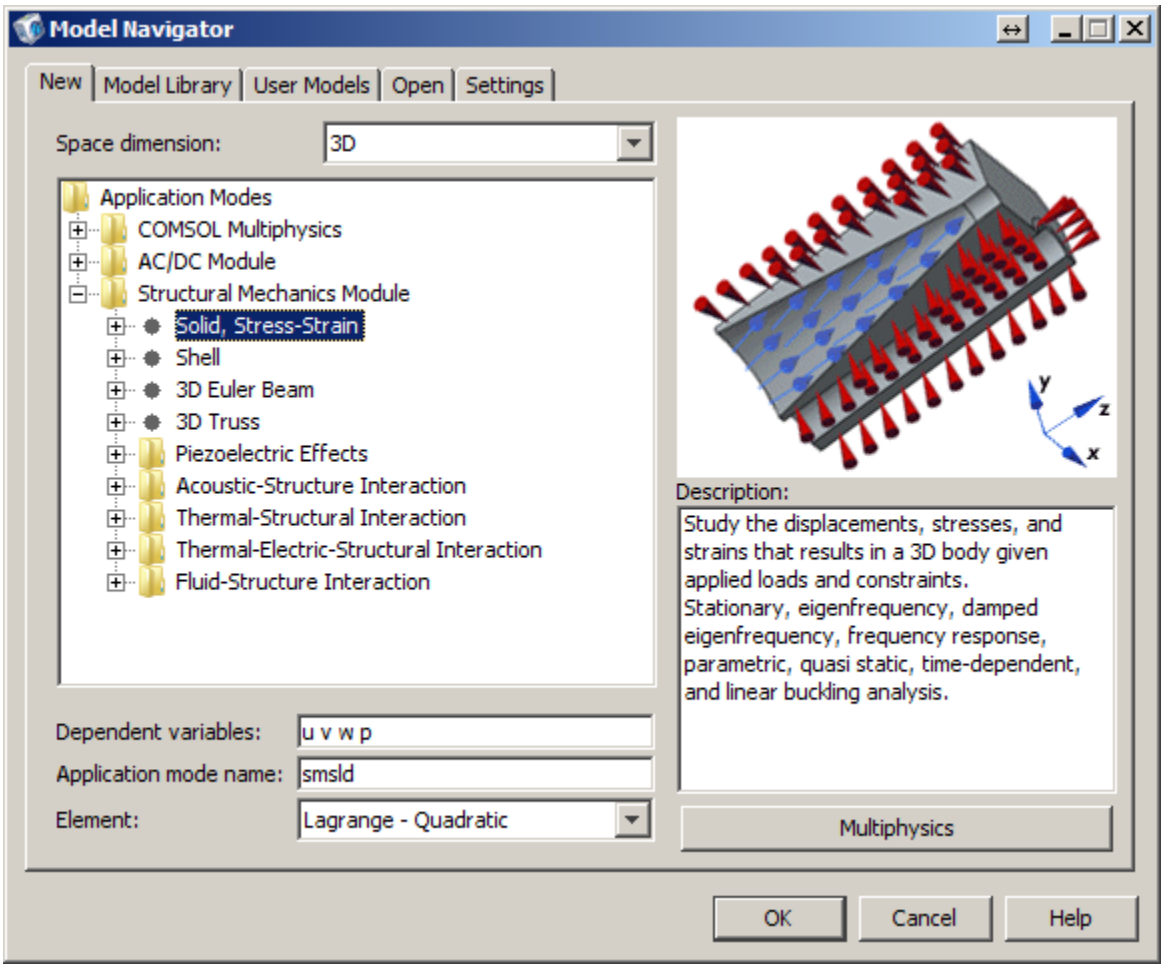

Figure 53: Creating Mechanical Geometry - Application Mode

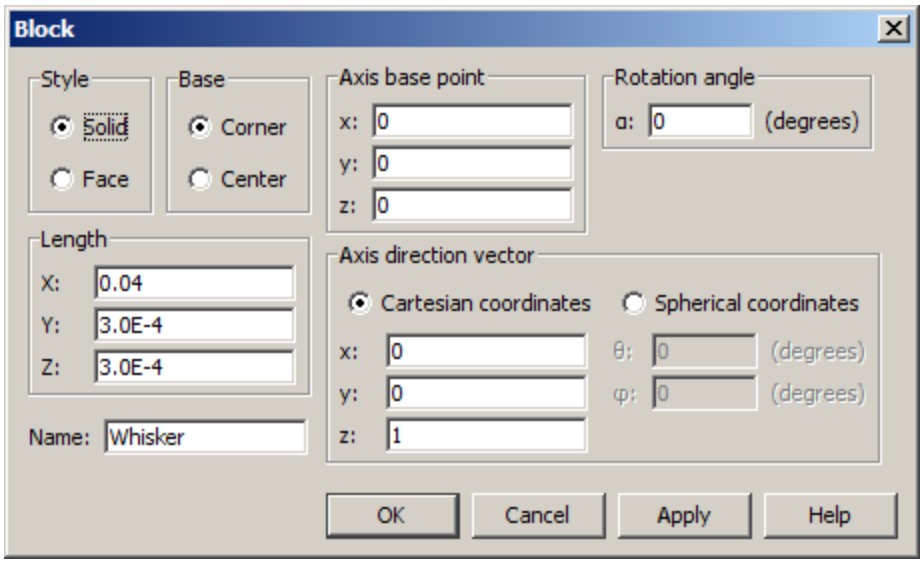

Figure 54: Creating Mechanical Geometry - Sketching Whisker

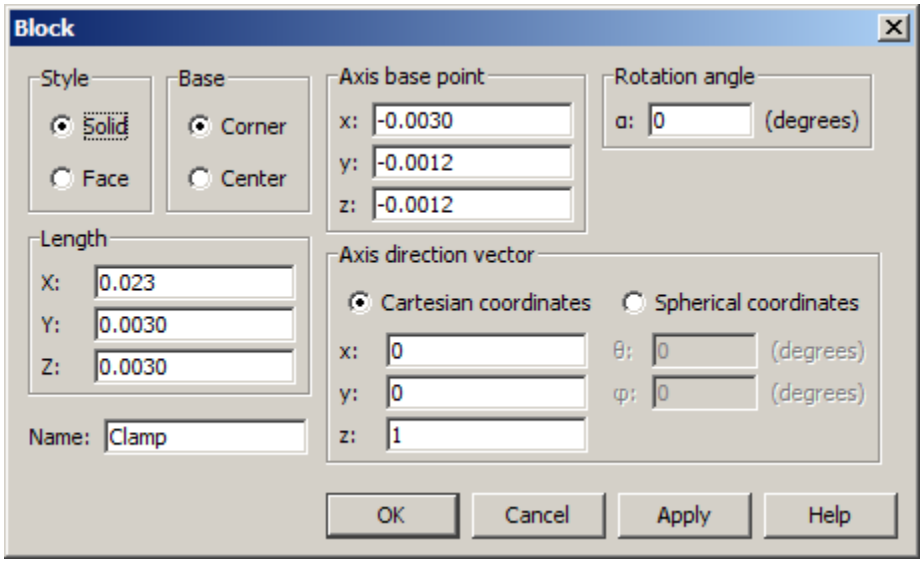

Figure 55: Creating Mechanical Geometry - Sketching Clamp

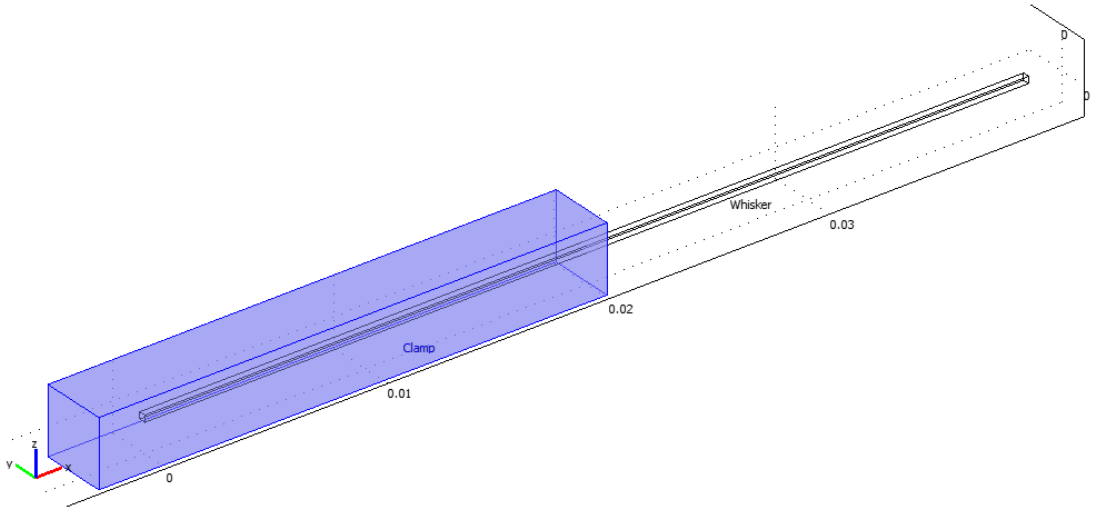

Figure 56: Creating Mechanical Geometry - Isometric View

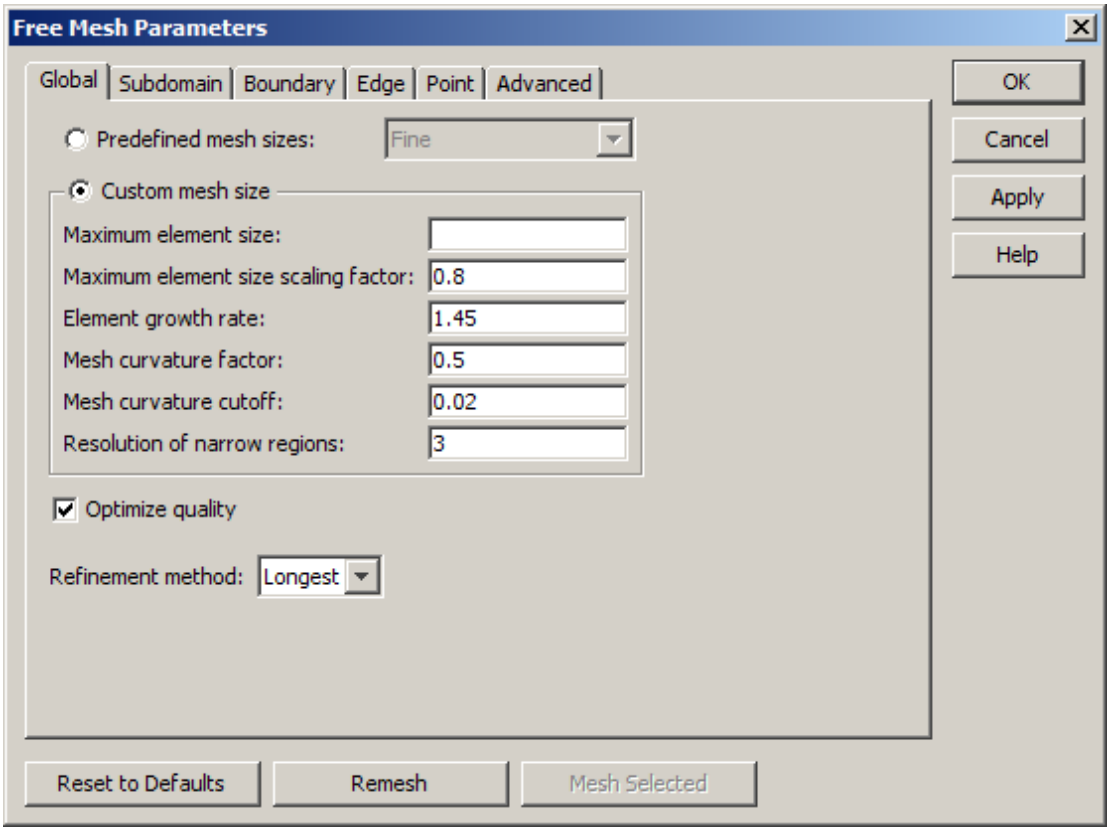

Figure 57: Creating Mechanical Geometry - Free Mesh Parameters

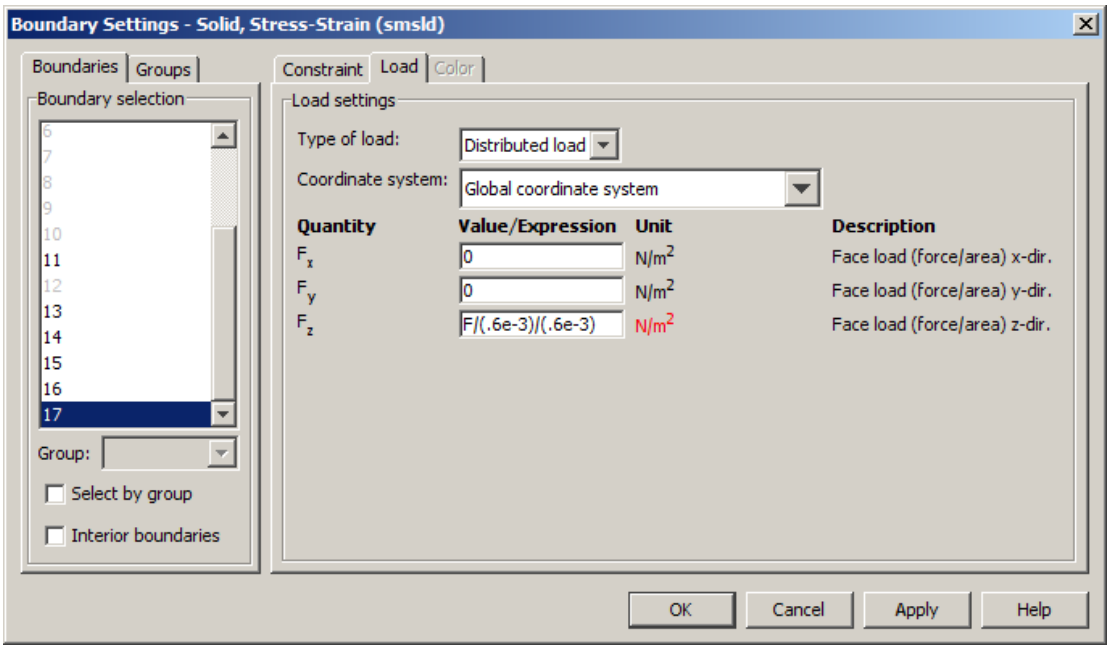

Figure 58: Creating Mechanical Geometry - Setting Tip Force

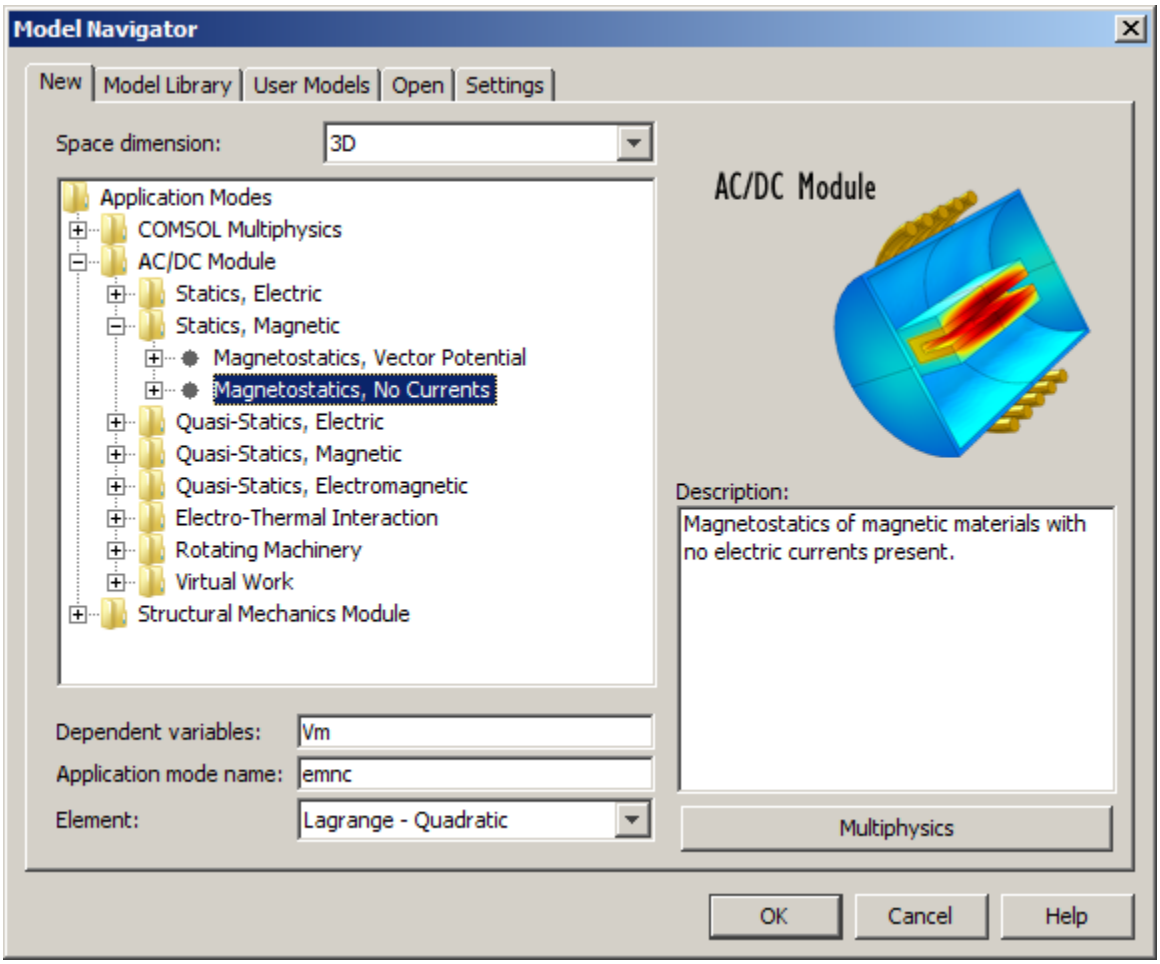

Figure 59: Creating Magnetic Geometry - Application Mode

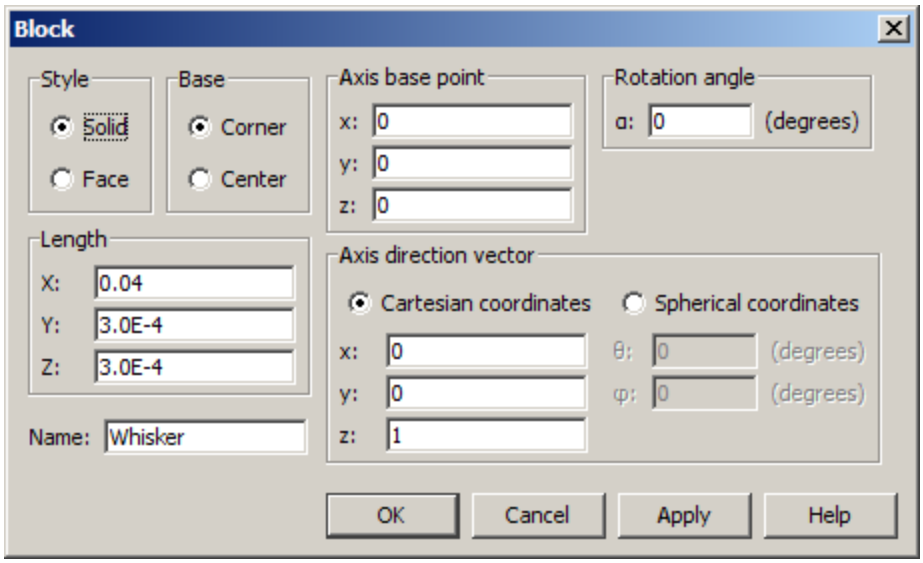

Figure 60: Creating Magnetic Geometry - Sketching Whisker

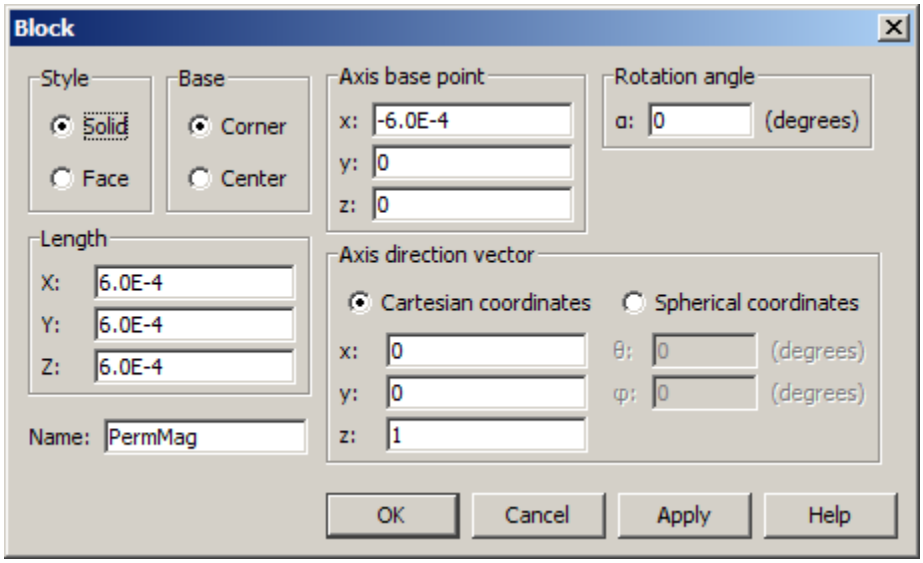

Figure 61: Creating Magnetic Geometry - Sketching Bias Magnet

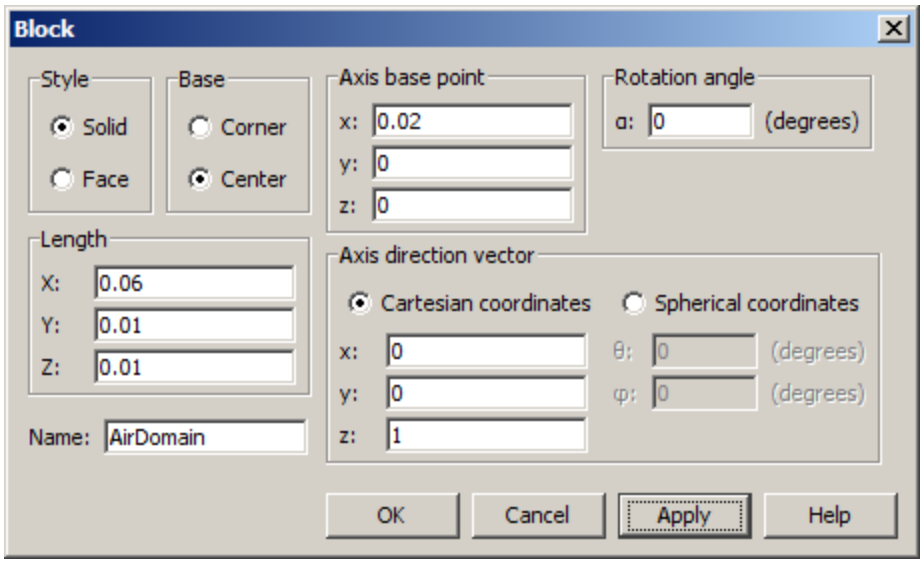

Figure 62: Creating Magnetic Geometry - Sketching Air Domain

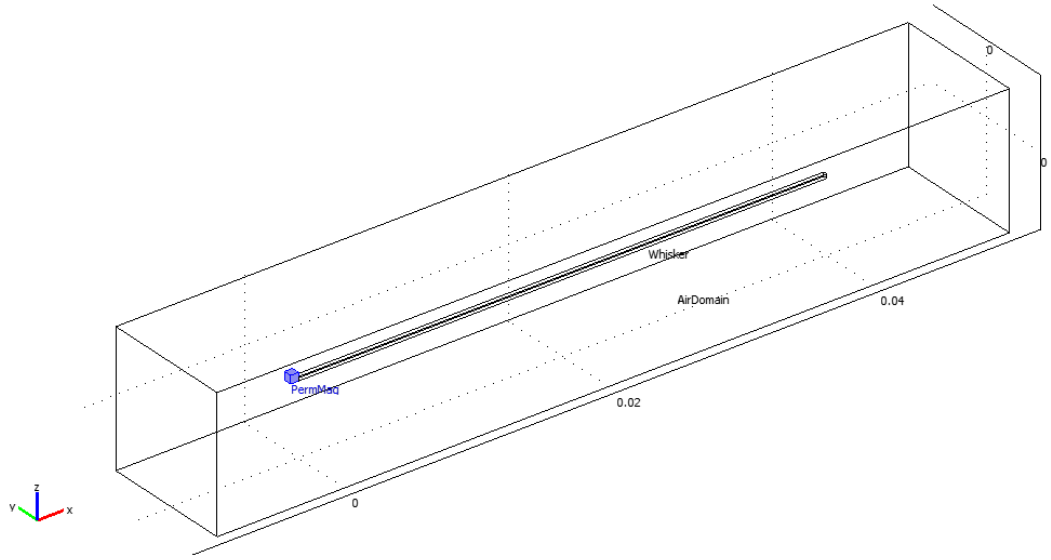

Figure 63: Creating Magnetic Geometry - Isometric View

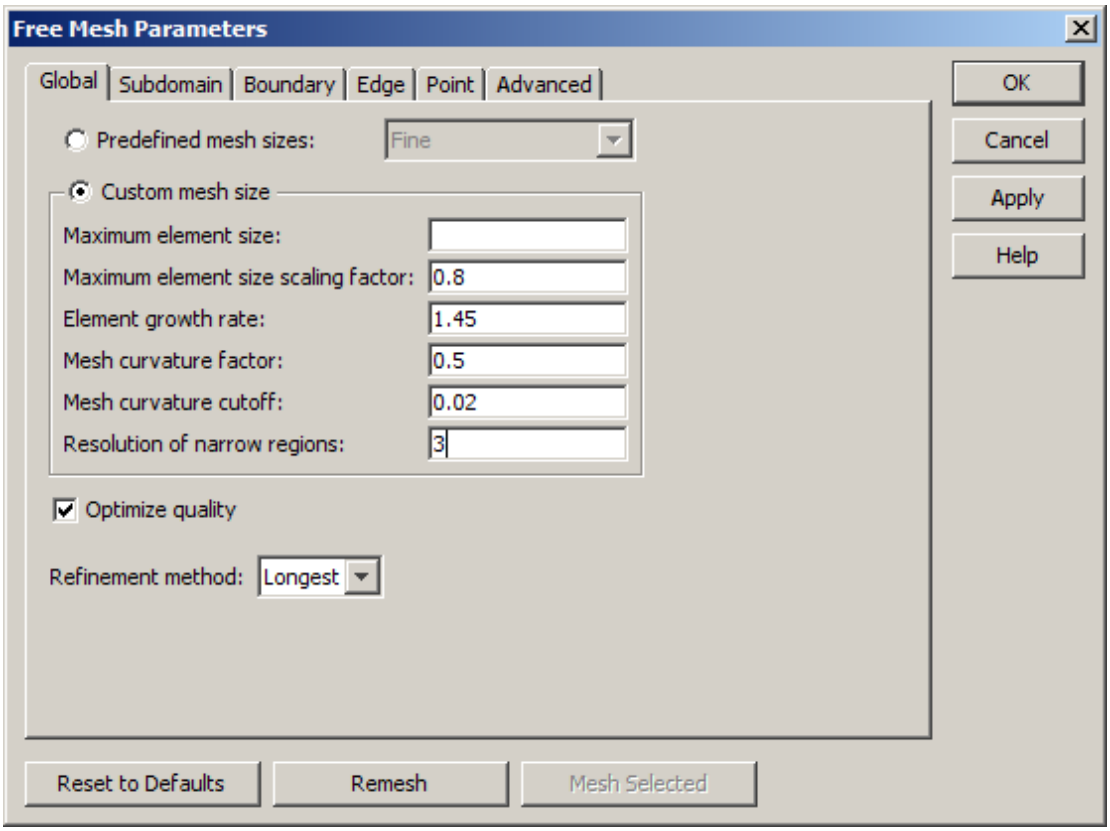

Figure 64: Creating Magnetic Geometry - Free Mesh Parameters

Boundary Conditions:
Edges of air domain: magnetic insulation $\mathbf{n} \cdot \mathbf{B} = 0$
All else: Continuity

Appendix D – BCMEM Sample Code

The BCMEM sample code was run from the MATLAB command line, after opening 'COMSOL 3.5a with MATLAB'

```
clc; close all; clear all;

% Model for full coupling of .6 mm x .6 mm x 4 cm Galfenol Whisker
tps = clock; % time at process start
global fem_mech fem_mag femmech femmag domain_mech domain_mag X Y Z
test1 test2
% ------------------------------------------------------------------
% Mechanical problem
% ------------------------------------------------------------------
flclear fem fem_mech fem_mag

% Geometry
g1=block3('.04','.6e-3','.6e-
3','base','corner','pos',{'0','0','0'},'axis',...
    {'0','0','1'},'rot','0');
g2=block3('0.023','0.0030','0.0030','base','corner','pos',...
    {'-.003','-0.0015+.6e-3/2','-0.0015+.6e-
3/2'},'axis',{'0','0','1'},'rot','0');

% Analyzed geometry
clear s
s.objs={g1,g2};
s.name={'Whisker','Epoxy'};
s.tags={'g1','g2'};

fem.draw=struct('s',s);
fem.geom=geomcsg(fem);

% Initialize mesh
fem.mesh=meshinit(fem, ...
                  'hmaxfact',0.8, ...
                  'hcurve',0.5, ...
                  'hgrad',1.45, ...
                  'hcutoff',0.02, ...
                  'hnarrow',3);

% Constants
fem.const = {'iter','0', ...
  'F','0', ...
  'E','56e9'};

% Application mode 1
clear appl
appl.mode.class = 'SmeSolid3';
appl.module = 'SME';
appl.gporder = 4;
appl.cporder = 2;
```

```
appl.sshape = 2;
appl.assignsuffix = '_smsld';
clear bnd
bnd.Fz = {0,0,'F/(.6e-3)/(.6e-3)'};
bnd.constrcond = {'free','fixed','free'};
bnd.ind = [2,2,2,2,2,1,1,1,1,1,1,1,1,1,1,1,3];
appl.bnd = bnd;
clear equ
equ.nu = {0.45,.45};
equ.rho = {7850,7850};
equ.E = {56e9,'Emod(ex_smsld)'};
equ.name = {'Epoxy','Whisker'};
equ.ind = [1,2,2];
appl.equ = equ;
fem.appl{1} = appl;
fem.frame = {'ref'};
fem.border = 1;
clear units;
units.basesystem = 'SI';
fem.units = units;

% Subdomain settings
clear equ
equ.ind = [1,2,2];
equ.dim = {'u','v','w','p'};

% Subdomain expressions
equ.expr = {'lamda',{'',0}};
fem.equ = equ;

% ODE Settings
clear ode
clear units;
units.basesystem = 'SI';
ode.units = units;
fem.ode=ode;

% Multiphysics
fem=multiphysics(fem);
fem.xmesh=meshextend(fem);

fem_mech = fem;
%-------------------------------------------------
% Magnetic problem
%-------------------------------------------------
flclear fem

% Geometry
g1=block3('.04','.6e-3','.6e-
3','base','corner','pos',{'0','0','0'},...
    'axis',{'0','0','1'},'rot','0');
g2=block3('.6e-3','.6e-3','.6e-3','base','corner','pos',{'-.6e-
3','0','0'},...
    'axis',{'0','0','1'},'rot','0');
g3=block3('8e-2','2e-2','2e-
2','base','center','pos',{'0','0','0'},'axis',...
```

```
    {'0','0','1'},'rot','0');
g4=block3('0.06','0.01','0.01','base','center','pos',{'2e-
2','0','0'},'axis',...
    {'0','0','1'},'rot','0');

% Analyzed geometry
clear s
s.objs={g1,g2,g4};
s.name={'Whisker','PermMag','AirDomain'};
s.tags={'g1','g2','g4'};

fem.draw=struct('s',s);
fem.geom=geomcsg(fem);

% Initialize mesh
fem.mesh=meshinit(fem, ...
                  'hmaxfact',0.8, ...
                  'hcurve',0.5, ...
                  'hgrad',1.45, ...
                  'hcutoff',0.02, ...
                  'hnarrow',3);

% Constants
fem.const = {'mue11','1200', ...
  'mue22','mue11', ...
  'mue33','(2/3)*mue11', ...
  'soln','0', ...
  'iter','0'};

% Application mode 1
clear appl
appl.mode.class = 'MagnetostaticsNoCurrents';
appl.module = 'ACDC';
appl.sshape = 2;
appl.border = 'on';
appl.assignsuffix = '_emnc';
clear bnd
bnd.type = {'nB0','cont'};
bnd.ind = [1,1,1,1,1,2,2,2,2,2,2,2,2,2,2,2,1];
appl.bnd = bnd;
clear equ
equ.magconstrel = {'mur','Br','mur'};
equ.name = {'Air','Magnet','Whisker'};
equ.mur =
{1,1,{'muinterp(Hx_emnc,x,y,z,soln,iter)';'mue22';'mue33'}};
equ.Br = {{0;0;0},{.25;0;0},{0;0;0}};
equ.ind = [1,2,3];
appl.equ = equ;
fem.appl{1} = appl;
fem.frame = {'ref'};
fem.border = 1;
clear units;
units.basesystem = 'SI';
fem.units = units;

% ODE Settings
```

```
clear ode
clear units;
units.basesystem = 'SI';
ode.units = units;
fem.ode=ode;

% Multiphysics
fem=multiphysics(fem);

fem.xmesh = meshextend(fem);

fem_mag = fem;

%------------------------------------------------------------
% Problem Solution
%------------------------------------------------------------

domain_mag = 3;
domain_mech = 2;
iter = 1;

Flist=[-.05 -.02 -.01 -.002 -.0005 .002 .01  .02 .05]
N = length(Flist);

fprintf('Solving mechanical problem at zero applied magnetic
field\n');

% Mechanical problem ar zero applied magnetic field
fem_mech.equ.expr{2} = {'0'}; %Zero Field
fem_mech.const{2} = iter;
fem_mech = multiphysics(fem_mech);

% modifying the standard elastic constitutive relations to take the
magnetostriction into account
sigmax = 'E_smsld*(1-nu_smsld)*ex_smsld/((1+nu_smsld)*(1-
2*nu_smsld))+E_smsld*nu_smsld*ey_smsld/((1+nu_smsld)*(1-
2*nu_smsld))+E_smsld*nu_smsld*ez_smsld/((1+nu_smsld)*(1-
2*nu_smsld))';
sigmax_mod = 'E_smsld*(1-nu_smsld)*(ex_smsld-
lamda)/((1+nu_smsld)*(1-
2*nu_smsld))+E_smsld*nu_smsld*ey_smsld/((1+nu_smsld)*(1-
2*nu_smsld))+E_smsld*nu_smsld*ez_smsld/((1+nu_smsld)*(1-
2*nu_smsld))';
sigmay = 'E_smsld*nu_smsld*ex_smsld/((1+nu_smsld)*(1-
2*nu_smsld))+E_smsld*(1-nu_smsld)*ey_smsld/((1+nu_smsld)*(1-
2*nu_smsld))+E_smsld*nu_smsld*ez_smsld/((1+nu_smsld)*(1-
2*nu_smsld))';
sigmay_mod = 'E_smsld*nu_smsld*(ex_smsld-lamda)/((1+nu_smsld)*(1-
2*nu_smsld))+E_smsld*(1-nu_smsld)*ey_smsld/((1+nu_smsld)*(1-
2*nu_smsld))+E_smsld*nu_smsld*ez_smsld/((1+nu_smsld)*(1-
2*nu_smsld))';
sigmaz = 'E_smsld*nu_smsld*ex_smsld/((1+nu_smsld)*(1-
2*nu_smsld))+E_smsld*nu_smsld*ey_smsld/((1+nu_smsld)*(1-
2*nu_smsld))+E_smsld*(1-nu_smsld)*ez_smsld/((1+nu_smsld)*(1-
2*nu_smsld))';
```

```
sigmaz_mod = 'E_smsld*nu_smsld*(ex_smsld-lamda)/((1+nu_smsld)*(1-
2*nu_smsld))+E_smsld*nu_smsld*ey_smsld/((1+nu_smsld)*(1-
2*nu_smsld))+E_smsld*(1-nu_smsld)*ez_smsld/((1+nu_smsld)*(1-
2*nu_smsld))';

fem_mech.equ.var{22} = {sigmax sigmax_mod};
fem_mech.equ.var{24} = {sigmay sigmay_mod};
fem_mech.equ.var{26} = {sigmaz sigmaz_mod};
fem_mech.xmesh = meshextend(fem_mech);
femmech{iter} = fem_mech;

% Nonlinear solver
femmech{iter}.sol = femstatic(fem_mech, ...
                  'matherr','off', ...
                  'symmetric','on', ...
                  'solcomp',{'u','v','w'}, ...
                  'outcomp',{'u','v','w'}, ...
                  'pname','F', ...
                  'plist',Flist,'nonlin','on');

while(iter~=4)
tis = tic; % time at iteration start

disp('iter')
disp(iter)
fem_mag.appl{1}.equ.mur{3}{1,1} =
'muinterp(Hx_emnc,x,y,z,soln,iter)';
fem_mag.const{10} = iter;
fem_mag = multiphysics(fem_mag);
fem_mag.xmesh = meshextend(fem_mag);
femmag{iter} = fem_mag;
fprintf('Solving magnetic problem using nonlinear solver for an
applied stress calculated from the mechanical problem previously
solved\n');
% Magnetic problem for an applied stress solved using the stress
calculated from the mechanical problem (nonlinear solver)
femmag{iter}.sol=femstatic(fem_mag, ...
                  'symmetric','on', ...
                  'solcomp',{'Vm'}, ...
                  'outcomp',{'Vm'}, ...
                  'pname','soln', ...
                  'plist',[1:N],'nonlin','on','ntol',1.0E-4);

% Solution at zero applied stress

fprintf('End of iteration %i\n',iter);
fname_mech = sprintf('femmech_iter%i',iter);
fem = femmech{iter};
flsave(fname_mech,fem);
fname_mag = sprintf('femmag_iter%i',iter);
clear fem;
fem = femmag{iter};
flsave(fname_mag,fem);

tie = toc(tis); % elapsed time since the start of the iteration
```

```
fprintf('iteration %i took %g minutes to complete\n',iter,tie/60);

iter = iter+1;

fem_mech.equ.expr{2} = {'lambdaHinterp(x,y,z,F,iter)'};
fem_mech.const{2} = iter;
fem_mech.appl{1}.equ.E{2} = 'Emod(ex_smsld)';
fem_mech = multiphysics(fem_mech);
fem_mech.equ.var{22} = {sigmax sigmax_mod};
fem_mech.equ.var{24} = {sigmay sigmay_mod};
fem_mech.equ.var{26} = {sigmaz sigmaz_mod};
fem_mech.xmesh = meshextend(fem_mech);

femmech{iter} = fem_mech;
fprintf('Solving mechanical problem for an applied lambda
(magnetostriction) calculated from the previously solved magnetic
problem\n');
% Iteration using previously calculated magnetic solution
femmech{iter}.sol = femstatic(fem_mech, ...
                  'symmetric','on', ...
                  'solcomp',{'w','v','u'}, ...
                  'outcomp',{'w','v','u'}, ...
                  'pname','F', ...
                  'plist',Flist,'nonlin','on');
end

fname_mech = sprintf('femmech_iter%i',iter);
fem = femmech{iter};
flsave(fname_mech,fem);

tpe = etime(clock,tps); % elapsed time during the process
fprintf('Total process took %g minutes to complete\n',tpe/60);
```

Appendix E – armstrong_optimized.m

The armstrong_optimized.m script was run prior to running the BCMEM code. The input and output arrays were saved in order for the BCMEM to interpolate between the calculated values.

```
function [B MEStrain]  = armstrong_optimized(Hin, Sigmain)
%%%%%%%%%%%%%%%%%%%%%%%%%%%%%%%%%%%%%%%%%%%%%%%%%%%%%%%%%%%%%%%%%%%%%%%%%%%%
%%
%   Input for the function:
%   Hin and Sigmain must be full 3-D vector/tensor in the form
%   Hin = [Hx Hy Hz]';
%   Sigmain = [Sxx Syy Szz Sxy Syz Sxz]';
%
%   Output from the function:
%   B and magnetostriction in full 3-D form
%   B = [Bx By Bz]';
%   MEStrain = [lxx lyy lzz lxy lyz lxz]';
%%%%%%%%%%%%%%%%%%%%%%%%%%%%%%%%%%%%%%%%%%%%%%%%%%%%%%%%%%%%%%%%%%%%%%%%%%%%
%



%% Global Variables
global mu_0 c11 c12 c44 K1 K2 B1 B2 Msat MagElas_FCT

%% Constants
% Fundamental
mu_0 = 4*pi*1e-7; % permeability of free space

%Elastic
c11 = 213e9;
c12 = 174e9;
c44 = 120e9;

% Magnetostrictive(MAGNETOELASTIC)
lambda_100 = 2/3*(247e-6); % strain (-2/3*B1/(c11-c12))
lambda_111 = -2/3*(20e-6); % strain (-1/3*B2/(c44))
MagElas_FCT = 0.875; % from experimental data
B1 = -3/2*lambda_100*(c11-c12);
B2 = -3*lambda_111*c44;


% Magnetocrystalline
K1 = 13e3; % J/m^3 This is actually K1+dK1 or experimentally
measured K1
K2 = -90e3; % J/m^3

% Saturation magnetization
Msat= 1456e3; % in A/m; number from (B - mu_0*H) from experimental
data
```

```
%% VARIABLES

omega = 600; % smoothing function to match with experimental BH plot

%% Angle step size
del_theta = 5; % azimuthal resolution in deg
del_phi = 5; % circular resolution in deg


%% main calculation

% Calculation of principal stresses and their directions
Sigma_tensor = [Sigmain(1) Sigmain(4) Sigmain(6);
                Sigmain(4) Sigmain(2) Sigmain(5);
                Sigmain(6) Sigmain(5) Sigmain(3)];
[pSdirec, pS] = eig(Sigma_tensor); % pS - principal stresses,
pSdirec - principal stress directions

% Meshgrid of theta and phi
[theta, phi] = meshgrid((0:del_theta:180)*pi/180,
(0:del_phi:359)*pi/180);

% Calculate ALPHA's (direction cosines) from theta and phi
ALPHA1 = sin(theta).*cos(phi);
ALPHA2 = sin(theta).*sin(phi);
ALPHA3 = cos(theta);

% Calculation of energy. It now (Nov. 10th 2008) uses stress induced
anisotropy
Etot = Etot2(ALPHA1,ALPHA2,ALPHA3,Hin,pS,pSdirec);

% Calculation of lambda
lambdaxx = B1/(c12-c11)*(ALPHA1.^2-1/3);
lambdayy = B1/(c12-c11)*(ALPHA2.^2-1/3);
lambdazz = B1/(c12-c11)*(ALPHA3.^2-1/3);
lambdaxy = -B2/c44*ALPHA1.*ALPHA2;
lambdayz = -B2/c44*ALPHA2.*ALPHA3;
lambdaxz = -B2/c44*ALPHA3.*ALPHA1;
% Calculation of Magnetization probability
expEtot_dalpha = (del_theta.*del_phi.*abs(sin(theta))).*exp(-
Etot/omega);
dMxProb = (Msat*ALPHA1).*expEtot_dalpha;
dMyProb = (Msat*ALPHA2).*expEtot_dalpha;
dMzProb = (Msat*ALPHA3).*expEtot_dalpha;
% Calculation of Lambda probability
dLambdaxxProb = (lambdaxx).*expEtot_dalpha;
dLambdayyProb = (lambdayy).*expEtot_dalpha;
dLambdazzProb = (lambdazz).*expEtot_dalpha;
dLambdaxyProb = (lambdaxy).*expEtot_dalpha;
dLambdayzProb = (lambdayz).*expEtot_dalpha;
dLambdaxzProb = (lambdaxz).*expEtot_dalpha;
dProb = expEtot_dalpha;

% Calculation of Magnetization
```

```
M = [sum(sum(dMxProb))/sum(sum(dProb));
     sum(sum(dMyProb))/sum(sum(dProb));
     sum(sum(dMzProb))/sum(sum(dProb))];
% Calculation of Magnetostriction
MEStrain = [sum(sum(dLambdaxxProb))/sum(sum(dProb));
            sum(sum(dLambdayyProb))/sum(sum(dProb));
            sum(sum(dLambdazzProb))/sum(sum(dProb));
            sum(sum(dLambdaxyProb))/sum(sum(dProb));
            sum(sum(dLambdayzProb))/sum(sum(dProb));
            sum(sum(dLambdaxzProb))/sum(sum(dProb))];

B = mu_0*(M + Hin); %induction in Tesla


function Etot = Etot2(ALPHA1,ALPHA2,ALPHA3,H,pS,pSdirec)

Etot = Eanisotropy(ALPHA1,ALPHA2,ALPHA3) +
Esaniso(ALPHA1,ALPHA2,ALPHA3,pS,pSdirec) +
Wmagnetic(ALPHA1,ALPHA2,ALPHA3,H);


function Ean = Eanisotropy(APLHA1,APLHA2,APLHA3)
global K1 K2

Ean =
K1*((APLHA1.^2).*(APLHA2.^2)+(APLHA2.^2).*(APLHA3.^2)+(APLHA3.^2).*(
APLHA1.^2)) + K2*((APLHA1.^2).*(APLHA2.^2).*(APLHA3.^2));


function Esan = Esaniso(ALPHA1,ALPHA2,ALPHA3,pS,pSdirec)
global B1 B2 c11 c12 c44 MagElas_FCT;

% first principal stress
direc1 = pSdirec(:,1);
BETA1S = direc1(1)/sqrt(sum(direc1.^2));
BETA2S = direc1(2)/sqrt(sum(direc1.^2));
BETA3S = direc1(3)/sqrt(sum(direc1.^2));
Sigma = pS(1,1);
E11 = B1/(c11-
c12)*Sigma*((ALPHA1.^2)*(BETA1S^2)+(ALPHA2.^2)*(BETA2S^2)+(ALPHA3.^2
)*(BETA3S^2)-1/3);
E21 = B2/c44*Sigma*(ALPHA1.*ALPHA2*BETA1S*BETA2S +
ALPHA2.*ALPHA3*BETA2S*BETA3S + ALPHA3.*ALPHA1*BETA3S*BETA1S);

% second principal stress
direc1 = pSdirec(:,2);
Sigma = pS(2,2);
BETA1S = direc1(1)/sqrt(sum(direc1.^2));
BETA2S = direc1(2)/sqrt(sum(direc1.^2));
BETA3S = direc1(3)/sqrt(sum(direc1.^2));
E12 = B1/(c11-
c12)*Sigma*((ALPHA1.^2)*(BETA1S^2)+(ALPHA2.^2)*(BETA2S^2)+(ALPHA3.^2
)*(BETA3S^2)-1/3);
```

```
E22 = B2/c44*Sigma*(ALPHA1.*ALPHA2*BETA1S*BETA2S +
ALPHA2.*ALPHA3*BETA2S*BETA3S + ALPHA3.*ALPHA1*BETA3S*BETA1S);

% third principal stress
direc1 = pSdirec(:,3);
Sigma = pS(3,3);
BETA1S = direc1(1)/sqrt(sum(direc1.^2));
BETA2S = direc1(2)/sqrt(sum(direc1.^2));
BETA3S = direc1(3)/sqrt(sum(direc1.^2));
E13 = B1/(c11-
c12)*Sigma*((ALPHA1.^2)*(BETA1S^2)+(ALPHA2.^2)*(BETA2S^2)+(ALPHA3.^2
)*(BETA3S^2)-1/3);
E23 = B2/c44*Sigma*(ALPHA1.*ALPHA2*BETA1S*BETA2S +
ALPHA2.*ALPHA3*BETA2S*BETA3S + ALPHA3.*ALPHA1*BETA3S*BETA1S);

Esan = MagElas_FCT*(E11+E21+E12+E22+E13+E23);



function Wmg = Wmagnetic(ALPHA1,ALPHA2,ALPHA3,H)
global mu_0 Msat

Wmg = -mu_0*Msat*(ALPHA1*H(1)+ALPHA2*H(2)+ALPHA3*H(3));
```

Appendix F – COMSOL Results of .75 T Bias Magnet

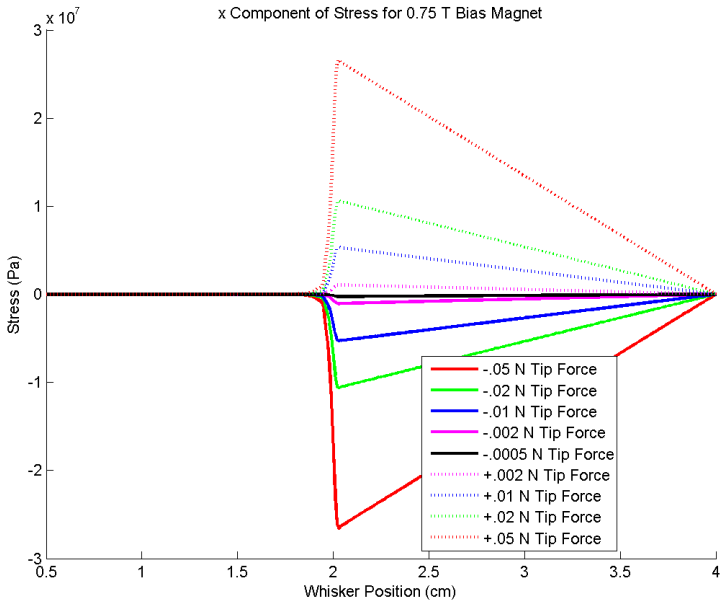

Figure 65: x-Component of Stress for .75 Bias Magnet - Bottom of Whisker

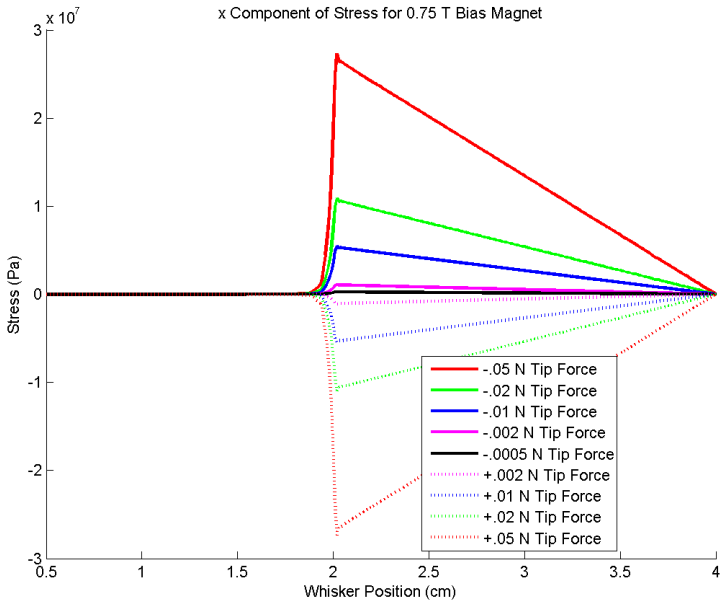

Figure 66: x-Component of Stress for .75 T Bias Magnet - Top of Whisker

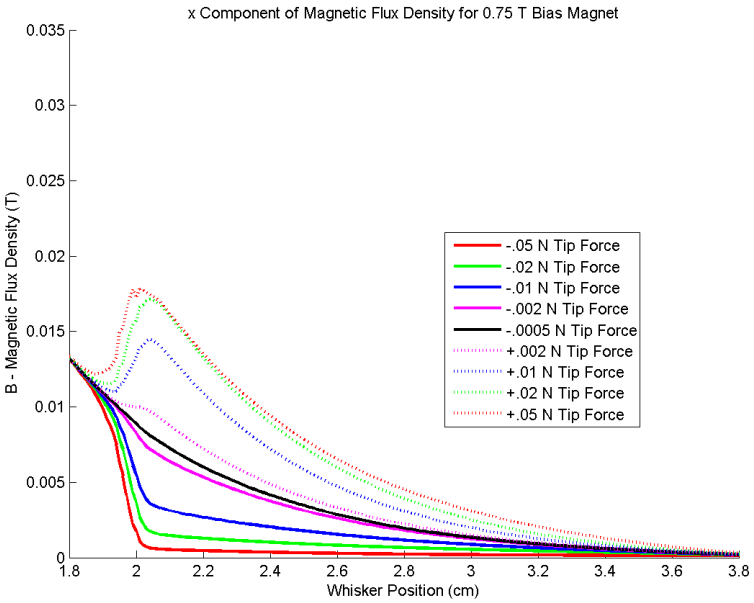

Figure 67: x-Component of B Field for .75 T Bias Magnet - Bottom of Whisker

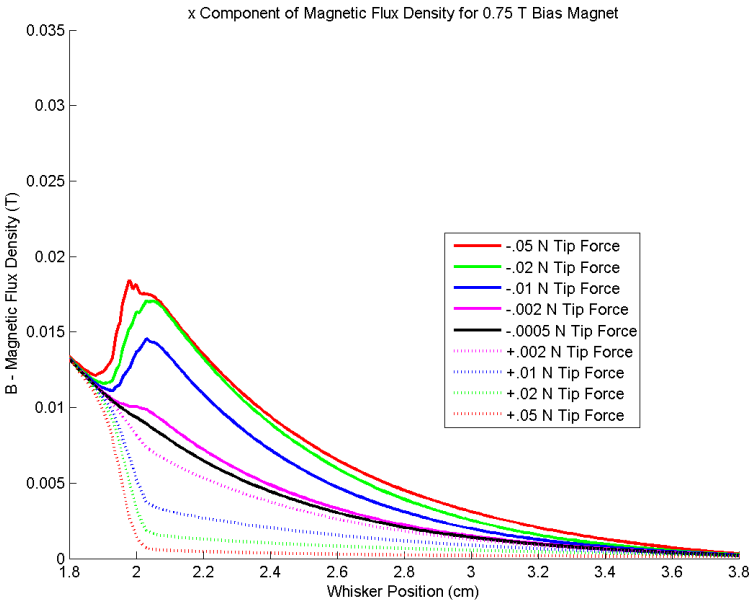

Figure 68: x-Component of B Field for .75 T Bias Magnet - Top of Whisker

Appendix G – Previous Whisker Sensor Prototypes

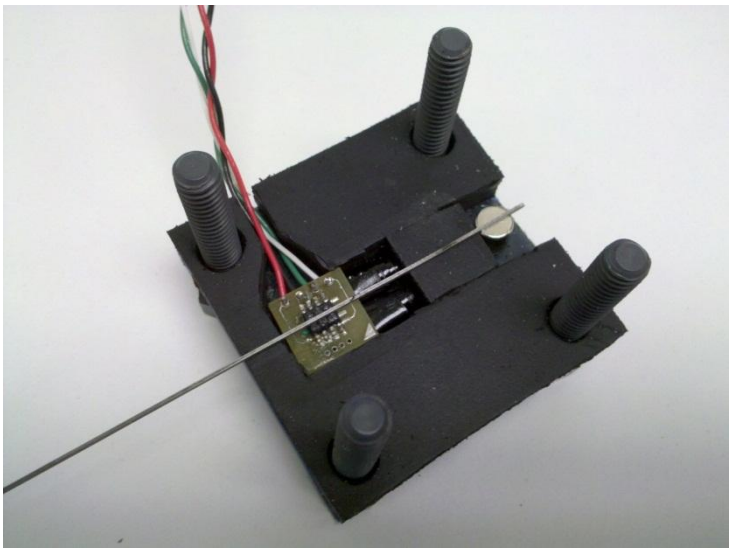

Figure 69: Second Prototype - Sensor Component Layout

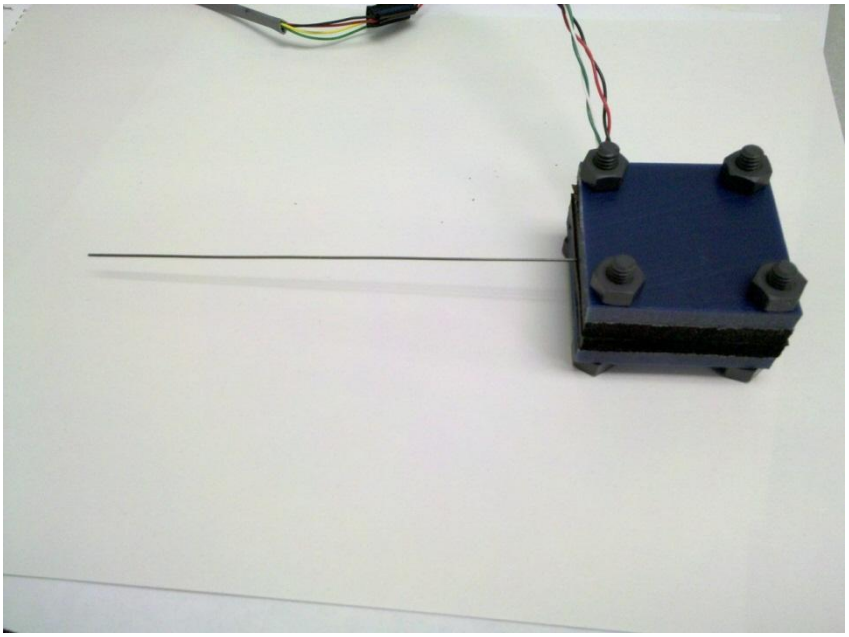

Figure 70: Second Prototype - Rubber Sheet Clamp

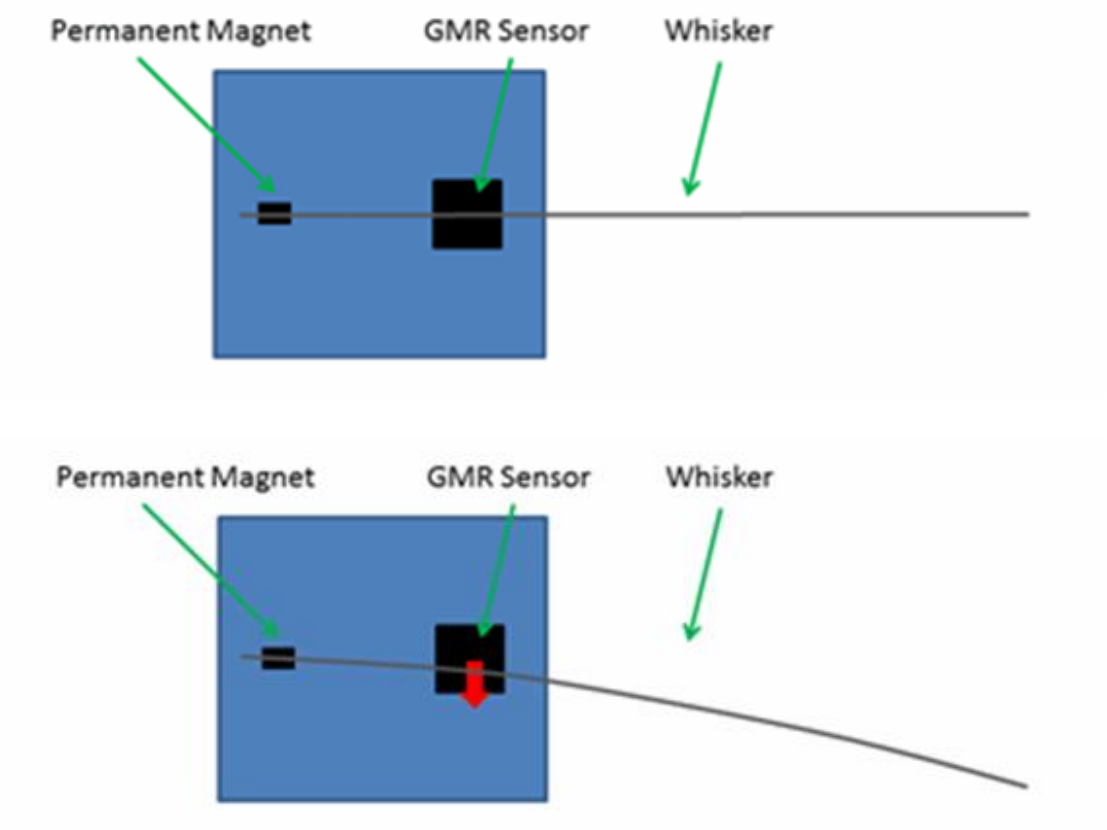

Figure 71: Second Prototype - Whisker Slippage between Rubber Sheets

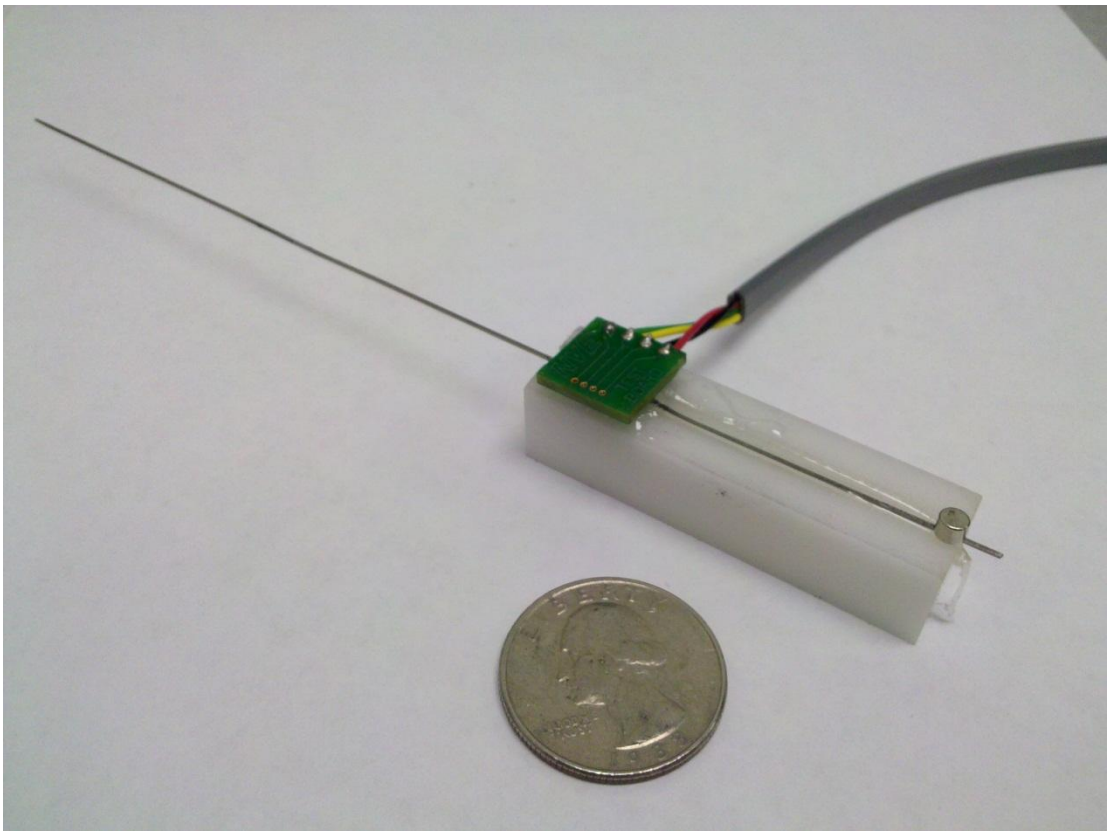

Figure 72: Third Prototype - Sensor Component Layout

Appendix H – Effect of Permanent Magnet Placement (.3 Tesla)

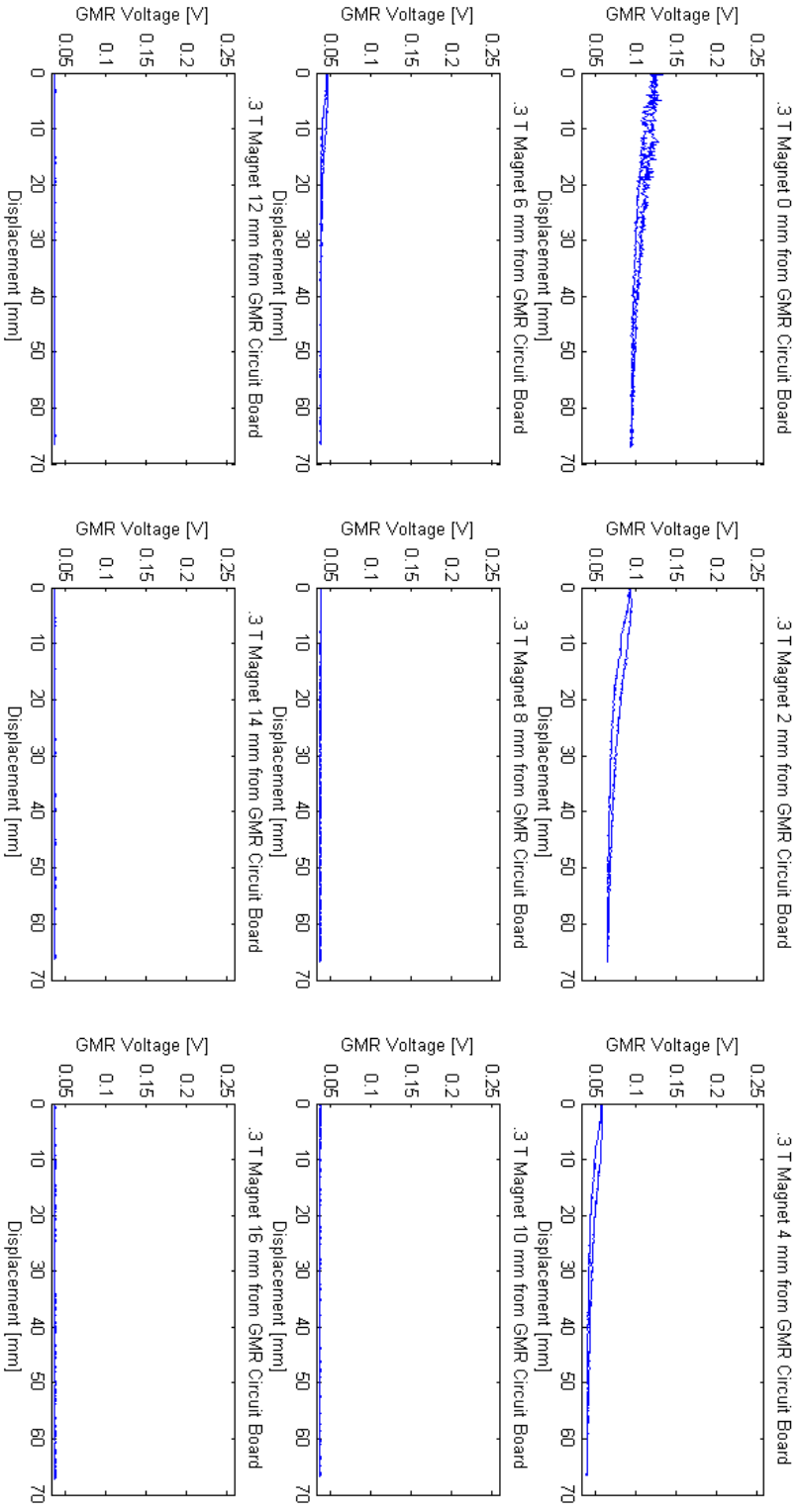

Figure 73: Effect of .3 T Bias Magnet Placement - GMR Voltage

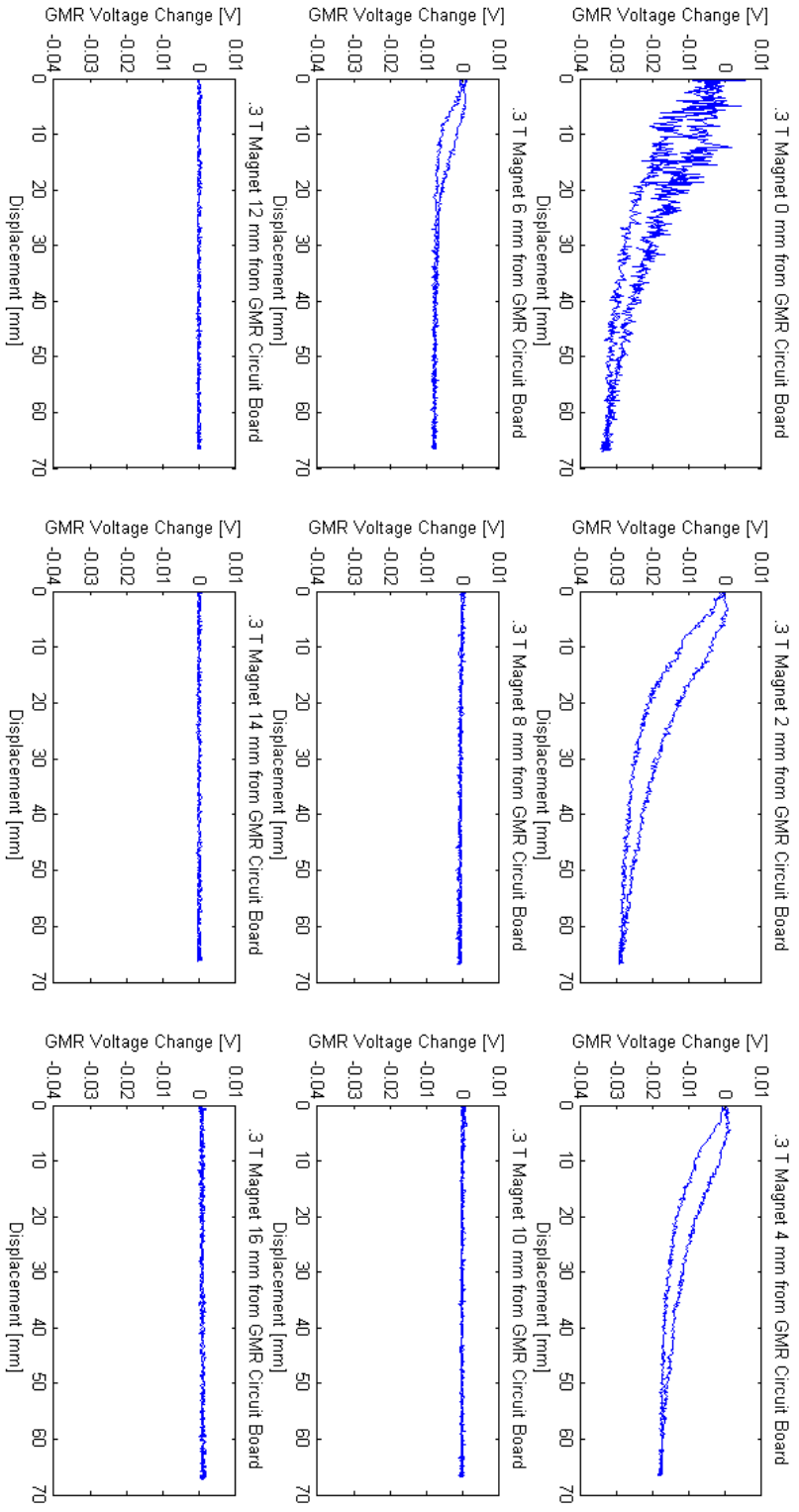

Figure 74: Effect of .3 T Bias Magnet Placement - GMR Voltage Change

Appendix I – Effect of Permanent Magnet Placement (.67 Tesla)

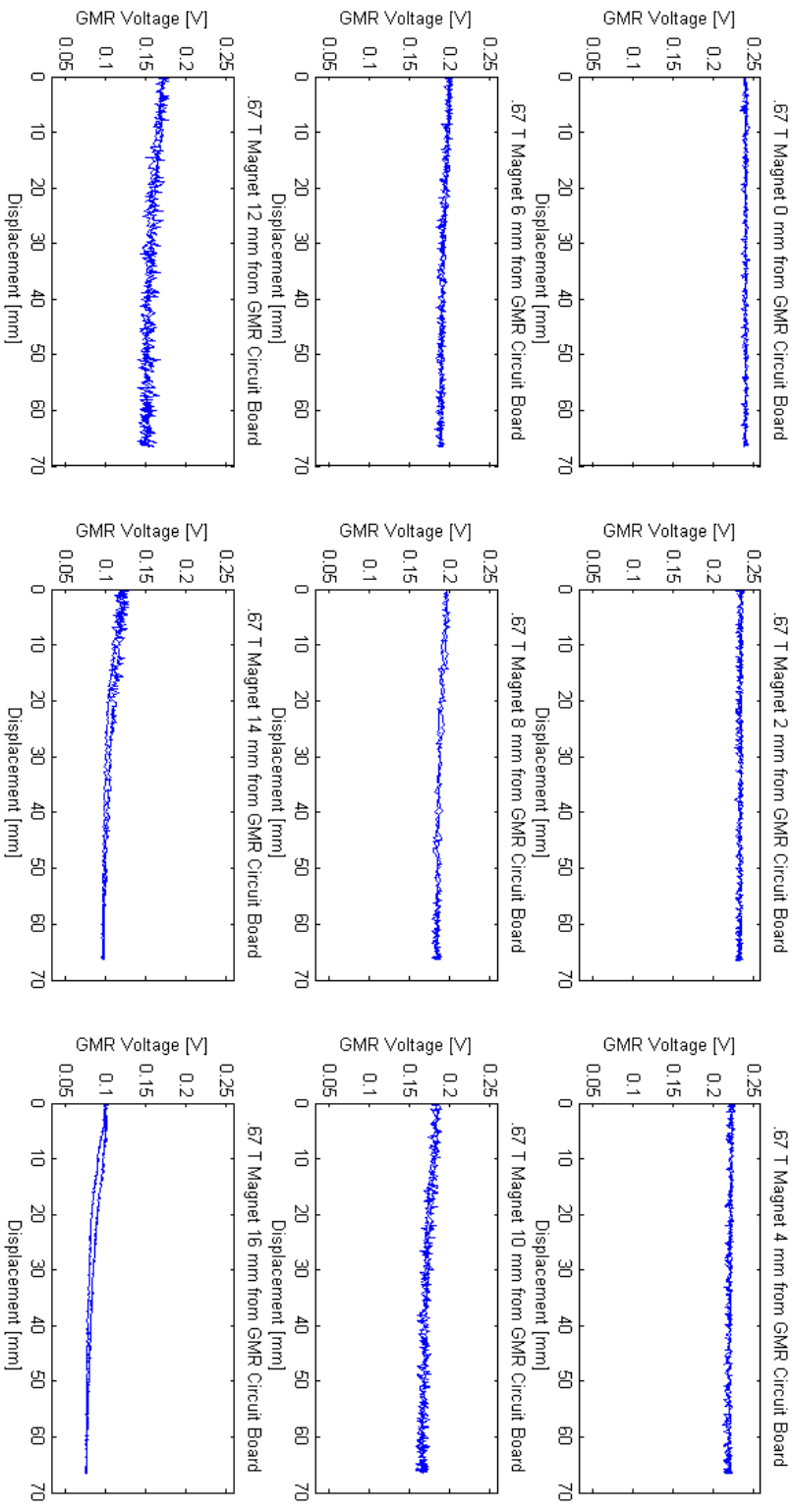

Figure 75: Effect of .67 T Bias Magnet Placement - GMR Voltage

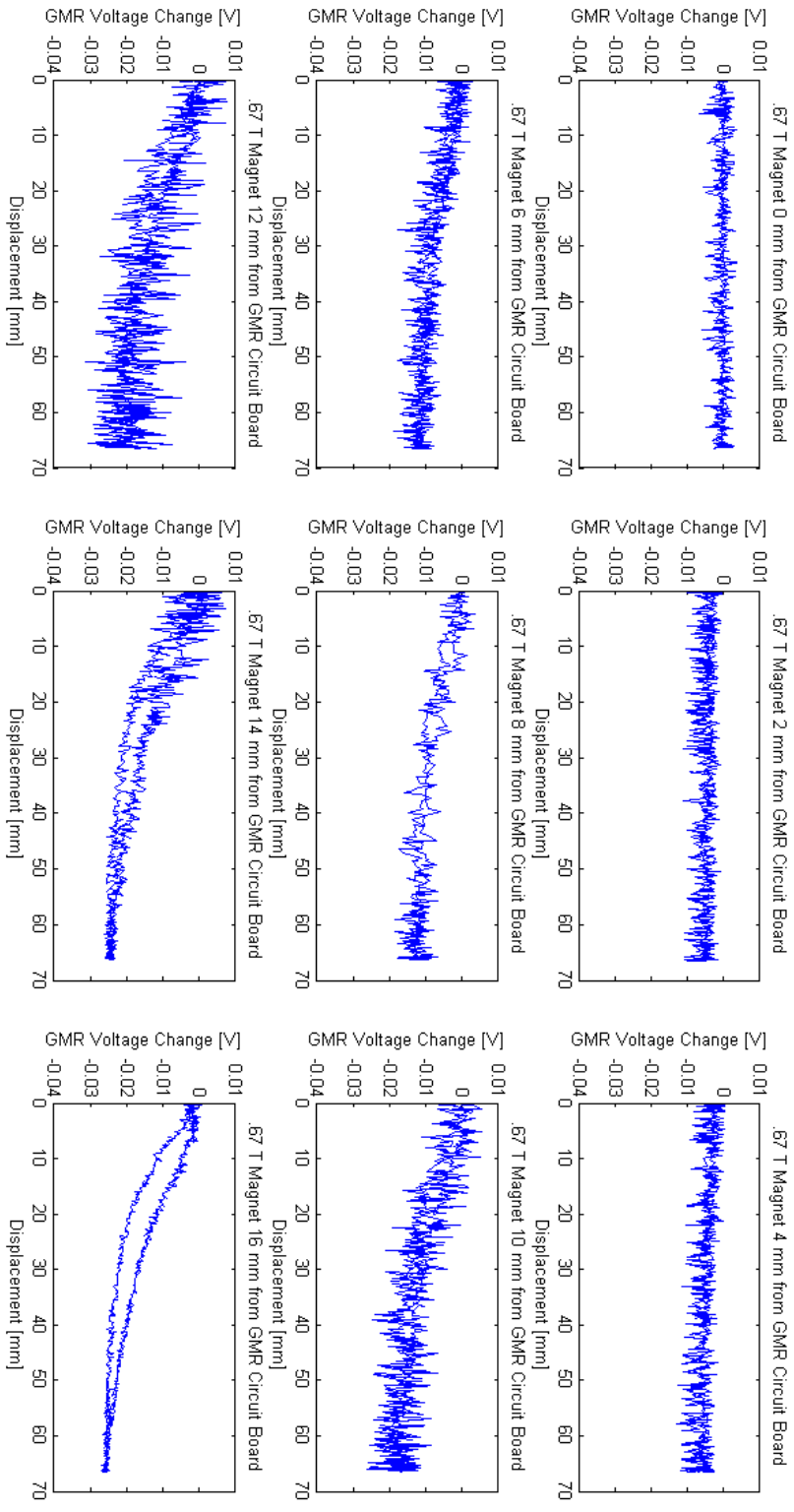

Figure 76: Effect of .67 T Bias Magnet Placement - GMR Voltage Change

Appendix J – Water Tunnel

The following figures depict the water tunnel setup used to test the whisker sensor. The water tunnel manufacturer was Engineering Laboratory Design, Inc. The water pump was manufactured by A Goulds Pumps Co.

Figure 77: Water Tunnel Manufacturer

Figure 78: Water Tunnel Pump

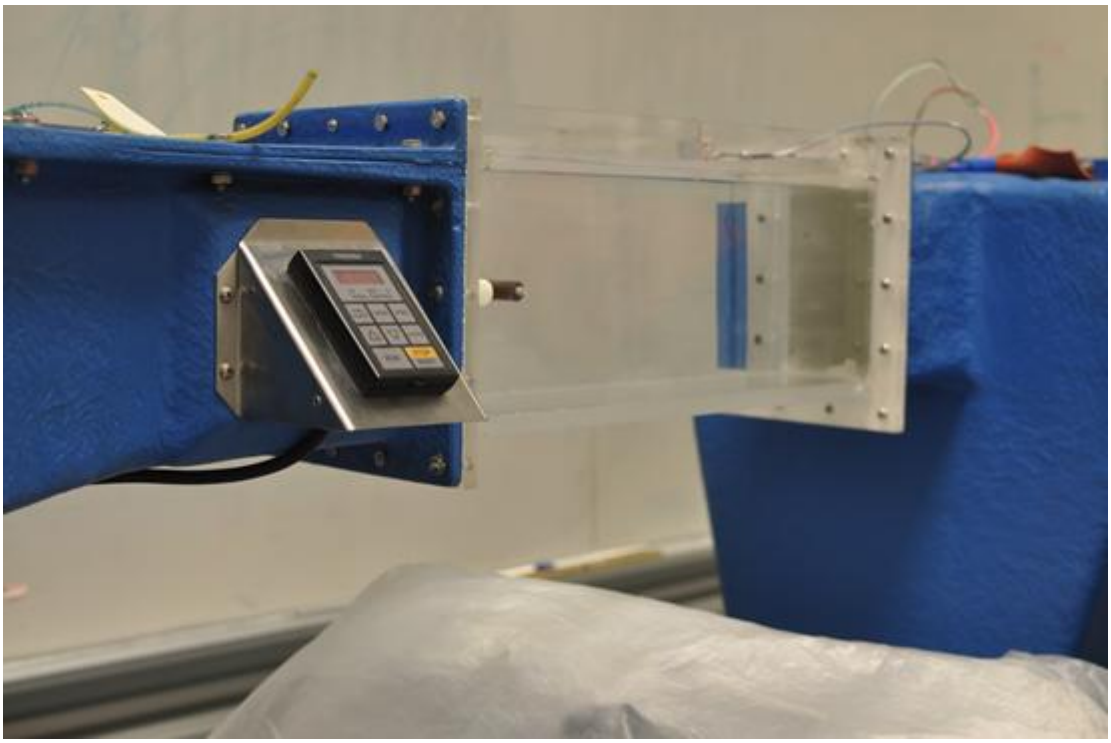

Figure 79: Water Tunnel Test Section

Figure 80: Water Tunnel

Bibliography

Albert, J., Friedrich, O., Dechant, H.-E., & Barth, F. (2001). Arthropod touch reception: spider hair sensilla as rapid touch detectors. *J Comp Physiol A*, 303-312.

Armstrong, W. D. (1997). Magnetization and magnetostriction processes in Tb(0.27-0.30)Dy(0.73-0.70)Fe(1.9-2.0). *Journal of Applied Physics*, 2321-2326.

Atulasimha, J. (2006). Characterization and modeling of the magnetomechanical behavior of iron-gallium alloys. College Park, MD: University of Maryland.

Barbier, C., & Humphrey, J. A. (2008). Drag force acting on a neuromast in the fish lateral line trunk canal. I. Numerical modelling of external-internal flow coupling. *Journal of the Royal Society Interface*, 627-640.

Burr-Brown Corporation. (1994, April). INA118 Precision, Low Power Instrumentation Amplifier. U.S.A.

Chopra, I. (2009). ENAE 651 class note on Smart Structures. College Park, MD: University of Maryland, Department of Aerospace Engineering.

Datta, S. (2009). *Quasi-static characterization and modeling of the bending behavior of single crystal galfenol and magnetostrictive sensors and actuators.* PhD Thesis, University of Maryland, Department of Aerospace Engineering, College Park.

Dehnhardt, G., Mauck, B., Hanke, W., & Bleckmann, H. (2001, July 6). Hydrodynamic Trail-Following in Harbor Seals (Phoca vitulina). *Science*, pp. 102-104.

Downey, P. R. (2008). Characterization of Bending Magnetostriction in Iron-Gallium Alloys for Nanowire Sensor Applications. College Park, MD: University of Maryland.

Downey, P., & Flatau, A. (2005). Magnetoelastic bending of Galfenol for sensor applications. *Journal of Applied Physics*.

Flatau, A., & Chong, K. (2002). Dynamic smart material and structural systems. *Engineering Structures*, 261-270.

Graham, F. (2009). *Development and Validation of a Bidirectionally Coupled Magnetoelastic FEM Model for Current Driven Magnetostrictive Devices.* College Park, MD: University of Maryland Department of Aerospace Engineering.

Haulman, D. L. (2003). *U.S. Unmanned Aerial Vehicles in Combat, 1991-2003.* Air Force Historical Research Agency. Defense Technical Information Center.

Hockmuth, C. M. (2007, February). UAVs - The Next Generation. *Air Force Magazine*, pp. 70-74.

Jiles, D., & Atherton, D. (1984). Theory of the magnetisation process in ferromagnets and its application to the magnetomechanical effect. *Journal of Physics D: Applied Physics*, 1265-1281.

Kellogg, R. A. (2003). *Development and modeling of iron-gallium alloys.* Ames, Iowa: Iowa State University.

Lee, E. (1955). Magnetostriction and Magnetomechanical Effects. *Rep. Prog. Phys.*

Loctite. (2011). *Loctite Epoxy Heavy Duty Technical Data from Loctite Adhesives.* Retrieved November 15, 2011, from Loctite Products Website:

http://www.loctiteproducts.com/p/epxy_heavy/technical-data/Loctite-Epoxy-Heavy-Duty.htm

Mudivarthi, C., Datta, S., Atulasimha, J., & Flatau, A. B. (2008). A bidirectionally coupled magnetoelastic model and its validation using a Galfenol unimorph sensor. *Smart Mater. Struct.*

Na, S.-M., Yoo, J.-H., & Flatau, A. B. (2009). Abnormal (110) Grain Growth and Magnetostriction in Recrystallized Galfenol With Dispersed Niobium Carbide. *IEEE Transactions on Magnetics*, 4132-4135.

novotechnik. (2007, February). *Novotechnik Linear Catalog 2007.* Retrieved November 1, 2011, from Novotechnik Corporate Website: www.novotechnik.com/catalogs/pdfs/TTS.pdf

NVE Corporation. (n.d.). Application Notes for GMR Sensors.

NVE Corporation. (n.d.). *NVE AA and AB-Series Analog Sensors.* Retrieved 10 16, 2011, from NVE Corporation Website: www.nve.com/Downloads/analog_catalog.pdf

Pines, D. J., & Bohorquez, F. (2006). Challenges Facing Future Micro-Air-Vehicle Development. *Journal of Aircraft*, 290-305.

Schurter, H. M. (2009). *Experimental investigation of mechanical properties and auxetic behavior of iron-gallium alloys.* Masters' Thesis, University of Maryland, Department of Aerospace Engineering, College Park.

Spillman Jr, W. B., Sirkis, J. S., & Gardiner, P. T. (1996). Smart materials and structures: what are they? *Smart Mater. Struct.*, 247-254.

Tzou, H., Lee, H.-J., & Arnold, S. M. (2004). Smart Materials, Precision Sensors/Actuators, Smart Structures, and Structronic Systems. *Mechanics of Advanced Materials and Structures*, 367-393.

U.S. Department of Transportation Federal Aviation Administration. (2008). *Pilot's Handbook of Aeronautical Knowledge.* Retrieved November 22, 2011, from Federal Aviation Administration Web site: http://www.faa.gov/library/manuals/aviation/pilot_handbook/